

COVRA Rocksalt Sealing Project

Long-term porosity-permeability evolution in and around backfilled openings in a radioactive waste repository in rock salt

**Preliminary recommendations for modelling
compaction creep and porosity-permeability
evolution in crushed salt backfill**

Phase 1 Deliverable

B.G.A. van Oosterhout (b.g.a.vanoosterhout@uu.nl),

S.J.T. Hangx, C.J. Spiers, J.H.P. de Bresser

HPT Laboratory, Faculty of Geosciences,

Utrecht University, The Netherlands

Work performed in the period October 2021 – April 2022



Utrecht University



Table of Contents

| | | |
|----------|--|-----------|
| 1 | Introduction..... | 3 |
| 1.1 | Evolution of the backfill..... | 4 |
| 1.2 | Problem statement and aim | 7 |
| 2 | Deformation mechanisms associated with backfill compaction | 8 |
| 2.1 | Conditions in repository and backfill properties..... | 8 |
| 2.1.1 | Depth and stress conditions | 8 |
| 2.1.2 | Temperature..... | 10 |
| 2.1.3 | Backfill characteristics | 10 |
| 2.1.4 | Brine content..... | 11 |
| 2.2 | Creep mechanisms in salt rock (Stage II)..... | 11 |
| 2.2.1 | Dislocation creep | 12 |
| 2.2.2 | Solution-precipitation creep (pressure solution) in salt | 15 |
| 2.2.3 | Composite creep behavior | 19 |
| 2.3 | Recrystallization (Stage II and III) | 20 |
| 2.4 | Static healing mechanisms (Stage III) | 21 |
| 3 | Previous experimental work on compaction creep in rock salt backfill | 23 |
| 3.1 | Overview of experimental techniques..... | 23 |
| 3.1.1 | Pre-compaction techniques..... | 24 |
| 3.2 | Mechanical data and constitutive models..... | 25 |
| 3.3 | Porosity-permeability relations | 30 |
| 3.4 | Evaluation of models and comparison on experimental data..... | 32 |
| 3.4.1 | Effect of humidity and grain size distribution on pressure solution creep rates..... | 32 |
| 3.4.2 | Model comparison on experimental data..... | 33 |
| 4 | Recommendations for modelling gallery convergence and internal backfill evolution | 35 |
| 4.1 | Recommended creep laws for intact rock salt – the host rock around an opening (Stage I and II)..... | 36 |
| 4.2 | Recommendation for modelling backfill compaction (Stage II)..... | 37 |
| 4.2.1 | Preliminary order of magnitude calculations for backfill compaction during Stage II convergence..... | 38 |
| 4.2.2 | Recommendations for porosity-permeability evolution in Stage II | 43 |
| 4.2.3 | Recommendations for static backfill evolution (Stage III)..... | 44 |
| 4.3 | An analytical approach to coupled convergence: Towards a fast model for estimating Stage II convergence times? | 45 |
| 4.3.1 | Elements of an analytical solution for Stage II convergence | 46 |
| 4.3.2 | Next steps to obtain improved Stage II convergence times..... | 49 |

| | |
|---|-----------|
| 5 Conclusion/Summary..... | 50 |
| References | 52 |
| A Appendices..... | 58 |
| A.1 BGR-CS3 model | 58 |
| A.2 Callahan model | 60 |
| A.3 C-WIPP models | 61 |
| A.4 Triaxial isotropic compaction tests TK-031 and TK-033..... | 62 |
| Experimental method..... | 62 |
| Experimental results..... | 62 |
| A.5 Isostatic long-term compaction test by IfG | 67 |
| Experimental method..... | 67 |
| Experimental results (mathematical fits) | 68 |
| A.6 TUC multi-stage test with isotropic and deviatoric stages..... | 71 |
| Experimental method..... | 71 |
| Experimental results..... | 72 |
| A.7 Hydrostatic compaction creep tests by Sandia | 74 |
| Experimental method..... | 74 |
| Mechanical results | 75 |
| Microstructures and interpretation of deformation mechanisms | 76 |
| A.8 Utrecht University stress relaxation tests..... | 78 |
| Experimental method..... | 78 |
| Experimental results and mechanistic interpretation | 79 |
| Microstructures | 82 |

1 Introduction

It is widely accepted that high level radioactive waste requires well-designed disposal for periods ranging from tens of thousands to a million years, to minimize release of the contained radioactivity into the environment (Pusch 2009). There is general agreement that placing radioactive waste in repositories in stable geological formations, with good sealing capacity, would be safer than long-term disposal in a ground level facility (Tsang et al. 2005). The main advantage of subsurface waste disposal is that less obligation for active management of the facility is passed onto future generations. The exposure to many (human-induced or natural) hazards is significantly reduced by subsurface disposal. Nevertheless, subsurface disposal is not risk free and many aspects must be considered for selecting a geological site for safe radioactive waste disposal.

Three types of host rocks are generally considered, namely: clay/claystone, crystalline igneous rocks and rock salt. Given the absence of igneous rocks in the accessible Dutch subsurface, research in the Netherlands is aimed at investigating the suitability of rock salt and clay formations (Hart et al. 2013; Vons & Prij 1988). Sealing of the waste is provided by a combination of engineered (cannister/container, backfill, plugs) and natural barriers (host rock, e.g. salt, clay or crystalline rock), which both contribute to preventing radionuclides from reaching the biosphere (Pusch 2009).

An advantage of selecting rock salt as a host rock for a waste repository is that creep processes in rock salt operate relatively fast, which ensures that porosity and permeability evolve to exceedingly low values during burial and, in particular, following any mechanical damage such as faulting (e.g. Langer 1999). These creep-related self-sealing properties are further augmented by the operation of fluid-assisted diffusive mass transfer processes, i.e. by dissolution-precipitation and recrystallization processes, that can further reduce pore-connectivity and hence permeability (Houben et al. 2013b; Koelemeijer et al. 2012a), especially on the long-term. These properties make salt rock favorable for repository construction due to ductile convergence of the repository and low permeabilities in the surrounding host rock.

The rapid operation of creep processes in rock salt allows for the use of crushed salt as backfill of the repository openings, which will compact over time along with the convergence of the surrounding host rock, providing an additional barrier. Crushed salt is readily available as backfill as it can be obtained from excavated material generated by the creation of the repository itself. Additional crushing, sieving and sorting can be done to achieve a mixture with grain sizes that are more favorable for fast compaction (Czaikowski et al. 2020). Other functions of the backfill include stabilizing of the

surrounding host rock and to conduct the heat generated from the decay of the radioactive waste (Holcomb & Hannum 1982).

It is expected that backfilled opening, such as shafts, galleries and boreholes, will ultimately converge and that the crushed backfill will compact to reach a state in which the properties, specifically the porosity and permeability, are comparable to the undisturbed (surrounding) host rock. Provided sufficient cavity closure and porosity - permeability reduction in the backfill can be achieved before the barrier function of the waste canisters can no longer be guaranteed due to corrosion (1000-10000 years), the backfilled zones present an additional, nearly impermeable geotechnical barrier for the long-term (1000 years – 1 million years). Hence, a key aim of research on salt repository integrity is to reliably predict the long-term porosity-permeability evolution of the backfill in converging repository openings, along with the decreasing cross-sectional area of the opening. Both permeability and cross-section play a role here, as the total volume of fluid that can flow through a backfilled opening, per unit time, is proportional to the product of backfill permeability times cross-section for flow (Darcy's Law). The timescale on which a given porosity-permeability and cross-section are achieved, during active convergence, in turn depends on how the convergence rate of an opening decreases as the resistance to compaction offered by the densifying backfill increases. To model this coupled problem rigorously, data are needed both on the deviatoric creep properties of the intact salt host rock and on the compaction creep properties of the salt backfill.

1.1 Evolution of the backfill

The compaction rate of backfill is expected to be controlled by a combination of mechanisms and depends on the properties of the backfill (mineralogy and grain size distribution;) and the conditions (stress state, temperature and brine availability/humidity) (Czaikowski et al. 2020; Holcomb & Hannum 1982; Kröhn et al. 2015; Zhang et al. 2007). Throughout this report, granular salt and crushed salt used as backfill is simply referred to as backfill. Under in-situ conditions in a converging backfilled opening in rock salt, the state of stress within the backfill will be determined by the mechanical coupling between the convergence creep of the surrounding salt rock and the compaction creep behavior of the backfill. In experiments addressing backfill compaction behavior, controlled stress or controlled compaction rate boundary conditions are usually imposed to obtain a compaction law that can be applied in numerical modelling of the supported convergence problem (e.g. Krohn et al. 2017; Prij 1991).

Experiments on backfill at an effective stress equal to the lithostatic pressure at repository depths (600-800m; i.e. 13-20 MPa, say 15 MPa, for typical overburden densities) indicate that during compaction, its porosity decreases from initial values of 30-40% down to 5% in the timespan of a few years, when small amounts of water are present (1 wt%) or when the backfill is saturated with brine (Krohn et al. 2017; Zhang et al. 2007). However, under dry (Zhang et al. 2007) or low humidity conditions (0 - 0.1 wt%) at the same stress levels (Czaikowski et al. 2020), low porosities (<10%) cannot be achieved on laboratory timescales, nor even when the measured compaction rates in dry backfill are extrapolated to 1000 years. When the porosity of the backfill drops below 5%, which in the laboratory is only reached in wet experiments, and certainly when the porosity gets down to around 1%, there is clear evidence of a decrease in compaction creep rates (Zhang et al. 2007). In a real backfilled opening, all these timescales will be significantly increased, as the stress in the backfill reaches lithostatic values only in the final stages of convergence.

Experiments, field observations and microstructural observations on intact rock salt under deviatoric conditions (because of mining activities or creation of cavities), show that dilatant deformation occurs in a region around cavities, which is generally called the excavation damage zone (EDZ). The creation of shafts and galleries in the repository is also expected to cause the formation of an EDZ in the surrounding host rock. Experiments on dilatancy in rock salt show that this microstructural change is associated with an increase of permeability from $< 10^{-21} m^2$ to $10^{-16} m^2$, while the increase in porosity associated with dilatancy is in the range from 0.1 to 1% (Peach & Spiers 1996). The creation of pathways by microcracking and rapid increase in permeability associated with dilatancy can be described using percolation theory. A porosity below 1% is considered as a desired target porosity for the backfill (Bechthold et al. 1999; Czaikowski et al. 2020).

The compaction time for the backfill to reach this “threshold” porosity is an important characteristic of the sealing performance. As the compaction rates slow down at low porosities (Bechthold et al. 1999; Krohn et al. 2017; Zhang et al. 2007), the timescales to reach porosities below 1% as a result of compaction creep processes will largely depend on the compaction rate in the later stages of convergence. At the same time, moisture-assisted diffusive mass transfer and recrystallization processes (i.e. fluid-assisted-recrystallization and grain boundary/crack healing) are known to dominate final densification and static healing/sealing of granular salt (Zhu & Arson 2015), crushed backfill (Krohn et al. 2017; Mills et al. 2018) and damaged host rock in the surrounding EDZ in the long-term (e.g. Peach et al. 2001; Houben et al. 2013; Urai et al. 2008). These processes are not necessarily captured in typical laboratory experiments and only become important when the decrease in porosity by compaction creep becomes negligible.

Although slow, these processes are likely to account for the final removal of residual porosity and, most importantly, they can be expected to decrease permeability by multiple orders of magnitude down to in-situ values for undisturbed dense rock salt ($10^{-21} - 10^{-23} m^2$). Despite this, these mechanisms are still poorly quantified and remain unaccounted for in constitutive models for either backfill or EDZ sealing, beyond mostly empirical laboratory fits (Czaikowski et al. 2020; Kröhn et al. 2015). As a result, uncertainties in the timescale on which pores and cracks remain open and connected in both backfill and EDZ material, in and around a converging opening, run into several orders of magnitude (Houben et al. 2013; Koelemeijer et al. 2012). This applies both for normal evolution scenarios (characterised by intrinsic repository moisture or humidity levels) and disturbed (e.g., flooded) evolution scenarios.

In total, three successive stages of gallery-, shaft- and borehole closure can be distinguished (see Figure 1-1): (I) unsupported convergent creep and microcracking in the EDZ surrounding the disposal galleries, prior to contact with the backfill; (II) backfill-supported convergent creep coupled with backfill compaction and porosity permeability reduction in the backfill and EDZ; and (III) near-static pore disconnection and healing/sealing as hydrostatic stress is approached and as creep closure and backfill compaction rates become negligible. Taking into consideration that shafts, galleries and boreholes will be backfilled immediately after waste emplacement is foreseen, only stages II and III are relevant for post-closure safety assessment. In addition, the EDZ is expected to be narrow (Tsang et al. 2005), with a permeability of several orders of magnitude lower than the permeability in the backfill at any point during the evolution of the repository (Peach et al. 2001). Hence, the EDZ will play a subordinate role in transport of radionuclides.

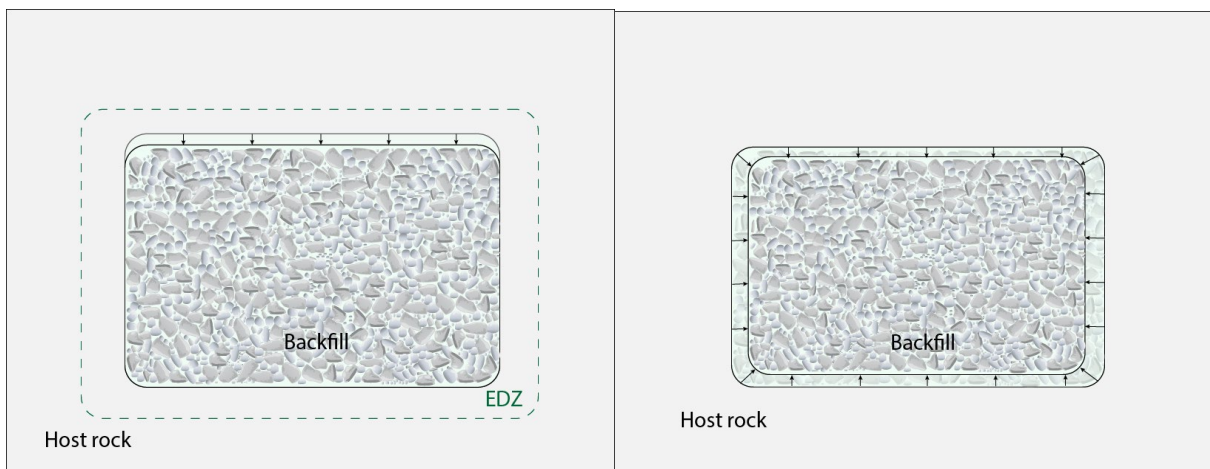


Figure 1-1: (left) Stage I behaviour: open convergence and creation of the excavation damage zone (EDZ). (right) stage II behaviour: coupled convergence of host salt rock surrounding a backfilled gallery. In stage III there is no convergence of the repository walls and porosity-permeability reduction takes place by static healing.

To model stage II and III evolution, constitutive equations describing the mechanical behavior and evolving porosity and permeability of the backfill are required – along with constitutive equations for the surrounding rock salt. Much is already known about the compaction of backfill on laboratory timescales, and the associated permeability evolution. Extrapolation of such empirical data down to about 5% is plausible. However, extrapolation beyond that is unconstrained and there are uncertainties due to (a) the empirical rather than microphysical basis of the constitutive relations used to describe compaction behavior and (b) the fact that slow pore-reconfiguration processes operating in the long term are not necessarily captured in conventional experiments on laboratory timescales.

1.2 Problem statement and aim

In this report an overview is given on existing work on experimental data and constitutive models of compaction creep in granular rock salt backfill. We do not consider creep laws for intact salt as these are well established (Carter et al. 1993; Hunsche & Hampel 1999; Spiers et al. 1990). The relevance and shortcomings of the existing work is discussed, and a first set of recommendations is given on how to improve the understanding of porosity-permeability evolution in a backfilled repository. In future reports, additional experiments on compaction creep (stage II) behavior, at low porosities and under controlled humidity, and healing (stage III) behavior will be used to further refine these recommendations and incorporate microphysical relationships as opposed to (partially) empirical laws.

2 Deformation mechanisms associated with backfill compaction

The porosity-permeability evolution in the backfill and EDZ will be controlled by the mechanisms controlling compaction creep rates (Stage II) and (near-) static porosity-permeability reduction (Stage III). The properties of the backfill and the conditions in the repository will determine which mechanisms are active, which will control backfill behaviour. Convergence of the repository walls and heat generation by radioactive waste will vary through time, causing changes in stress and temperature, activating different mechanisms. As the backfill is compacted, the porosity of the backfill will change, which may also cause a switch in controlling deformation mechanism (Zhang et al. 2007). The rate at which (grain boundary-) diffusional mechanisms operate is strongly determined by the grain size (distribution) of the backfill and when recrystallization is activated this may also change the grain size during the evolution of the backfill. Finally, the availability of water, in the form of moisture or brine, will accelerate creep and must be considered in modelling porosity and permeability reduction in the backfill (Bechthold et al. 1999). Given the range of conditions and the change in properties of the backfill during evolution, targeted experiments investigating the effect of each of these conditions are key to understanding the (rate-controlling) mechanisms and effectively modelling backfill behaviour.

In this chapter, an overview is given of the expected conditions in the repository and properties of the backfill. Subsequently, an overview is given of the different mechanisms associated with compaction creep (stage II) and healing (stage III) and their relevance for the conditions of the repository will be discussed.

2.1 Conditions in repository and backfill properties

2.1.1 Depth and stress conditions

Two locations are currently considered as a potential site for a repository of the Netherlands: the diapirs of the Zechstein in the northeastern part of the Netherlands (at a depth of about 700m; De Mulder et al. 2003) and the bedded salt of the Röt formation in the Eastern part of the Netherlands (at a depth of 300-500m; Schlöder & Urai 2005). Although, recent work by Altenberg (unpublished TNO-COVRA project) indicated that the Röt formation is not suitable for radioactive waste disposal. At depths of 700m, a lithostatic stress of ~15 MPa is expected. During stage I, the host rock surrounding an

opening (gallery, borehole, shaft) will not be supported by the backfill, the initial effective stress on the backfill is 0 MPa, and the backfill will only compact very slowly under its own weight. The duration of this stage will depend on the creep rates of the wall rock and on the distance between the gallery/borehole wall and the backfill. During stage II, the effective stress supported by the compacting backfill will rise to asymptotically approach the lithostatic stress of ~ 15 MPa. As the compaction creep rate will be determined by the effective stress, which in turn will depend on the resistance of the backfill and the convergence rate of the opening, a coupled convergence model taking creep of both the walls and the backfill itself is required (e.g. Krohn et al. 2017; Prij 1991). Such coupled models can simultaneously determine the cavity convergence, backfill porosity reduction and the effective stress in the backfill. An example is given in Figure 2-1. Note, that while the lithostatic (far-field) stress in this example is equal to 18.6 MPa (corresponding to a lithostatic stress at a depth of 800m), the minimal principal stress on the backfill will take 100 years to reach 6 MPa at 38.6 °C (e.g. just 1/3 of the lithostatic stress, for dry backfill) (intermediate and largest principal stress not given by author). Hence, assuming the effective stress equal to the lithostatic stress ($\sigma_1 = \sigma_2 = \sigma_3 = 18.6$ MPa) is too optimistic and a coupled model must be used to estimate the real stress state in the backfill and reliably estimate convergence rates.

As compaction continues and porosity decreases towards a few percent, compaction creep rates are expected to ultimately become exceedingly low (e.g. around 1% porosity, e.g. Zhang et al. 2007), which will mark the transition to stage III. During stage III, permeability is expected to decrease by means of near-static pore-disconnection and healing, caused by surface energy minimization and the development of equilibrium pore shapes (Holness & Lewis 1997; Houben et al. 2013), independently of the effective stress. Ultimately, pressurization of brine present in the pores by any ongoing compaction may reduce the effective stress to zero.

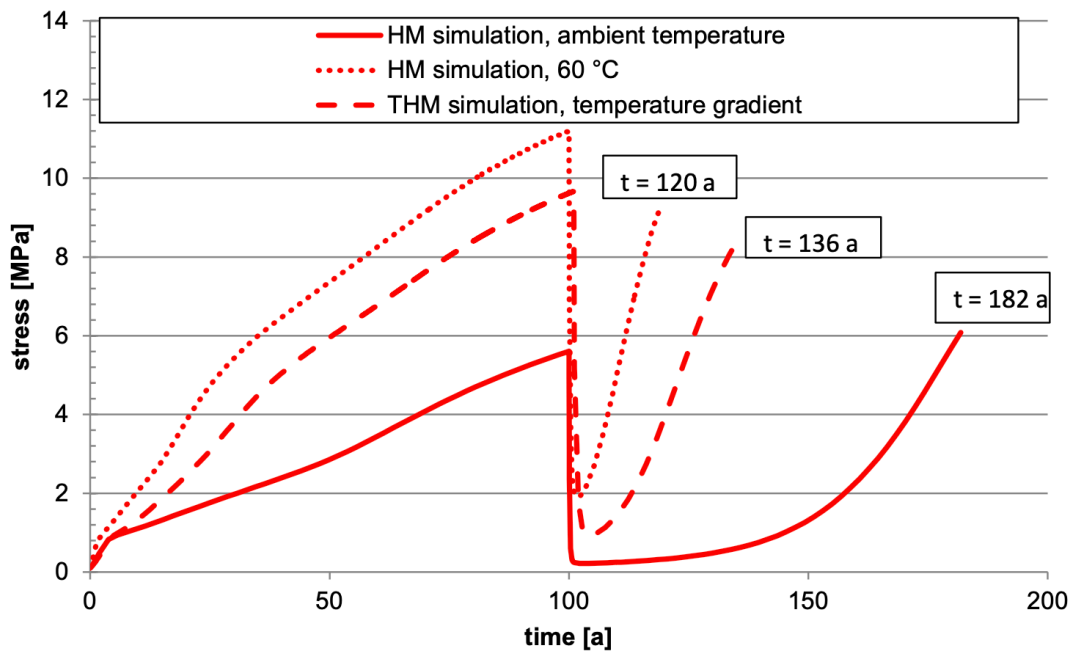


Figure 2-1: Evolution of minimal principal stress in the centre of a backfilled drift, plotted as a function of time in years (after Krohn et al. 2017). Model is based on CODE_BRIGHT (Czaikowski et al. 2020; Olivella et al. 1997) for a repository with a far field stress of 18.6 MPa (comparable to a lithostatic stress at a depth of 800m). The first 100 years is assumed dry and then brine is introduced into the model with a fluid pressure of 10 MPa, gradually saturating the backfill. Ambient temperature is 38.6 °C.

2.1.2 Temperature

Given the geotherm of north-western Europe, a temperature of 33°C is expected at a depth of 700m. The current Dutch strategy of long-term radioactive waste disposal is to store high level heat generating waste for 100 years in a ground level facility (Hart et al. 2015). As the heat generation after 100 years is just 10% of the initial heat generation, the effect of heat generation of the waste on the temperature in the repository is expected to be minimal. Therefore, it can be assumed that the temperature of the backfill will remain below 50°C, although this must be assessed.

2.1.3 Backfill characteristics

Grain sizes vary from 2 to 4 mm in the bedded Zechstein in the Twente region and from 2 to 10 mm in the salt diapirs in Groningen (Schléder & Urai 2005). In addition, salt formation can contain impurities such as anhydrite or clay affecting the mechanical properties of the salt. Crushed salt for the backfill is obtained from excavated material generated by the creation of the repository, however drilling of the repository will reduce the size of the fragments. The in-situ grain sizes can therefore be considered an upper

estimate of the grain sizes used for the backfill, without any special treatment. Additional crushing, sieving and sorting can be done to achieve a mixture with grain sizes that are more favorable for fast compaction, such as the “KOMPASS” mixture considered by Czaikowski et al. 2020. Another advantage of using a predetermined mixture is that compaction experiments on such a mixture may give more realistic results, although identifying mechanisms (and their contribution to the compaction rates) in experiments with a varying grain size can be challenging. It must also be noted that the crushed backfill (e.g. the starting material) inherits some of the properties and microstructure of the original formation it was excavated from. The presence of these inherited features (e.g. dislocation density, subgrains, slip bands, cracks and inclusions) may also affect the mechanisms controlling compaction creep and healing during backfill convergence.

2.1.4 Brine content

It is well established that intact dense rock salt contains between 0.05 and 1 wt.% of water (Urai et al. 1986). In rock salt-based geological disposal systems at depths up to a few km, it is expected that small quantities of brine naturally present in the salt will buffer the humidity to maximum values relatively close to the deliquescence point (78% RH) (Czaikowski et al. 2020; Koelemeijer et al. 2012b). A higher humidity will cause an increase in adsorbed fluid film thickness, causing an increase in effective surface diffusivity (Koelemeijer et al. 2012b). This in turn will accelerate fluid-assisted grain boundary migration (Ter Heege et al. 2005a). When performing compaction experiments it must be considered that without special humidity control salt will always adsorb moisture from the air (e.g. Zhang et al. 2007). Current backfill recipes (e.g. KOMPASS mixture) include small amounts of brine (0.5-1 wt. %) to enhance compaction, which will buffer the relative humidity to around the deliquescence point.

2.2 Creep mechanisms in salt rock (Stage II)

The term creep describes the tendency of solid materials to deform permanently over time under the influence of deviatoric stress. Steady state creep refers to creep at a fixed rate, attained after an initial phase of decelerating or transient creep, all under a fixed stress (Poirier 1985). Rock salt is a ductile material that can undergo large creep strains without brittle failure, especially if the temperature and confining pressure are high and the deformation rate is slow (Senseny et al. 1992). The behaviour of the material can be described using a variety of constitutive equations or creep “laws” that reflect the basic physical processes at the grain scale that determine deformation, hardening and recovery

of the material. The rate of these mechanisms and their contribution to strain and deformation depend on factors such as stress, temperature, grain size, fluid chemistry and impurity content. For large strain deformations of intact rock salt, such as those associated with convergence creep in a borehole or gallery wall, deformation is generally assumed to be dominated by steady state flow, with transient creep playing a minor role (Prij 1991). In salt, and indeed almost all dense crystalline materials, steady state creep is generally described using either empirical or microphysically based flow laws of the form (e.g. Frost and Ashby 1982):

$$\dot{\varepsilon} = A \exp\left(\frac{-Q}{RT}\right) \frac{\sigma^n}{d^m} \quad (\text{Eq. 2.1})$$

where, $\dot{\varepsilon}$ is in the strain rate in s^{-1} (or day^{-1}), A is a material parameter that may depend on grain size (MPa^{-n}), Q is the activation energy in $kJ mol^{-1}$, R is the gas constant in $kJ mol^{-1} K^{-1}$, T is the temperature in K, σ is the differential stress (MPa), n is the stress exponent, d is the grain size in m and m is the grain size exponent which is 0 for a grain size insensitive mechanism. For compaction creep of a porous material such as salt backfill, on-going, steady state creep is not possible due to the continuous decrease in porosity and associated decrease in stress intensification at the grain scale. However, assuming a series of steady states that evolve with porosity reduction, then compaction creep can often be adequately approximated using a form similar to (2.1):

$$\dot{\varepsilon}_v = A f(\phi) \exp\left(\frac{-Q}{RT}\right) \frac{\bar{\sigma}^n}{d^m} \quad (\text{Eq. 2.2})$$

where $\dot{\varepsilon}_v$ is now the volumetric strain rate in s^{-1} (or day^{-1}), $\bar{\sigma}$ is the mean effective stress (MPa), and $f(\phi)$ (MPa^{-n}), is a decreasing function of porosity as well as being potentially grain size dependent (e.g. Pluymakers & Spiers 2015). At high stresses, the dependence of strain rate on stress seen in equations 2.1 and 2.2 is often better described by a hyperbolic sine or exponential function of stress (Haupt 1991).

2.2.1 Dislocation creep

Lattice defects carry plastic deformation of crystals, through the movement of dislocations (line and planar defects) causing intergranular transportation of matter through the lattice (Poirier 1985). These types of deformation mechanisms are called dislocation creep. During dislocation creep, deformation occurs as a result of glide of edge and/or screw dislocations in specific (easy) lattice planes or glide planes. This motion is limited by obstacles within the lattice that may either be overcome by (stress-assisted) thermal agitation (glide-controlled creep) or if obstacles are too large, by either vacancy-supported diffusive motion of edge dislocations (Weertman 1955) or by cross-

slip of screw dislocations (Poirier 1976) (recovery-controlled creep). At moderate stresses and higher temperatures, where recovery-controlled creep dominates, dislocation cross-slip and dislocation climb in effect counteract the hardening process of dislocation multiplication and tangling by enabling reactions in which dislocations of opposite sign combine and annihilate.

2.2.1.1 Glide-controlled creep (dislocation glide) in salt

At low temperatures and high deviatoric stress, in the absence of water, and at confining pressures (mean normal stresses) high enough to prevent microcracking ($> 10\text{-}15\text{ MPa}$), deformation of intact salt rock occurs by glide-controlled creep (Carter & Heard 1970; Wawersik & Zeuch 1986). The occurrence of dislocation glide is manifested in microstructures as the creation of slip bands, which evolve into zones of accumulating and entangling dislocations with increasing deformation (see Figure 2-2). For dislocation glide, where temperature is too low for dislocations to climb out of their lattice planes to bypass obstacles, the steady state strain rate in dense salt rock is given by (Carter & Heard 1970):

$$\dot{\epsilon} = A_1 \exp\left(\frac{-Q_{dg}}{RT}\right) \sinh(B_1 \sigma) \quad (\text{Eq. 2.3})$$

where A_1 (s^{-1}) and B_1 (MPa^{-1}) are empirically determined material parameters for dislocation glide, σ is the differential stress (MPa), Q the activation energy for dislocations to initiate gliding. Alternatively, it can be approached by using a power law equation ($\dot{\epsilon} \propto \sigma^n$), with very large stress apparent stress exponents, as is often done with experimental data that is ascribed to dislocation glide (e.g. Wawersik & Zeuch 1986). Despite differences in porosities, the mechanism of dislocation glide is also attributed to control compaction creep in porous granular salt at high stresses, low temperatures and in the absence of water (Holcomb & Zeuch 1990; Zhang et al. 2007). Holcomb & Zeuch 1990 obtained a high n value of 18.5 and Zhang et al. 2007 obtained even higher n values of 20-22, at room temperatures and stresses above 20 MPa.

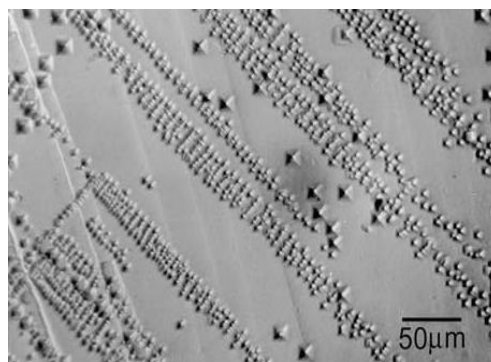


Figure 2-2. Micrographs of halite showing slip bands (taken from Barber & Meredith 1990).

2.2.1.2 Recovery-controlled creep in salt

There are two recovery mechanism: cross-slip and climb. Climb requires higher temperatures ($T > 0.5 T_m$) as vacancy diffusion will require higher temperatures but can also occur at lower stress and strain rate. A generalized form of Weertman's dislocation climb model (Weertman 1955) is given as (Frost & Ashby 1982):

$$\dot{\varepsilon} = A_2 \exp\left(\frac{-Q_{dc}}{RT}\right) \sigma^n \quad (\text{Eq. 2.4})$$

where A_2 is a material parameter, Q_{dc} is the activation for self-diffusion of vacancies which ranges from 70-130 kJ mol^{-1} (depending on pressure and temperature conditions; e.g. Senseny et al. 1992; Wawersik & Zeuch 1986). Note that in this form, the shear modulus is implicitly taken into account in the material parameter. Depending on diffusion mode, i.e. bulk diffusion or through the dislocation cores, the stress exponent (n) is either 3 or 5 (Poirier 1985). In dislocation cross slip, screw dislocations may surmount an obstacle by temporarily gliding onto a plane oblique to the primary glide plane. Screw dislocations of opposite sign cross slip towards each other and mutually annihilate. Cross slip is a thermally activated process in which the activation barrier is reduced by stress. Its general creep equation is given as (after Poirier 1976):

$$\dot{\varepsilon} = A_3 \exp\left(\frac{-Q_{cs}}{RT}\right) \sigma^2 \quad (\text{Eq. 2.5})$$

in which, Q_{cs} is the activation energy, which is dependent on stress and hydrostatic pressure (e.g. De Bresser 2002). Microstructural evidence for dislocation creep is given by the development of subgrains whose size depends systematically on steady state flow stress, as shown for synthetic halite and natural dense rock salt by Carter et al. 1982; Schlöder & Urai 2005; Ter Heege et al. 2005b.

Despite the large body of data that already exist on the mechanical behavior of rock salt and resulting empirical flow laws (Carter et al. 1993; Carter & Heard 1970; Ter Heege et al. 2005b; Wawersik & Zeuch 1986), the underlying question what microphysical mechanisms govern plastic flow of natural dense salt rock at in situ conditions has not yet been answered to full satisfaction (Muhammad 2015). Especially, the exact mechanism controlling dislocation motion at relatively low temperature is still insufficiently understood. Therefore, uncertainties exist regarding the appropriate mechanism-based flow law for low temperature, which makes extrapolation of lab creep data to in situ strain rates challenging.

Experiments on crushed backfill (Callahan & Hansen 1999; Korthaus 1996; Kröhn et al. 2015; Stührenberg & Zhang 1995) and granular salt (Zhang et al. 2007), at ambient conditions (i.e. containing its natural water content) indicate stress exponents in the range

of 4.7-7.5. Hence, most constitutive laws on compaction creep in backfill contain a power law-term with a stress exponent of around 5 (e.g. Callahan & Hansen 1999; Kröhn et al. 2015). This is generally attributed to a combination of different dislocation mediated mechanisms, but uncertainties exist on which mechanisms play a role (e.g. Zhang et al. 2007) and a satisfying microphysical basis is lacking.

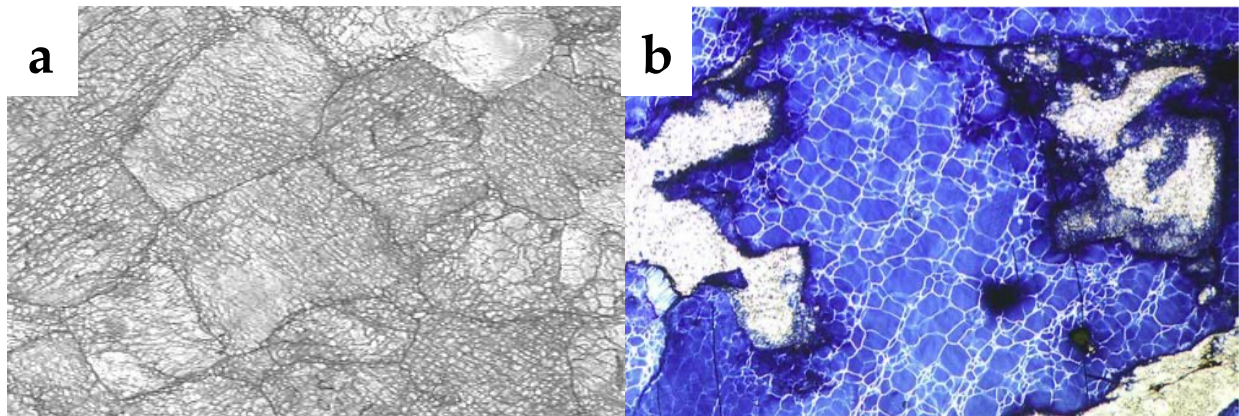


Figure 2-3. (a) reflection micrograph of etched section of synthetic rock salt deformed in the lab at 125 °C and 20 MPa featuring deformation bands and a fine cellular subgrain structure (Ter Heege et al. 2005) and (b) micrograph of gamma-irradiated, naturally deformed rock salt showing the formation of subgrains (Schléder & Urai 2005).

2.2.2 Solution-precipitation creep (pressure solution) in salt

Besides dislocation-mediated mechanisms, deformation in rock salt can occur by means of diffusional mechanisms, i.e. diffusive mass transfer from grain boundaries under a high compressive normal stress to those under a lower normal stress (Frost and Ashby 1982). Diffusion in a polycrystalline aggregate can occur as (1) diffusion of vacancies through the grain volume or lattice (Nabarro-Herring creep), (2) grain boundary diffusion of vacancies (Coble creep) and (3) grain boundary diffusion of ions dissolved in a grain boundary brine/moisture film (solution-precipitation or pressure solution creep). Volume diffusion requires very high temperatures ($T > 0.8 T_m$), allowing vacancies to diffuse through the lattice in the opposite direction as the flow of matter, resulting in strain. Grain boundary diffusion of vacancies requires slightly lower temperatures ($0.6 T_m < T < 0.8 T_m$). The temperature, for both of these solid-state mechanisms is not reached under repository conditions.

By contrast, when brine is present in salt rock, diffusion can occur through the thin fluid films that are found between grains, which can significantly enhance grain boundary diffusion and have a strong impact on creep (e.g. Urai et al 1986). This process is often referred to as pressure solution. Brine is nearly always present in natural dense salt and hence is expected to play a role in deformation of natural dense rock salt (e.g. Spiers et

al. 1990; Urai et al. 1986). The process is driven by stress-induced gradients in chemical potential along grain boundaries. At grain boundaries under high normal stress (i.e. high chemical potential) material is dissolved, followed by diffusion through the fluid film, and finally is precipitated again at boundaries supporting low normal stress (i.e. with a low chemical potential). These are serial processes of which the slowest is rate controlling. For NaCl it is generally believed that ionic diffusion is the slowest step under all relevant conditions (Spiers et al. 1990). This mechanism becomes dominant over dislocation creep at low stresses for which the transition stress depends on grain size and is expected at 7, 4 and 2 MPa for respectively grain sizes of 2, 5 and 10 μm (Spiers & Carter 1998). The corresponding flow law for dense salt creep by pressure solution is given by (Spiers et al 1990):

$$\dot{\epsilon}_v = A_3 \exp\left(\frac{-Q_{ps}}{RT}\right) \frac{\bar{\sigma}}{Td^3} \quad (\text{Eq. 2.6})$$

in which A_3 ($\text{K m}^3 \text{MPa}^{-1} \text{s}^{-1}$) is an empirically determined material parameter, Q_{ps} is the activation energy for pressure solution (kJ mol^{-1}), which is determined at 25.0 kJ mol^{-1} , d is the grain size (m), and T is the temperature (K). The strain in rate is linearly dependant on stress ($n = 1$) and has a cubic inverse dependence on grain size ($m = 3$). This material parameter (A_3) is derived from experiments with the pores filled with 100% saturated brine and takes the value of $3.76 \cdot 10^{-13} \text{ K m}^3 \text{MPa}^{-1} \text{s}^{-1}$.

2.2.2.1 Diffusion-controlled compaction creep under saturated conditions

For compaction creep of porous salt, this material parameter will also depend on porosity as the contact area will increase with decreasing porosity, leading to a reduction in contact stress. Hence, for diffusion-controlled compaction creep the flow law is given by (Pluymakers & Spiers 2015):

$$\dot{\epsilon}_v = A_3 f(\phi) \exp\left(\frac{-Q_{ps}}{RT}\right) \frac{\bar{\sigma}}{Td^3} \quad (\text{Eq. 2.7})$$

Where $f(\phi)$ is a porosity function, which should be chosen such that (a) $f(\phi) \rightarrow \infty$, when $\phi \rightarrow \phi_0$, where ϕ_0 is the starting porosity at which grain contact shows negligible contact area, and (b) $f(\phi) \rightarrow 1$, when $\phi \rightarrow 0$. A porosity function satisfying these constrains is given by (Pluymakers & Spiers 2015):

$$f_1(\phi) = \frac{2\phi_0}{2\phi_0 - 2\phi} \quad (\text{Eq. 2.8})$$

with ϕ_0 taken as 40%. This approximation works down to porosities of circa 5%, but it breaks down at low porosities since with ongoing solution transfer, the grain geometry rapidly changes from spherical to cubic (Niemeijer et al. 2002). This is substantiated by the experimental results of Zhang et al. 2007 that show a decrease in strain rates of three

orders of magnitude between 25% porosity and 1% porosity (at a fixed stress of 10 MPa, both with same grain size of 137 μm), which is a larger decrease in strain rates than predicted by the theoretical approach of Pluymakers & Spiers 2015 (see Figure 2-4). Hence as an alternative, the porosity-dependence of diffusion-controlled compaction creep can also be determined by taking an empirical fit to the experiments of Zhang et al. 2007 at a fixed stress (here taken at 10 MPa), which can be approximated by:

$$f_2(\phi) = 9.74 \cdot 10^{-4} \phi^{2.589} \quad (\text{Eq. 2.9})$$

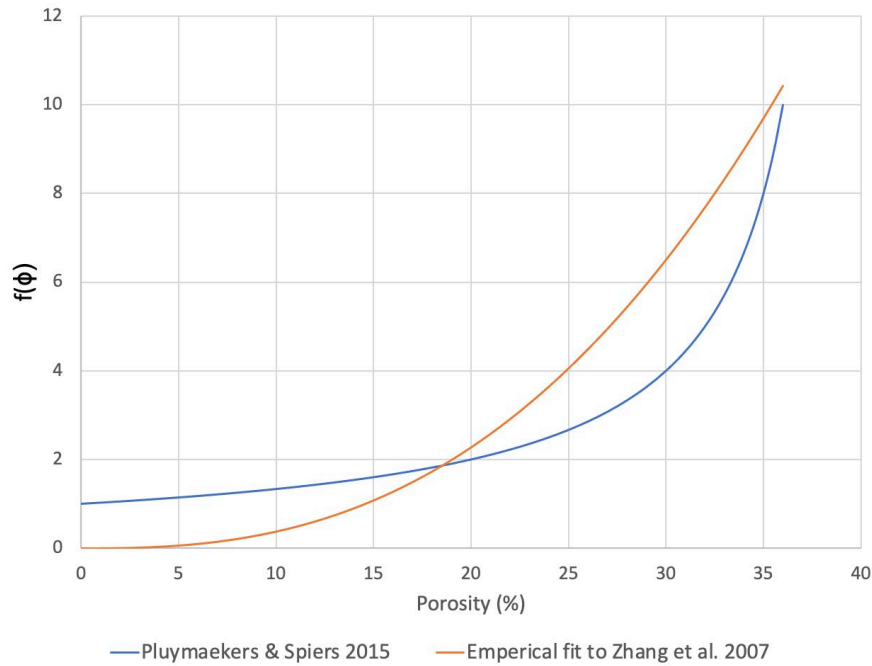


Figure 2-4: Comparison of porosity functions for diffusion-controlled compaction creep. The blue line shows the theoretical function after Pluymakers & Spiers 2015 (Eq. 2.7) and the orange line shows the empirical fit to the diffusion controlled experiments of Zhang et al. 2007 (Eq. 2.8). This shows that the observed decrease in strain rates at low porosities is larger than predicted from theory on contact area decrease of spherical grains.

2.2.2.2 Diffusion-controlled compaction creep under humid conditions

Up to this point, the pores are considered to be saturated with brine, which for a backfilled repository is not (always) the case. At a fixed temperature and porosity, material parameter A_3 is proportional to the effective surface diffusivity, given by:

$$A_3 \propto DCS \quad (\text{Eq. 2.10})$$

In which D is the diffusion coefficient (m^2s^{-1}), C is the solubility in m^3/m^3 and S is the fluid film thickness in m . This combined term DCS (effective surface diffusivity, m^3s^{-1}) takes a value of $6 \cdot 10^{-20} - 2 \cdot 10^{-19} \text{m}^3\text{s}^{-1}$ (Spiers et al. 1990) for saturated conditions. While the diffusive transport rates in bulk NaCl solution are rapid and well characterized, such data are not directly applicable to humid disposal conditions where

pore walls are coated with thin adsorbed water films. The thickness of the fluid film is expected to be controlled by the relative humidity (Koelemeijer et al 2012). In addition, the diffusion coefficient will decrease as the thickness decreases. Therefore, effective surface diffusivity will depend on humidity and will significantly reduce pressure solution creep rates.

Koelemeijer et al 2012 measured the surface impedance of single NaCl crystals. These impedance results were used to calculate the effective surface diffusivity, which lie in the range of $10^{-27} \text{ m}^3 \text{ s}^{-1}$ at very dry conditions to $10^{-19} \text{ m}^3 \text{ s}^{-1}$ for the deliquescence point at 296 K (see Table 1), the latter one is similar to the effective surface diffusivity given above for a saturated solution. Hence, it is expected that pressure solution creep rates are strongly dependent on humidity conditions. In rock salt-based geological disposal systems at depths up to a few km, it is expected that small quantities of brine naturally present in the salt will buffer the humidity to maximum values relatively close to the deliquescence point (78% RH) and at least above 60% RH. Many experiments (e.g. Czaikowski et al. 2020; Mills et al. 2018; Stührenberg 2013) consider adding a fixed amount of water to a sample, in the range of 0.5 wt% to 1.0 wt%, which correspond to a fluid film thickness of 30-100 nm (depending on grain size). Hence, these conditions correspond to effective grain surface diffusivities of 0-2 orders of magnitude lower (see Table 2-1), leading to a similar decrease in strain rates by pressure solution. Combining equation 2.7 and 2.9, and considering the humidity conditions expected in a repository (60-78% RH), diffusion-controlled compaction creep under humid conditions can be given by:

$$\dot{\epsilon}_v = A_3 \cdot 9.74 \cdot 10^{-4} \phi^{2.589} \exp\left(\frac{-Q_{ps}}{RT}\right) \frac{\bar{\sigma}}{Td^3} \quad (\text{Eq. 2.11})$$

where A_3 is in the range of $3.76 \cdot 10^{-15} - 3.76 \cdot 10^{-13} \text{ K m}^3 \text{ MPa}^{-1} \text{ s}^{-1}$. Experiments are necessary to test the sensitivity to humidity predicted here. In addition, a microphysical framework to account for the decrease in strain rates at low porosities may help in further constraining the creep rates.

Table 2-1: Overview of quantities measured by Koelemeijer et al. 2012 as a function of relative humidity, including effective surface diffusivity.

| | Absolute Humidity 1–8 (g/m ³) | Absolute Humidity 8–14 (g/m ³) | Absolute Humidity 14–18 (g/m ³) |
|---|---|--|---|
| Relative humidity (%) | 4–35 | 35–60 | 60–78 |
| Typical impedance amplitude (Ω) | 8×10^{11} | 5×10^{10} | 8×10^6 |
| Surface resistance (Ω) | $2 \times 10^{14} - 1 \times 10^{13}$ | $2 \times 10^{13} - 9 \times 10^9$ | $2 \times 10^9 - 2 \times 10^6$ |
| Effective surface diffusivity ($\text{m}^3 \text{ s}^{-1}$) | $1 \times 10^{-27} - 3 \times 10^{-26}$ | $1 \times 10^{-26} - 3 \times 10^{-23}$ | $1 \times 10^{-22} - 1 \times 10^{-19}$ |
| Assumed thickness (nm) | 1–10 | 10–50 | 50–90 |
| Diffusivity ($\text{m}^2 \text{ s}^{-1}$) | $1 \times 10^{-18} - 1 \times 10^{-17}$ | $2 \times 10^{-17} - 4 \times 10^{-15}$ | $1 \times 10^{-14} - 8 \times 10^{-12}$ |

^aThe results are grouped into three humidity ranges and typical values are given to demonstrate the general trends.

2.2.3 Composite creep behavior

In salt, as in all crystalline materials, different deformation mechanisms, represented by different steady state creep equations, may dominate at different conditions, and can be represented using deformation mechanism maps (e.g. Frost and Ashby 1982; Khaledi et al. 2016; Spiers & Carter 1998; Urai et al. 1987). Deformation maps show the dominant deformation mechanisms (mechanisms with largest contribution to overall strain rate) under a range of conditions (stress and temperature). The deformation map for dense salt is given in Figure 2-5. The total strain rate of a material is then given by the sum of the strain rates of all the individual mechanisms. In practice, in the centre of a field in a deformation map, one single mechanism accounts for most of the total strain under a given set of conditions and creep rates can be approached using a single mechanism only. Near the boundary of the fields in a deformation map, the creep rate can be approached by the sum of the strain rates of the two mechanisms, leading to two mechanisms occurring in parallel (i.e. leading to composite creep behaviour). Most of these deformation maps are based on experiments on dense rock salt under deviatoric creep, but the same mechanisms have been identified in controlling compaction creep in granular rock salt (e.g. Spiers et al. 1990; Zhang et al. 2007). In porous salt, the grain scale stresses are intensified, causing the boundaries between the mechanisms to move towards higher stresses, with respect to the deformation map in dense salt (Figure 2-5). Hence, pressure solution creep is expected to be dominant under a broader range of conditions in granular compaction creep as opposed to dense deviatoric creep shown in Figure 2-5.

While dislocation creep mechanisms are grain size insensitive (GSI), diffusion creep laws are known to be grain size sensitive (GSS) processes. Typical microstructures of rock salt samples deformed in the laboratory may show evidence of several deformation mechanisms, such as (a) climb-controlled dislocation creep and/or (b) pressure solution creep alongside (c) grain boundary sliding, possibly in combination with (d) fluid-assisted grain boundary migration (i.e. dynamic recrystallization).

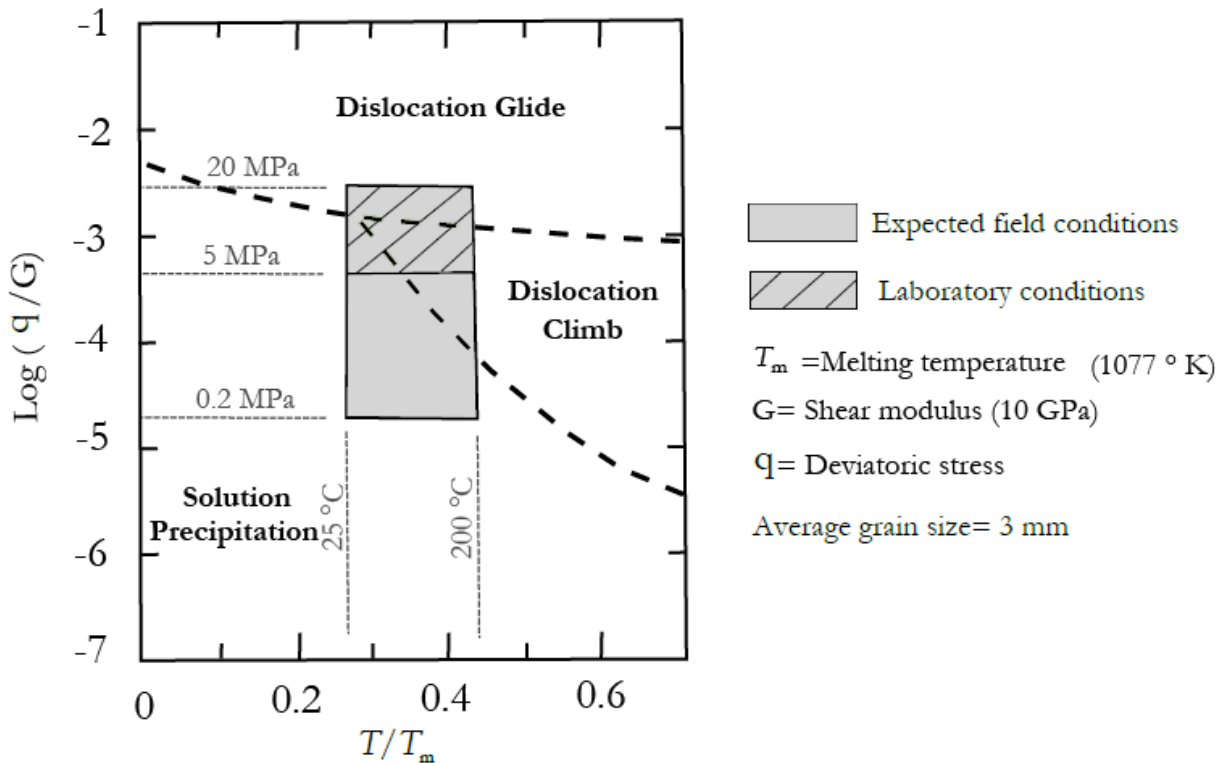


Figure 2-5. Deformation mechanism map of rock salt plotted as stress normalized to the shear modulus vs. temperature, for a grain size 3 mm and intergranular fluid pressures of 10 MPa (taken from Khaledi et al. 2016). Note that deformation mechanism map is based on creep in dense rock salt. The presence of porosity in granular backfill and the decrease in grain size will cause the boundaries to move towards higher stresses and solution-precipitation creep (i.e. pressure solution) will become dominant over a broader range of conditions.

2.3 Recrystallization (Stage II and III)

In addition to creep mechanisms, recrystallization may take place in natural salt and in backfill during or after deformation. Recrystallization is the transformation of the grain structure without any chemical changes and can either occur during deformation (dynamically) or after deformation (statically) (Guillope & Poirier 1979). Dynamic recrystallization may play a role in backfill during compaction creep (Stage II). Static recrystallization occurs after deformation or when the porosity is low and compaction creep rates become negligible (Stage III). Both mechanisms are driven by the excess potential energy stored in dislocations, where grains with a low internal energy consume grains with a higher internal energy (Guillope & Poirier 1979). This results in rotation of subgrains (at low temperature and stresses) and migration of grain boundaries (at higher temperatures and stresses or in the presence of water). Grain boundary migration is strongly accelerated by the presence of fluid and is an important mechanism in rock salt

that can weaken rock salt and may accelerate creep (Peach et al. 2001; Schlöder & Urai 2005; Ter Heege et al. 2005a).

2.4 Static healing mechanisms (Stage III)

The majority of research on the mechanical behavior and transport properties of salt is directed at dense rock salt and rock salt backfill (Hunsche & Hampel 1999; Senseny et al. 1992), at microcrack damage production in the EDZ (Peach & Spiers 1996; Popp & Kern 2000) and at its reduction by mechanical crack closure (Hou et al. 2012). Relatively little has been done on crack and pore healing/sealing effects in salt when deformation/closure rates have fallen to negligible values, i.e. by pore reconfiguration towards a thermodynamic equilibrium state (equilibrium dihedral wetting angles and associated connectivity) due to interfacial and strain energy minimization through diffusive mass transfer. Exceptions include the work by Houben et al. 2013, who showed that diffusion controlled healing of cracks results in crack disconnection on a timescale of a few years at laboratory humidity levels, but much longer times under very dry conditions and the work by Holness & Lewis 1997 who showed that salt rock becomes permeable at high pressure-temperature conditions ($> \sim 100 \text{ MPa}$ for a geotherm in a sedimentary basin), as the equilibrium dihedral angle under these conditions is lower than 60° . However, these conditions are not reached in a repository. Furthermore, it is likely that variations in dislocation density result in anisotropy in surface energy, causing local departures from equilibrium, which cast doubt on their assessment under which conditions granular salt should be permeable or impermeable (e.g. Sinn et al. 2018).

Important to note here is that compaction experiments on wet granular salt by Zhang et al. 2007 indicate that at a porosity of 1% creep rates become negligible while a permeability of 10^{-17} m^2 is measured. Natural undisturbed rock salt has a permeability of about 5 orders of magnitude lower (Peach & Spiers 1996). This is due to generally even lower porosity but also to the fact that brine-bearing pores, cracks and grain boundaries have healed to form isolated inclusion arrays. Hence, healing processes are expected to control the long-term permeability evolution in backfill during stage III when porosities are low (a few %) and compaction has more or less ceased. However, these healing and sealing processes are unlikely to be detected in mechanical experiments when the porosity and compaction rate are still significant ($>5\%$). Besides mechanical closure associated with compaction of damaged salt or salt backfill by dislocation creep or pressure solution creep processes (see Fig 2-6A), healing and sealing of pores, cracks and grain boundaries can occur by two different mechanisms (Houben et al.2013):

(1) Diffusive crack healing driven by surface energy reduction, which involves necking down of pores, cracks and grain boundary brine films to form isolated, sub-spherical inclusions (Chen et al. 2013; Houben et al. 2013b; Schutjens & Spiers 1999) – Figure 2-6B. Here, transport of material occurs by diffusion through thin adsorbed water films on the solid surface or through a liquid brine phase if the voids are completely brine filled cracks;

(2) Recrystallization involving fluid-assisted grain boundary migration, leaving sub-spherical inclusions behind (Schmatz & Urai 2011; Ter Heege et al. 2005a) – Figure 2-6C. In this case, the driving force is dislocation stored energy remaining from earlier plastic deformation.

Based on crack surface diffusivity in the presence of adsorbed water layers, Houben et al. 2013 estimated that individual cleavage cracks in NaCl can be expected to become disconnected on a timescale of a few years at laboratory humidity levels. However, much longer timescales are needed under low humidity conditions, where adsorbed films in salt are very thin. Under truly dry conditions, it is expected that healing cannot operate as temperatures for dry grain boundary diffusion are not reached in the repository. But unless actively maintained such conditions are not expected in the repository, certainly not in the post-operational stage.

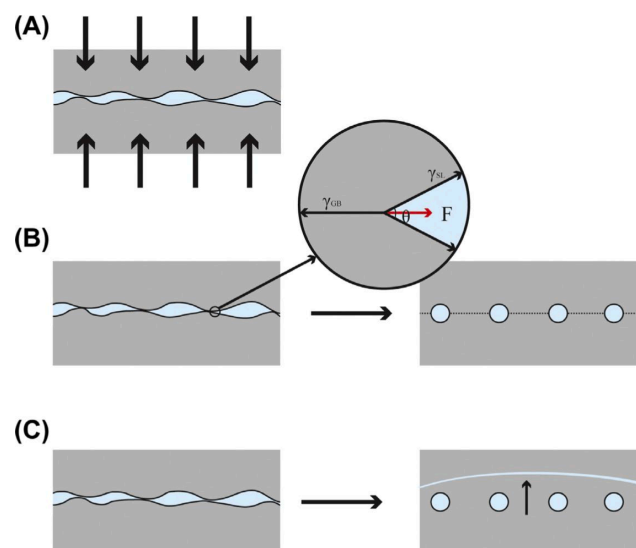


Figure 2-6: physical mechanisms by which crack healing/sealing and permeability reduction can occur. (A) mechanical closure of cracks. (B) necking down of crack pores to form isolated inclusions by means of surface-energy driven mass transport and (C) crack and pore occlusion through fluid-assisted grain boundary migration (recrystallization). After Houben et al. (2013).

3 Previous experimental work on compaction creep in rock salt backfill

The previous sections give a detailed overview of the conditions expected in a backfilled repository in salt rock and the mechanisms controlling the mechanical behavior in the salt rock, in particular the compaction of the backfill under these conditions. Experiments have been carried out over the past decades to determine convergence rates under a range of conditions (e.g. Bechthold et al. 1999; Czaikowski et al. 2020), porosity-permeability relations (e.g. Bechthold et al. 1999; Zhang et al. 2007) and, in some cases, to identify mechanisms controlling convergence creep of backfill (e.g. Mills et al. 2018; Zhang et al. 2007). The aim of this section is to give an overview of earlier experimental work used to derive constitutive models for backfill compaction (Callahan & Hansen 1999; Korthaus 1996; Sjaardema & Kreig 1987) and to give an overview of more recent experiments on backfill compaction (Bechthold et al. 1999; Kröhn et al. 2009; Krohn et al. 2017; Stührenberg 2013; Zhang et al. 2007). The more recent experiments are used to show the state-of-the-art mechanical data. The results of these more recent experiments have been used to calibrate the earlier derived constitutive laws and along with the data on pressure solution creep at low stresses and low porosities (Zhang et al. 2007) are used to provide a basis for an evaluation and the recommendations on laws to be used for modelling repository convergence (see Section 4).

3.1 Overview of experimental techniques

The laboratory investigations on backfill carried out in the past years have been extensively documented in the literature (Bechthold et al. 1999; Kröhn et al. 2009; Krohn et al. 2017; Stührenberg 2013; Zhang et al. 2007). There are mainly three type of experimental setups that have been used to determine mechanical behavior:

- i) Oedometer test: 1D compaction at constant load or constant strain rate (e.g. Kröhn et al. 2015; Stührenberg 2017). The advantage of this method is that the shape and the volume of the sample can be measured exactly. However, this type of experiments is bound in the lateral direction, without the ability to measure lateral stresses. Whereas the in-situ backfill compaction will be 3D with near isotropic stresses.
- ii) Isostatic triaxial test: 3D compaction at constant load (e.g. Krohn et al. 2017; Mills et al. 2018; Stührenberg 2013). The advantage of this is that the 3D stress state is known, it is similar to the in-situ loading geometry in the repository and it is possible to apply a deviatoric stress.

- iii) Stress relaxation experiments: 1D compaction at a fixed position, with dissipating load (e.g. Zhang et al. 2007). The stress relaxation behavior is due to creep in the sample, as the elastic strain in the sample plus elastic distortion of the apparatus are converted into permanent deformation of the sample. The advantage of the relaxation method is that one can experimentally determine a relationship between flow stress and flow rate of the sample and smaller strains are required to measure a significant strain rate.

Another key difference is that experiments performed by IfG (Institute für Gebirgsmechanik GmbH) (Czaikowski et al. 2020), BGR (Stührenberg 2013), TUC (Technical University Clausthal) (Czaikowski et al. 2020) and Sandia national laboratory (Mills et al. 2018) were performed on a mixture with a grain size distribution ranging from 0.1 mm – 10 mm (e.g. KOMPASS mixture, see Figure 3-1). While the experiments at UU (Utrecht University) (Zhang et al. 2007) were performed on single grain sizes (range: 50-560 μm ; standard deviation: $\pm 12\text{-}25 \mu\text{m}$). The large grain size fractions also require larger samples for representative measurements, which leads to a range in sample sizes ranging from a length of 780 mm/diameter of 514 mm (IfG big compaction cell) to a length of 10 mm/diameter of 20 mm (Zhang et al. 2007).

| Material-fraction | Grain size distribution $d_5\text{-}d_{95}$ [mm] | d_{50} [mm] | m [-] | Optimized mixture [wt.-%] |
|--|--|---------------|-------|---------------------------|
| Überkorn (ÜK) – oversized grains | 3 - 10 | 6.03 | 3.44 | - |
| Band 6 (B6) – production line 6 | 0.4 - 4 | 1.90 | 2.06 | 65.6 |
| Band 8 (B8) – production line 8 | 0.1 - 1 | 0.49 | 1.58 | 20.2 |
| Feinsalz (FS) – fine salt | 0.03 - 0.3 | 0.14 | 2.01 | 14.2 |
| | | | sum | 100.0 |
| Materials from other investigations or sources | | | | |
| REPOPERM | 0.1 - 30 | 2.35 | 0.81 | |
| ESCO - salt | 0.1 - 8 | 1.48 | 1.02 | |

Figure 3-1: Grain size fractions in the raw mixture retrieved from the GSES and the optimized KOMPASS mixture with oversized grains taken out and the three other fractions mixed in the ratio's 65.6:20.2:14.2.

3.1.1 Pre-compaction techniques

Without any compaction, the loose backfill has an initial porosity $> 40\%$. The initial stage of in-situ compaction of the backfill will be very slow as the repository walls have to converge before a significant load is reached. Most of the experiments are aimed at investigating compaction creep at intermediate (5-20%) porosities and ideally also in the low porosity range (0.1-5%). To speed up this process, most samples were first pre-compacted to a desired porosity either at constant strain rate (BGR experiments, e.g. TK-

031 & TK-033 and UU experiments) or constant loads. In both cases, implying unrealistic high loads for the initial stage of compaction, which potentially could result in microstructural changes that affect the later mechanical behavior during the actual compaction experiments. Hence, samples were pre-compacted using stepped axial load (IfG experiments, Appendix A5, e.g. TCC1-6) (Stührenberg 2013, Czaikowski et al. 2020) or plane strain compaction (TUC, Appendix A6) with the long axis fixed (Czaikowski et al. 2020). For future work, pre-compaction at higher temperatures is considered at Utrecht University to decrease the stress required to get to intermediate and low porosities.

3.2 Mechanical data and constitutive models

In the 1990's, a range of compaction experiments have been performed on granular backfill to determine the strain rate dependence on stress for a range of stresses and obtain basic constitutive laws (e.g. Callahan & Hansen 1999; Hein 1991; Korthaus 1996; Sjaardema & Kreig 1987). The grain size in these tests typically was coarser than later backfill recipes (e.g. KOMPASS mixture), with 75% larger than 0.5 mm (Korthaus 1996) or a mean grain size of 1 mm (Callahan & Hansen 1999) and porosities in the range of 13-30%. These experiments indicated stress exponents of 5-7 (Korthaus 1996) and 5-5.5 (Callahan & Hansen 1999; Sjaardema & Kreig 1987) and all incorporate empirical functions to incorporate the decrease in strain rates with decreasing porosity. The model derived by Korthaus 1996 has been modified several times and an updated version is known as the BGR-CS3 model, containing recent modifications including a humidity creep term (Krohn et al. 2017); the model by Callahan & Hansen 1999 has been modified to account for a linear pressure solution creep term and is known as the Callahan model; and the model of Sjaardema & Kreig 1987 has become known as the C-WIPP model. An overview of the constitutive laws used in these three models is presented in Appendix A1-A3.

More recent experiments (Krohn et al. 2017; Kröhn et al. 2015) have been conducted to further calibrate these existing models and obtain mechanical data at low porosities (<10%) and in mixtures with smaller grain sizes (see Table 3-1 and Table 3-2). Both long-term creep tests at ambient temperatures and short-term stress relaxation tests have been carried out over recent years to obtain mechanical data for a range of conditions. An overview of the conditions and the experimental results of these more recent experiments are given in Table 3-1 and Table 3-2. A detailed description of the experimental method and results for each of these experiments as well as microstructural data are given in the Appendix A4-A8.

The long-term experiments (Czaikowski et al. 2020; Krohn et al. 2017; Kröhn et al. 2015) have all been performed on grain size mixtures, with roughly comparable grain size distribution (e.g. KOMPASS, DEBORA). Strain rates vary from $10^{-7} s^{-1} - 10^{-11} s^{-1}$, with porosity decreasing from $\sim 40\%$ to 1% , while stress is increased from $\sim 1-20$ MPa, in backfill saturated with brine or brine content added to the mixture. In backfill without added brine strain rates vary from $10^{-8} s^{-1} - 10^{-11} s^{-1}$, with porosity decreasing from $\sim 40\%$ to 8% , while stress was increased from $\sim 1-20$ MPa. A steady state is never reached, due to ongoing decrease of porosity. At the same porosity and stress, strain rates in dry experiments tends to be about 1-2 orders of magnitude slower, than for wet conditions.

Kröhn et al. 2015 note that their experimental results can be described by using the phenomenological (Norton) power law with a stress exponent of $n = 5$, but to account for the difference of 0.5 order of magnitude between a lab-dry or oven-dried experiment, a term must be introduced to describe the effect of humidity, which later has been added to improved constitutive models (Krohn et al. 2017). In the other long-term experiments (Czaikowski et al. 2020; Krohn et al. 2017) the mechanical data is not explicitly tested in terms of strain-rate dependence of stress (e.g. stress exponent), but the experiments are only used to further calibrate constitutive laws derived from earlier experiments (e.g. Callahan & Hansen 1999; Hein 1991; Korthaus 1996).

As an example, the mechanical data of compaction test TK-031 is shown in Figure 3-2. Compaction test TK-031 included five loading stages with a mean stress of 10.3; 12.3; 15.3; 18.4 and 20.4 MPa, with creep phase durations of 7, 19, 26, 27 and 202 days respectively. The loading rate during each phase set between 1 and 3 MPa/day. The moisture content of the sample was equal to 0.05wt%. The strain rate during all loading stages varies from $10^{-8} - 10^{-9} s^{-1}$ from the beginning to the end of each loading stage. The final porosity after 300 days of compaction is equal to 7.5%.

Table 3-1: List of recent backfill compaction experiments of GRS (Kröhn et al. 2015), BGR (Krohn et al. 2017), IfG (Czaikowski et al. 2020), TUC (Czaikowski et al. 2020), Sandia (Mills et al. 2018) an Utrecht University (Zhang et al. 2007), indicating experiment type, conditions and differences in backfill properties. ^(a) First 1200 days with lab-air, subsequently flooded with 100% saturated brine. ^(b) Brine content added to backfill before start of experiment.

| Metadata | | | | Conditions | | | Backfill properties | |
|----------|----------|------------------------|-------------------|---------------------------|-----------|----------------------|---------------------|------------------------------|
| Inst. | Exp. | References | Experiment type | Pore fluid | Temp (°C) | Stress regime | Grain size (dist) | Brine content ^(b) |
| GRS | Sample 1 | Kröhn et al. 2015 | Creep test | Lab-air/fl ^(a) | 32-57 °C | Multistep 1D | dist (d<8 mm) | None |
| GRS | Sample 2 | Kröhn et al. 2015 | Creep test | Lab-air | 30-90 °C | Multistep 1D | dist (d<8 mm) | None |
| BGR | TK-031 | Kröhn et al. 2017 | Creep test | Lab-air | 50 °C | Multistep isostatic | DEBORA dist | 0.05 wt% |
| BGR | TK-033 | Kröhn et al. 2017 | Creep test | Lab-air | 50 °C | Multistep isostatic | DEBORA dist | 0.05 wt% |
| IfG | TCC1 | Czaikowski et al. 2020 | Creep test | Lab-air | 25 °C | Multistep isostatic | KOMPASS dist | None |
| IfG | TCC2 | Czaikowski et al. 2020 | Creep test | Lab-air | 25 °C | Multistep isostatic | KOMPASS dist | None |
| IfG | TCC3 | Czaikowski et al. 2020 | Creep test | Lab-air | 25 °C | Multistep isostatic | KOMPASS dist | None |
| IfG | TCC5 | Czaikowski et al. 2020 | Creep test | Lab-air | 25 °C | Multistep isostatic | KOMPASS dist | 1 wt% |
| IfG | TCC6 | Czaikowski et al. 2020 | Creep test | Lab-air | 25 °C | Multistep isostatic | KOMPASS dist | 1 wt% |
| TUC | TUC-V2 | Czaikowski et al. 2020 | Creep test | Lab-air | 30 °C | Multi iso+deviatoric | KOMPASS dist | 0.5 wt% |
| Sandia | W90-1 | Mills et al. 2018 | Creep test | Lab-air | 90 °C | Isostatic | dist (d<9.5 mm) | None |
| Sandia | W90-2 | Mills et al. 2018 | Creep test | Lab-air | 90 °C | Isostatic | dist (d<9.5 mm) | 1 wt% |
| Sandia | W90-4 | Mills et al. 2018 | Creep test | Lab-air | 90 °C | Isostatic | dist (d<9.5 mm) | 1 wt% |
| Sandia | W90-7 | Mills et al. 2018 | Creep test | Lab-air | 90 °C | Isostatic | dist (d<9.5 mm) | 1 wt% |
| Sandia | W90-8 | Mills et al. 2018 | Creep test | Lab-air | 90 °C | Isostatic | dist (d<9.5 mm) | None |
| Sandia | W175-1 | Mills et al. 2018 | Creep test | Lab-air | 175 °C | Isostatic | dist (d<9.5 mm) | None |
| Sandia | W250-1 | Mills et al. 2018 | Creep test | Lab-air | 250 °C | Isostatic | dist (d<9.5 mm) | None |
| Sandia | W250-2 | Mills et al. 2018 | Creep test | Lab-air | 250 °C | Isostatic | dist (d<9.5 mm) | None |
| Sandia | A250-1 | Mills et al. 2018 | Creep test | Lab-air | 250 °C | Isostatic | dist (d<9.5 mm) | None |
| Sandia | A250-2 | Mills et al. 2018 | Creep test | Lab-air | 250 °C | Isostatic | dist (d<9.5 mm) | 1 wt% |
| UU*** | CP1 | Zhang et al. 2007 | Stress relaxation | Lab-air | 21 °C | 1D compaction | 412 µm | None |
| UU | CP3 | Zhang et al. 2007 | Stress relaxation | Decane | 21 °C | 1D compaction | 412 µm | None |
| UU | CP4 | Zhang et al. 2007 | Stress relaxation | Argon | 21 °C | 1D compaction | 412 µm | None |
| UU | CP5 | Zhang et al. 2007 | Stress relaxation | Sa. brine | 21 °C | 1D compaction | 412 µm | None |
| UU | CP6 | Zhang et al. 2007 | Stress relaxation | Argon | 21 °C | 1D compaction | 70 µm | None |
| UU | CP8 | Zhang et al. 2007 | Stress relaxation | Sat. brine | 21 °C | 1D compaction | 412 µm | None |
| UU | CP9 | Zhang et al. 2007 | Stress relaxation | Lab-air | 21 °C | 1D compaction | 412 µm | None |
| UU | CP10 | Zhang et al. 2007 | Stress relaxation | Sat. brine | 21 °C | 1D compaction | 137 µm | None |
| UU | CP12 | Zhang et al. 2007 | Stress relaxation | Lab-air | 21 °C | 1D compaction | 137 µm | None |
| UU | Anl3 | Zhang et al. 2007 | Stress relaxation | Sat. brine | 21 °C | 1D compaction | 560 µm | None |
| UU | Anl13 | Zhang et al. 2007 | Stress relaxation | Sat. brine | 21 °C | 1D compaction | 137 µm | None |
| UU | Anl17 | Zhang et al. 2007 | Stress relaxation | Sat. brine | 21 °C | 1D compaction | < 50 µm | None |
| UU | Anl19 | Zhang et al. 2007 | Stress relaxation | Sat. brine | 21 °C | 1D compaction | < 50 µm | None |

Table 3-2: Overview of mechanical data of recent backfill compaction experiments from GRS (Kröhn et al. 2015), BGR (Krohn et al. 2017), IfG (Czaikowski et al. 2020), TUC (Czaikowski et al. 2020), Sandia (Mills et al. 2018) and Utrecht University (Zhang et al. 2007). (*) Due to the different nature of the stress relaxation experiments, one stress relaxation experiment contains multiple tests at different (initial) stress and porosity. The colours denote the stresses and initial/final porosities belonging to one experiment. The duration of stress relaxation experiments is typically 1 hour – 1 day, depending on stress, porosity and pore fluid. Note that the strain rates in the stress relaxation experiments are significantly higher than the creep test, because of smaller grain sizes (saturated conditions) and/or higher stresses (Argon dry conditions).

| Name | Duration | Mean eff. stress | Porosity | | | | Strain-rates (s ⁻¹) | Def. mechanisms | | | | |
|----------|-----------|---------------------|----------------------|-----|--------------------|-------|---------------------------------|-------------------------|--------------|--------------------|--------------|--------------------|
| | | (MPa) | Initial porosity (*) | | Final porosity (*) | | | | | | | |
| Sample 1 | 1350 days | 1-4-7-10-13-18 | 41.00% | | 11.50% | | 1E-7 - 3E-11 | "Disl creep + p-sol" | | | | |
| Sample 2 | 1350 days | 1-4-7-10-13-18 | 43.00% | | 1.00% | | 1E-7 - 3E-10 | "Dislocation creep" | | | | |
| TK-031 | 295 days | 10.3-15.3-18.4-20.4 | 16.48% | | 7.76% | | 7E-8 - 1.5E-9 | Not investigated | | | | |
| TK-033 | 400 days | 15.3-20.4 | 16.77% | | 5.08% | | 1.5E7 - 2.4E-9 | Not investigated | | | | |
| TCC1 | 197 days | 5.0-10.0-20.0 | 14.39% | | 11.09% | | 1.4E-9 - 3.4E-11 | Not investigated | | | | |
| TCC2 | 197 days | 10.0-20.0-30.0 | 15.60% | | 7.77% | | 3.4E-8 - 1.2E-10 | Not investigated | | | | |
| TCC3 | 197 days | 1.0-5.0-10.0 | 12.90% | | 11.70% | | 1.2E-9 - 2.3E-11 | Not investigated | | | | |
| TCC5 | 197 days | 5.0-10.0-20.0 | 16.00% | | 1.36% | | 1.2E-7 - 3.5E-10 | Not investigated | | | | |
| TCC6 | 197 days | 1.0-5.0-10.0 | 16.21% | | 0.88% | | 9.0E-8 - 2.3E-10 | Not investigated | | | | |
| TUC-V2 | 150 days | 4.0-8.0-16.0-20.0 | 16.70% | | 9.50% | | 7.5E-8 - 8.7E-10 | Not investigated | | | | |
| W90-1 | 111 days | 20 | ~20% | | 8.33% | | Not calculated | Cataclasis + plasticity | | | | |
| W90-2 | 16 days | 20 | ~20% | | 1.89% | | Not calculated | Pressure solution | | | | |
| W90-4 | 5 days | 20 | ~20% | | 4.45% | | Not calculated | Pressure solution | | | | |
| W90-7 | 21 days | 20 | ~20% | | 2.67% | | Not calculated | Pressure solution | | | | |
| W90-8 | 3 days | 20 | ~20% | | 3.44% | | Not calculated | Cataclasis + plasticity | | | | |
| W175-1 | 1 day | 20 | ~20% | | 4.55% | | Not calculated | Cataclasis + plasticity | | | | |
| W250-1 | 14 days | 20 | ~20% | | 1.55% | | Not calculated | Cataclasis + plasticity | | | | |
| W250-2 | 12 days | 20 | ~20% | | 1.67% | | Not calculated | Cataclasis + plasticity | | | | |
| A250-1 | 7 days | 20 | ~20% | | 1.78% | | Not calculated | Cataclasis + plasticity | | | | |
| A250-2 | 7 days | 20 | ~20% | | 0.78% | | Not calculated | Pressure solution | | | | |
| CP1 | N/A | 19, 44, 57 | 30% | 15% | 10% | 29.9% | 14.8% | 9.6% | ~1E-6 - 1E-8 | Disl creep + recr. | | |
| CP3 | N/A | 13, 38, 48, 38 | 30% | 15% | 10% | 8% | 29.9% | 14.9% | 9.6% | 7.6% | ~1E-7 - 1E-8 | Disl creep + recr. |
| CP4 | N/A | 26, 65 | 30% | 10% | | | 29.9% | 9.9% | | | ~3E-7 - 3E-8 | Dislocation glide |
| CP5 | N/A | 61, 61, 155 | 10% | 5% | 1% | | 8.7% | 3.6% | 0.5% | | ~3E-9 - 1E-8 | Pressure solution |
| CP6 | N/A | 47, 64, 94, 130 | 15% | 10% | 5% | 1% | 14.9% | 9.9% | 4.7% | 0.7% | ~5E-7 - 2E-8 | Dislocation glide |
| CP8 | N/A | 62, 59, 108 | 10% | 5% | 1% | | 8.6% | 3.6% | 1.0% | | ~8E-6 - 2E-8 | Pressure solution |
| CP9 | N/A | 125, 118 | 3% | 1% | | | 2.7% | 1.0% | | | ~5E-8 - 4E-8 | Disl creep + recr. |
| CP10 | N/A | 18, 22, 36, 37 | 25% | 20% | 15% | 10% | 24.7% | 19.6% | 14.3% | 9.2% | ~1E-5 - 1E-9 | Pressure solution |
| CP12 | N/A | 105 | 5% | | | | 4.2% | | | | ~3E-8 - 8E-7 | Disl creep + recr. |
| An13 | N/A | 95 | 5% | | | | 3.2% | | | | ~3E-6 - 3E-8 | Pressure solution |
| An13 | N/A | 50, 85 | 10% | 4% | | | 8.9% | 2.5% | | | ~8E-6 - 2E-8 | Pressure solution |
| An17 | N/A | 12, 70 | 10% | 4% | | | 9.7% | 3.7% | | | ~3E-5 - 5E-8 | Pressure solution |
| An19 | N/A | 62 | 5% | | | | 3.5% | | | | ~1E-5 - 4E-8 | Pressure solution |

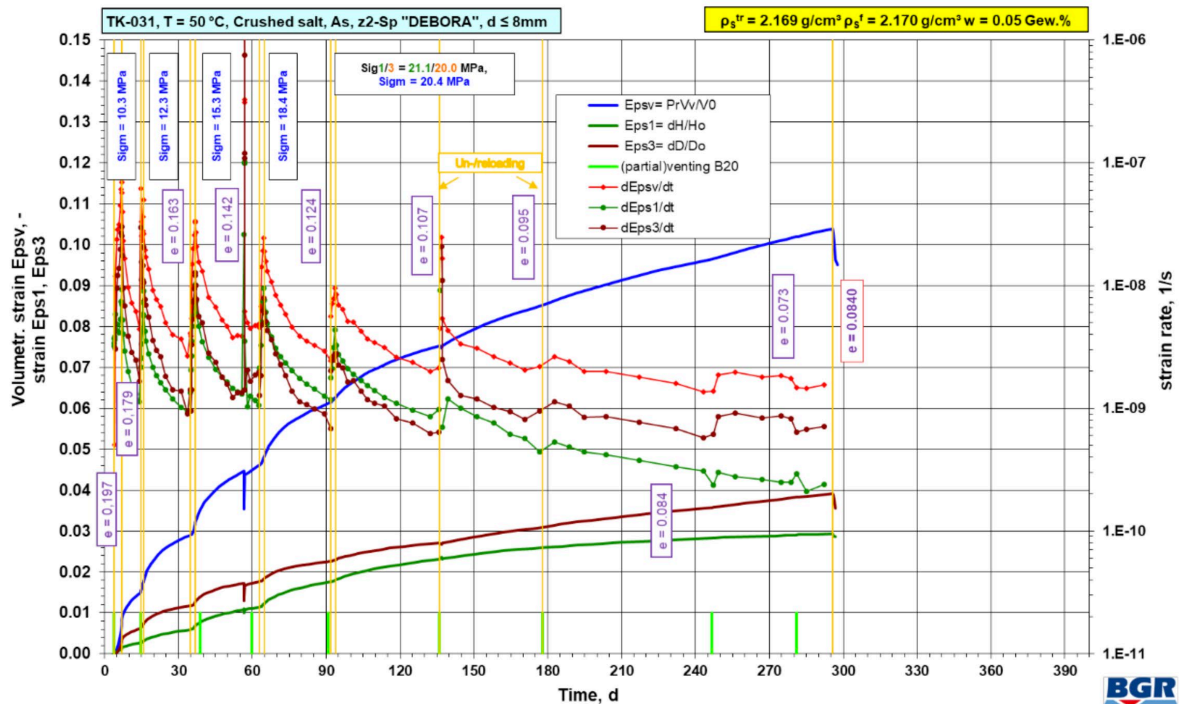


Figure 3-2: Development of strain and strain rate versus time in days for experiment TK-031 (Krohn et al. 2017). Note that strain rate is in the same range for all loading stages as the decrease in strain rates with decreasing porosity are compensated by an increase in stress.

A key issue with interpreting the long-term creep experiments in terms of stress-strain rate behavior is that there is ongoing porosity reduction during the experiments. Hence the changes in strain rate between each loading stage are not only caused by stress changes but also caused by a continuous decrease in porosity. Therefore, the individual effect of stress or porosity on creep rate cannot easily be determined and a switch to other mechanisms at lower porosity is not easily observed. Interpretation of the controlling mechanisms are further complicated by the use of a large grain size distribution, which activates multiple mechanisms and is expected to vary with sorting. Zhang et al. 2007 investigated the effect of lab-air, saturated brine and argon gas as pore fluid on the dominant deformation mechanism in fine grained granular salt at room temperature down to 1% porosity using stress relaxation experiments on narrow grain size fractions ($\pm 12.5 \mu\text{m}$) in the range 50-560 μm . Hence, it is expected that such a transition would also occur under humid conditions or when moisture is added to the mixture.

In the argon dry samples, the strain rates are very sensitive to stress. The average apparent n -value for the dry argon samples is about 20. Extrapolating these rates to low stresses $< 10 \text{ MPa}$, would result in negligible (10^{-23} s^{-1}) strain rates. The average n value of the lab air and decane filled samples is 5.1. In the saturated samples, the n values are exactly 1 at stresses less than 15-20 MPa, while at higher stresses the n value gradually transitions from 1-6. The deformation mechanism for the samples flooded with a

saturated solution is most likely pressure solution, given the n value and microstructural observations. Many studies on crushed rock salt and dense rock salt conclude that the steady state flow laws have a stress exponent of about 5. For example, the Norton creep laws (see Section A.1) which incorporates an n value of 5 based on compaction experiments of Korthaus 1996.

3.3 Porosity-permeability relations

In addition permeability measurements were obtained by Zhang et al. 2007, in which permeability was measured using decane for lab-air compacted samples and brine for samples compacted with saturated brine as pore fluid. The porosity-permeability data is shown in Figure 3-4a and b, for respectively decane and brine. The permeability data shows that the porosity-permeability evolution can be divided into three different porosity regions. These relations are shown in Figure 3-3 and can be described using Equation 10 ($\kappa = 1.13 \cdot 10^{-11} \phi^{2.80}$), when $\phi \geq 10\%$, Equation 11 ($\kappa = 6.54 \cdot 10^{-8} \phi^{6.99}$), when $4\% > \phi \geq 10\%$ and Equation 12 ($\kappa = 3.90 \cdot 10^{-16} \phi^{1.40}$) when $\phi \leq 4\%$.

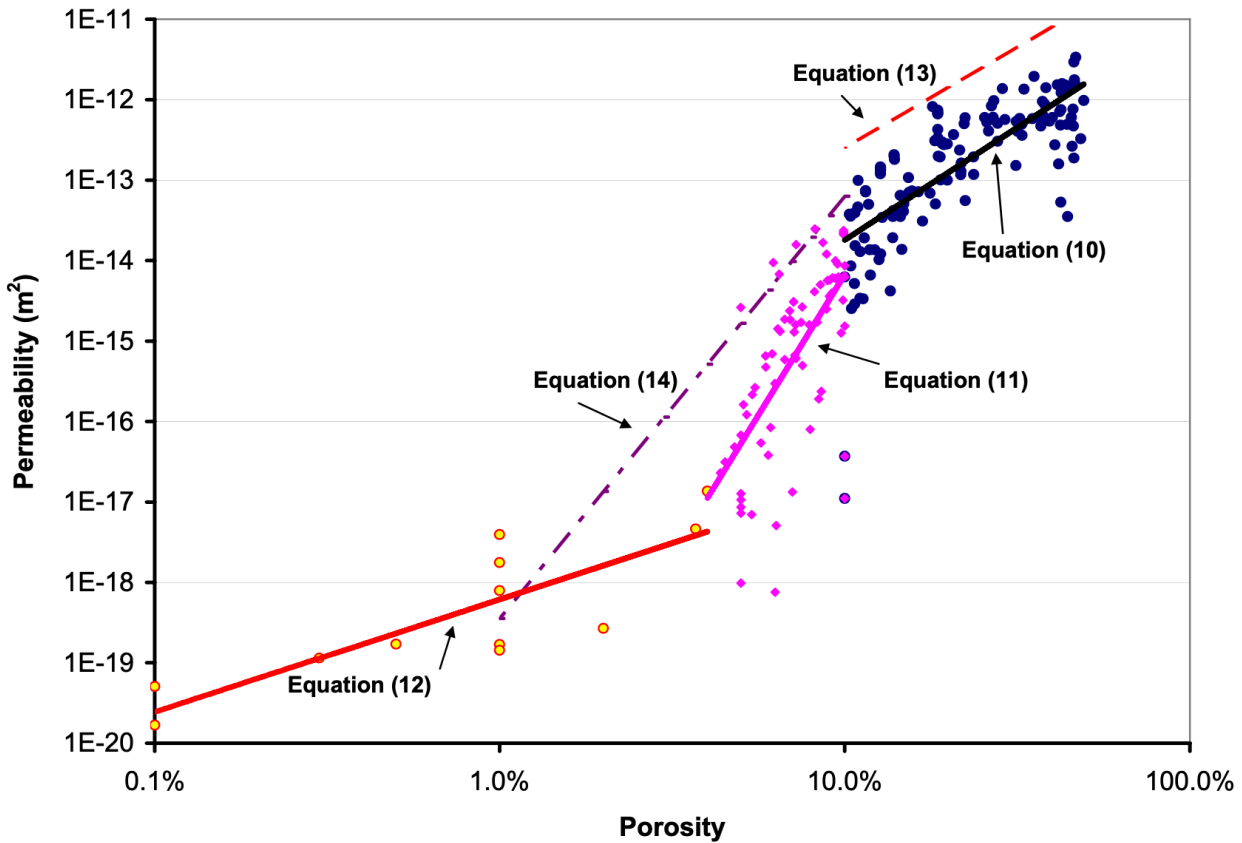


Figure 3-3: permeability-porosity relation for all measured permeability-porosity data (after Zhang et al. 2007). The dashed lines are from Bechthold et al. 1999.

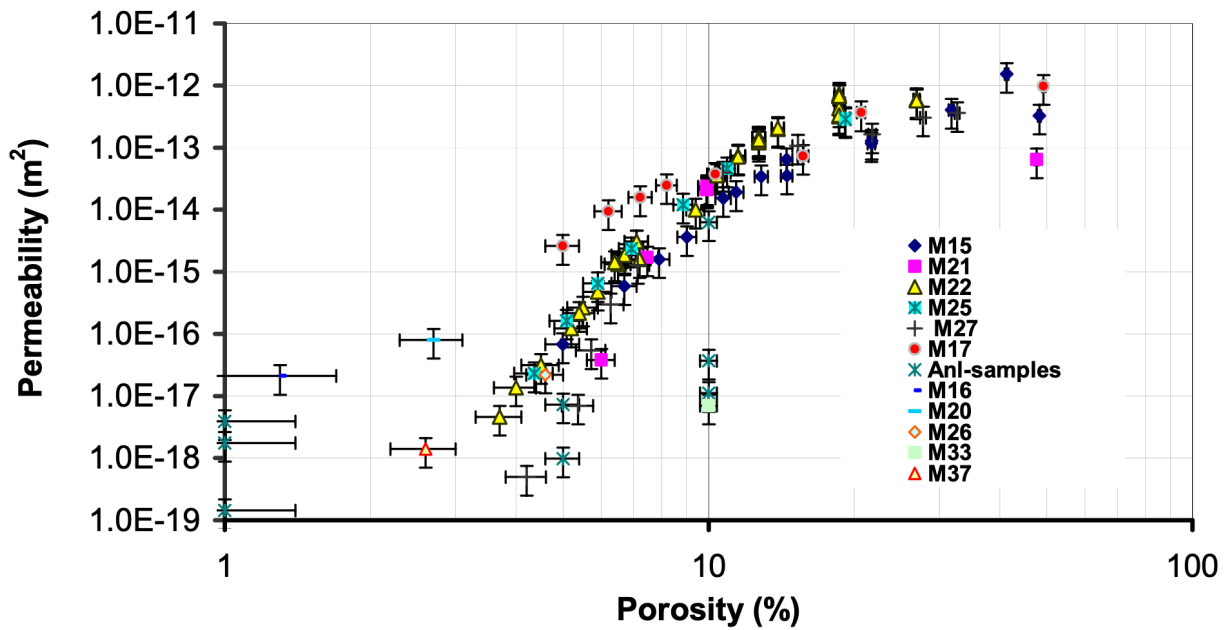
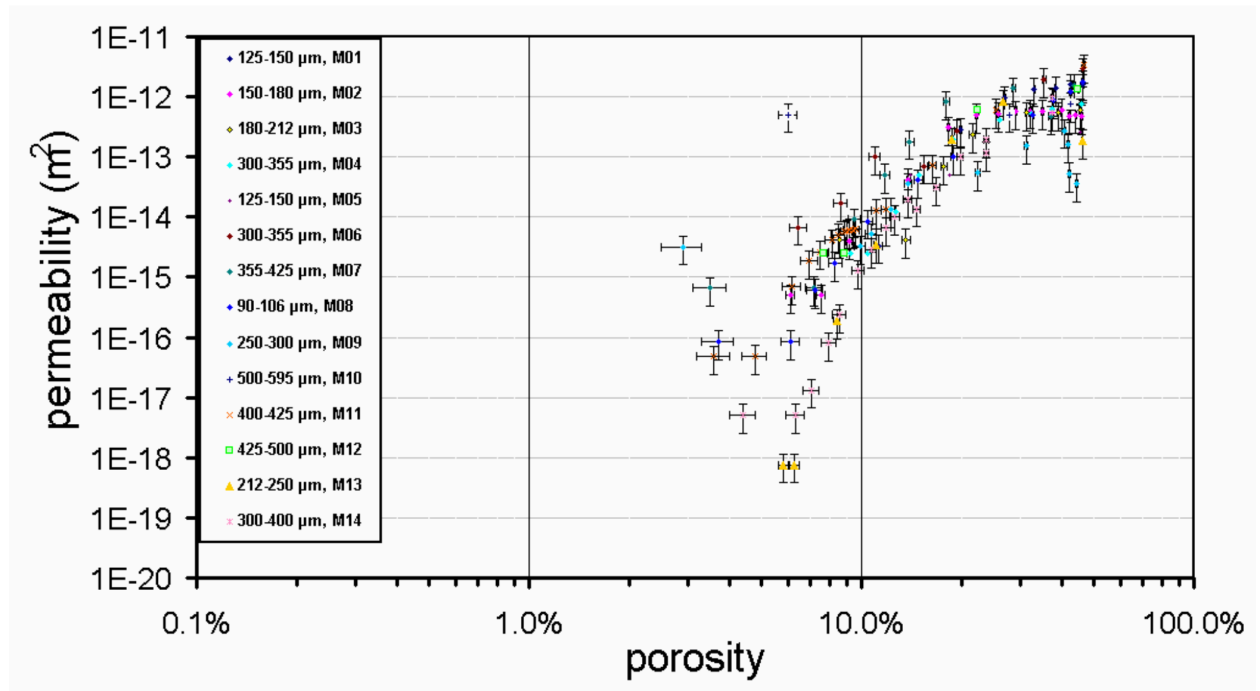


Figure 3-4: porosity-permeability data for (a) salt compacted with their pores filled with decane and (b) wet compacted salt (filled with saturated solution) (Zhang et al. 2007).

3.4 Evaluation of models and comparison on experimental data

The models discussed in Appendix A1-A3 have in common that they consider: (1) an elastic deformation part, based on porosity-dependent elastic properties, (2) a non-linear creep law accounting for the observed $n \approx 5 - 5.5$ behavior in laboratory experiments and (3) the phenomenological observations of a further decrease in strain rates at low porosity and a relative increase in strain rates (or lower n -value) at low stresses. In the BGR-CS3 and Callahan model this is explicitly considered as humidity creep, while in the other models this is not accounted for or implicitly taken into account by incorporating a function that allows for a changing stress-exponent (C-WIPP BGE-TEC). The BGR-CS3 and Callahan model allow for grain size (d, D_i , see Equation 4.3 and 4.4) and moisture content as input parameters. Only the BGR-CS3 model contains grain rearrangement due to fracturing. The C-WIPP models do not consider transient creep.

3.4.1 Effect of humidity and grain size distribution on pressure solution creep rates

The long-term experiments discussed in this report (Section 3 and Appendix A4-A8) have been performed on a mixture with an added moisture content. From impedance measurements on NaCl crystals by Koelemeijer et al. 2012 it becomes clear that the effect of relative humidity (hence moisture content) on effective surface diffusivity is in a range of 6 orders of magnitude from low humidity to high humidity. Hence, pressure solution creep rates can decrease by the same amount going from humid to near dry conditions (see Table 2-1). In practical for expected relative humidity under geological disposal conditions, this reduces to a range of 3 orders of magnitude (Koelemeijer et al. 2012). Hence, we suggest performing compaction experiments under a range of well-controlled humidity and test the effect of humidity on strain rates is necessary. Most of these experiments here are not under controlled humidity conditions. This can potentially explain the large range in compaction rates seen between experiments performed under similar conditions (e.g. TK-031 and TK-033, especially at the initial loading stages), as the backfill may take up moisture from the air during the experiment (Zhang et al. 2007). Another key point is that the KOMPASS mixture has a grain size range of 0.01 to 10 mm. For a mechanism which is known to depend on grain size ($\dot{\epsilon} \propto d^{-3}$), we suggest it is necessary to have a model that allows for calculating strain rates for a distributed grain size instead of a single grain size (e.g. BGR-CS3 and Callahan model). Which especially becomes relevant if experimental results are extrapolated to other grain sizes then for which experimental data is obtained.

Based on: (1) the grain size distribution of the KOMPASS mixture, (2) the pressure solution creep law of Spiers et al. 1990, (3) the observed porosity dependence of strain rates by pressure solution of Zhang et al. 2007 and (4) the effect of humidity on effective surface diffusivity of Koelmeijer et al. 2012, we have developed a preliminary model that for now only considers pressure solution as a mechanism. For a water content with a weight percentage of 1%, we expect nearly similar values as saturated conditions (e.g. TCC experiments, see Section A.5), a decrease of 1 order of magnitude for 0.5 wt% water (e.g. TUC-V2, Appendix A.6) and a decrease of 2-3 orders of magnitude for low humidity 0.05-0.5 wt% water (e.g. TK-031,TK-033, see Appendix A.4). The effects of humidity on creep rates will especially be important at low stresses, where dry creep mechanisms are significantly slower (Kröhn et al. 2015; Zhang et al. 2007). Considering that perhaps for the first ~100 years the effective stress on the backfill will very likely be well below 10 MPa (see Figure 2-1), it is likely that fluid or moisture assisted diffusional mechanisms will dominate during the begin of stage II.

3.4.2 Model comparison on experimental data

The models described in Appendix A1-A3 (except the BGR-CS3) have been compared on the experimental data of TUC-V2 (see Section A.6). The predictions on strain rate and porosity as a function of time in days are given in Figure 3-5. The loading history for this experiment is given in Figure A-10 and consists of isotropic and deviatoric loading cycles. An estimation for creep rates by pressure solution for humid conditions, based on the previous section is also added. All models predict strain rates in the right order of magnitude for the applied stress conditions and porosity range in this experiment. However, note that for the C-WIPP IfG model several parameters have been derived from the experiment itself and then used a fitting parameter and for the C-WIPP TUC, the model parameters have been adjusted to the test result using a least squares method fit (Czaikowski et al. 2020). While for the Callahan, BGE-TEC and UU models, no such fitting activity has been performed. Especially when applying models to the in-situ convergence of the backfill such fitting techniques will not be possible, certainly not when extrapolating to lower stresses, smaller porosities and different grain size distributions.

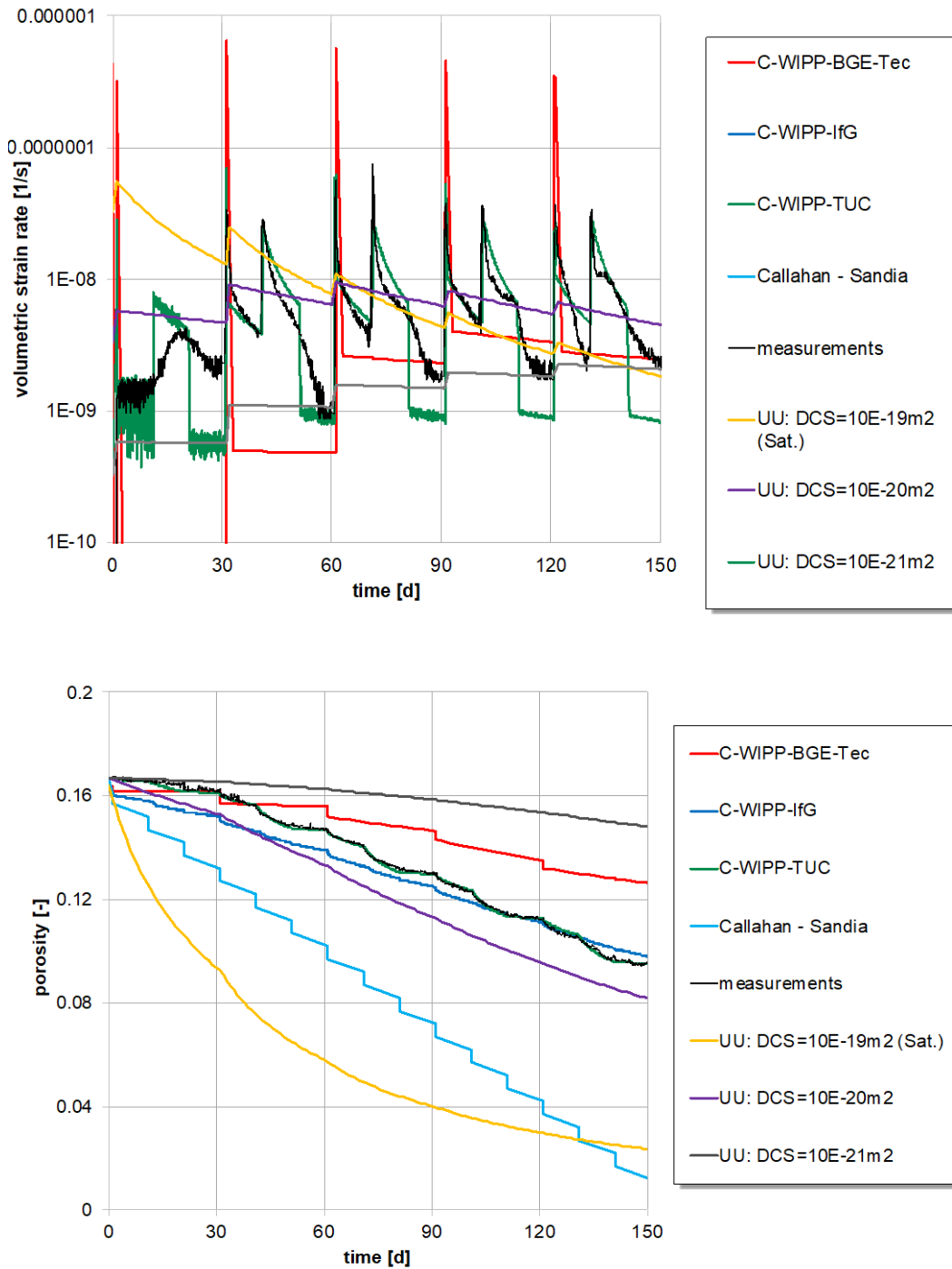


Figure 3-5: Comparison of model results with experimental data for TUC-V2. (a) showing volumetric strain rate (/s) versus time (days), and (b) showing porosity (-) vs time (days). Measured volumetric strain rate and porosity of experiment TUC-V2 is indicated in black. The loading history of the experiment contains isostatic and deviatoric loading parts. For the loading history of the experiment see Figure A-10. As an indication, preliminary predictions for the modified pressure solution creep model are given (Section 3.4.1). These lines indicate strain rate and porosity evolution expected for flooded conditions (yellow line) ($DCS = 10^{-19}m^3s^{-1}$) and for effective surface diffusivity expected at the given moisture content (0.5wt% water for this experiment, purple line) ($DCS = 10^{-20}m^3s^{-1}$).

4 Recommendations for modelling gallery convergence and internal backfill evolution

As discussed in the preceding sections, Stage II convergence of a backfilled opening in a radioactive waste repository, such as a gallery or borehole, represents a coupled problem in which the rate of convergence and backfill compaction are simultaneously determined by the creep behavior of the host salt rock and by the compaction behavior of the backfill. Convergence is driven by the difference between the lithostatic stress in the salt rock and the resistance to compaction (mean stress) that gradually builds up in the backfill as porosity decreases (Bechthold et al. 1999; Czaikowski et al. 2020; Kröhn et al. 2015). When the resistance to compaction offered by the backfill becomes high enough, the convergence and compaction rate will become negligible and any remaining porosity and permeability is expected to be modified primarily by pore reconfiguration and disconnection effects (Stage III).

Based on our analysis in Sections 3, we now provide preliminary recommendations regarding salt rock creep and backfill compaction laws suitable for modelling the coupled convergence-compaction problem in Stage II, by numerical means (e.g. Krohn et al. 2017; Prij 1991). We do not conduct such a modelling exercise but rather explore the likely timescale on which Stage II convergence can be expected to reduce backfill porosity to values of the order of 1% and corresponding permeabilities of $10^{-19} - 10^{-17} m^2$ (Section 3.3). A porosity of 1% is chosen as representing the end of Stage II convergence on the basis that the volume of free brine present in the salt backfill will typically be around 1 vol % (about 0.5 wt % for the brine/salt system – e.g. the KOMPASS backfill mix), which means that in a sealed repository the brine pressure will increase and the mean effective stress driving backfill compaction will fall towards zero as a porosity of 1% is approached. Our exploration of the timescale to reach this porosity is conducted by assuming a variety of highly simplified stress evolution paths within the backfill, instead of computing the stress-strain evolution numerically. We also present some preliminary considerations on how permeability is likely to evolve in Stage III.

The key aim of the remainder of the present UU-COVRA project is to provide new, improved, microphysically based models for backfill compaction (Stage II) that fully account for grain size and humidity effects, and to quantify, for the first time, how permeability evolves with time in Stage III, due to (near-)static pore reconfiguration. To obtain an accurate estimate of the timescale to reach specific backfill porosity/permeability levels, these improved material models (and associated uncertainties) still need to be incorporated in analytical or numerical computations of the

coupled convergence problem, e.g. by COVRA or in the framework of the KOMPASS II research program (Friedenberg et al. 2022).

4.1 Recommended creep laws for intact rock salt – the host rock around an opening (Stage I and II)

For the host rock surrounding an opening such as a gallery or borehole, we suggest using a simple two-mechanism creep law consisting of a power law part representing dislocation creep (after Hunsche & Hampel 1999) and a linear part representing pressure solution creep (after Spiers et al. 1990) for intact dense salt (following the microphysical approach adopted by Spiers et al 1990, Spiers & Carter 1998, Urai & Spiers 2007). These are given by:

$$\dot{\epsilon} = A_{dc} \exp\left(\frac{-Q_{dc}}{RT}\right) \sigma_{eq}^5 \quad \text{Eq. 5.1}$$

for dislocation creep, in which A_{dc} is a material parameter with a value of $2.1 \cdot 10^{-6}$ ($MPa^{-5}s^{-1}$), Q_{dc} is the activation energy for dislocation creep with a value of 54 ($kJ mol^{-1}$) and σ_{eq} is the Von Mises equivalent (deviatoric) stress in MPa ; and:

$$\dot{\epsilon} = A_{ps} \exp\left(\frac{-Q_{ps}}{RT}\right) \frac{\sigma_{eq}}{Td^3} \quad \text{Eq. 5.2}$$

for pressure solution creep, where A_{ps} is a combined geometric and material parameter with a value of $3.8 \cdot 10^{-13}$ ($MPa^{-1}s^{-1}Km^3$), Q_{ps} is the activation energy for pressure solution with a value of 24.53 ($kJ mol^{-1}$) and d is the grain size in m (for which a range of 2-10 mm can be used, typically 5 mm). Note that, in the EDZ around an opening, the effective grain size of salt rock may be reduced by perhaps a factor 2, in which case pressure solution creep rates may be up to one order of magnitude higher. For initial purposes, though, this can be neglected as the EDZ is generally only of the order of 1 m thick (Rutqvist et al. 2009; Tsang et al. 2005). Equations 5.1 and 5.2 accordingly represent our preliminary recommendations for describing the steady state creep behavior of intact salt host rock during both Stage I and Stage II convergence, and during any minor stress-strain changes occurring in Stage III – see Table 5.1.

4.2 Recommendation for modelling backfill compaction (Stage II)

For compaction of the backfill during Stage II, we suggest an equivalent two-mechanism constitutive law consisting of:

- i) a modified version of the BGR-CS3 model (Section A.1) to cover dislocation creep occurring in the backfill, specifically the hydrostatic part as the effect of deviatoric stress on volumetric strain rates is expected to be negligible in a more or less uniformly compacting aggregate (see Section 0), combined with
- ii) a humidity-assisted diffusion creep or pressure solution compaction equation to account for the effect of brine or humidity on effective surface diffusivity (see Sections 2.2.2 & 3.4.1).

The power law part of the simplified BGR-CSR model for hydrostatic stresses (Hein 1991; Umwelt & Korthaus 1998) reduces to:

$$\dot{\varepsilon}_{v-N} = A_N \exp\left(\frac{-Q_N}{RT}\right) (f_1(\phi) \bar{\sigma})^5 \quad \text{Eq. 5.3}$$

where ε_{v-N} is the volumetric creep rate in s^{-1} , A_N is a material parameter ($1.09 \cdot 10^{-6} s^{-1} MPa^{-5}$), Q_N is the apparent activation energy for creep ($54000 Jmol^{-1}$), $\bar{\sigma}$ is the mean Terzaghi effective stress (MPa) and $f_1(\phi)$ is an empirical porosity function given by:

$$f_1(\phi) = \left(\frac{0.01648}{\left(0.0003 - \frac{1}{\phi^{0.1} + \phi^{0.1}}\right)^{2.25}} \right)^{\frac{3}{5}} \quad \text{Eq. 5.4}$$

For the humidity-assisted or pressure solution creep component, we recommend using a modified version of the compaction creep equation given by Spiers et al. 1990 (see also Pluymakers & Spiers 2014), in which the theoretically- based effect of porosity on pressure solution creep rate (which breaks down at low porosities) is replaced by an empirically derived function determined from the experiments of Zhang et al. 2007 (see Figure A-17). The result obtained for compaction by pressure solution is given by:

$$\dot{\varepsilon}_{v-hum} = A_{hum} \exp\left(\frac{-Q_{ps}}{RT}\right) \frac{\bar{\sigma}}{Td^3} f_2(\phi) \quad \text{Eq. 5.5}$$

Here, $\dot{\varepsilon}_{v-hum}$ is the volumetric creep rate in s^{-1} , A_{hum} is a material parameter which will have a value in the range of $3.8 \cdot 10^{-15} - 3.8 \cdot 10^{-13} MPa^{-1} s^{-1} Km^3$, Q_{ps} is the activation

energy for pressure solution ($24.53 \text{ kJ mol}^{-1}$) and d is the grain size of the backfill. The porosity function $f_2(\phi)$ is given by:

$$f_2(\phi) = 9.74 \cdot 10^{-4} \phi^{2.589} \quad \text{Eq. 5.6}$$

Although, $f_2(\phi)$ has been fit to experimental data down to 1% porosity, using this porosity function to extrapolate strain rates to lower porosities (i.e. between 1% and 0.1%) remains open for debate. Note, that the range given for A_{hum} represents the range in the effect of effective grain boundary or surface diffusivity on pressure solution creep rates for intermediate relative humidities expected to be relevant for geological disposal conditions (RH=60-78%), as discussed in Section 2.2.2.2.

Table 4-1: Recommended creep laws for backfill and wall rock and porosity functions during Stage I, II and III. Stresses given in MPa.

| Stages | Creep law(s) | Porosity function | ϕ [%] | d [m] |
|-----------|---|--|---|---|
| Stage I | Wall rock $\dot{\epsilon}_{DC} = 2.1 \times 10^{-6} \exp\left(\frac{-54000}{RT}\right) \sigma_{eq}^5$ | - | 0-2% ^(a) | - |
| | Wall rock $\dot{\epsilon}_{PS} = 3.8 \times 10^{-13} \exp\left(\frac{-24530}{RT}\right) \frac{\sigma_{eq}}{Td^3}$ | - | 0-2% ^(a) | 2 ... 10 (5) mm |
| | Backfill No creep: open convergence | - | 40% | |
| | Backfill No creep: open convergence | - | 40% | |
| Stage II | Wall rock $\dot{\epsilon}_{DC} = 2.1 \times 10^{-6} \exp\left(\frac{-54000}{RT}\right) \sigma_{eq}^5$ | - | 0-2% ^(a) | - |
| | Wall rock $\dot{\epsilon}_{PS} = 3.8 \times 10^{-13} \exp\left(\frac{-24530}{RT}\right) \frac{\sigma_{eq}}{Td^3}$ | - | 0-2% ^(a) | 2 ... 20 (5) mm |
| | Backfill $\dot{\epsilon}_{v-N} = 1.09 \times 10^{-6} \exp\left(\frac{-54000}{RT}\right) (f_1(\phi) \bar{\sigma})^5$ | $f_1(\phi) = \left(1 / \left(\left[\frac{\left(\frac{\phi_0}{\phi}\right)^{0.1} - 1}{\phi_0^{0.1}}\right] + 0.0003\right)\right)^{\frac{2.25}{5}}$ | $\dot{\epsilon}_{v-tot} = -\dot{\phi}/1(-\phi)$ | 40-1% |
| | Backfill $\dot{\epsilon}_{v-hum} = 3.8 \times 10^{-14} \exp\left(\frac{-24530}{RT}\right) \frac{\bar{\sigma}}{Td^3} f_2(\phi)^{(c)}$ | | $f_2(\phi) = 9.74 \cdot 10^{-4} \phi^{2.589}$ | 85%: 0.1-0.5 mm 15%: 2-10mm ^(d) |
| Stage III | healing n/a ^(e) | - | <1% | - |

^(a) porosity of nearly zero in far field close, in EDZ up to 2% due to dilatancy

^(b) the exact porosity at which healing will dominate over compaction creep and stage III starts has to be determined

^(c) A_{hum} for humidity conditions at RH of 60-75%

^(d) e.g. we recommend KOMPASS mixture or KOMPASS mixture without intermediate fraction

^(e) static permeability evolution has to be determined

4.2.1 Preliminary order of magnitude calculations for backfill compaction during Stage II convergence.

Here, we explore the timescale on which Stage II convergence can be expected to reduce backfill porosity to values of the order of 1% and corresponding permeabilities of 10^{-19} – 10^{-17} m^2 (Section 3.3). This is done in a preliminary manner by assuming a variety of

simplified stress evolution paths within the backfill, i.e. a set of simplified cases. Note once again that a more rigorous treatment requires numerical computation of the coupled convergence-compaction problem.

Case 1: Backfill compaction under fixed lithostatic stress (fast compaction case):

A lower bound estimate of the time for backfill to compact to a porosity of 1% can be obtained by assuming that the backfill is subjected to the lithostatic stress from the onset of convergence by assuming power law creep (Eq. 5.3) and humidity-assisted or pressure solution creep (Eq. 5.5). The latter one is grain size sensitive, and the volumetric strain rates have been calculated by generating three log normal distributions resembling the different fractions of the KOMPASS mixture (see Section 3.1 and Figure 3-1) with 10000 grains in each fraction, following a similar approach as Ter Heege et al. 2004. Each grain then has a size and a (volume) probability. Hence, its contribution to the strain rate can then be calculated by calculating the strain rate of that grain, multiplied by its probability, given as:

$$\dot{\epsilon}_i P_i = \left[A_{hum} \exp\left(\frac{-Q_{ps}}{RT}\right) \frac{\bar{\sigma}}{T d_i^3} f_2(\phi) \right] P_i \quad \text{Eq. 5.7}$$

in which $\dot{\epsilon}_i$ is the strain rate of each grain, P_i is the (volume) probability of that grain and d_i is the size of each grain. Subsequently for each of the three log-normal distributions, the total strain rate can be calculated by adding all the strain rates for each of the 10000 grains within that fraction, multiplied by its probability, divided by the summed probability of that fraction, so that for each of the three log-normal distribution:

$$\dot{\epsilon}_k = \frac{\dot{\epsilon}_1 P_1 + \dot{\epsilon}_2 P_2 + \dots + \dot{\epsilon}_j P_j}{P_1 + P_2 + \dots + P_j} = \frac{\sum_{i=1}^{i=j} \dot{\epsilon}_i P_i}{\sum_{i=1}^{i=j} P_i} \quad \text{Eq. 5.8}$$

in which $\dot{\epsilon}_k$ is the strain rate of each of the three log-normal distribution ($k = 1,2,3$), $\sum P_i$ is the total probability of all grains belonging to that log-normal distribution and $j = 10000$. Finally, the total strain rate is given by the adding the strain rates of the three-fraction multiplied by their volume fractions (v_k - see Figure 3-1), such that:

$$\dot{\epsilon}_{tot} = \dot{\epsilon}_k v_k \quad \text{Eq. 5.9}$$

The porosity reduction resulting from the BGR power law creep (Eq. 5.3) and humidity-assisted or pressure solution creep (Eq. 5.5) of backfill for a distributed grain size of the KOMPASS reference mixture, at a constant mean effective stress of 15 MPa (e.g. equivalent to the lithostatic pressure at ~700m), taking a starting porosity of 40% at the onset of Stage II, is given in Figure 4-1a. When the pores are saturated with brine, a porosity of 1% is reached after 281 days of the start of stage II. For the relative humidities (60-75% RH) expected in backfill (e.g. containing 0.5-1 wt% of water) under geological

disposal conditions, a porosity of 1% is reached after $9.51 \cdot 10^4 - 1.09 \cdot 10^3 - 4.82 \cdot 10^3$ days (3.0 – 13.2 years). Figure 4-1c shows the porosity reduction resulting from purely humidity-assisted or pressure solution creep (Eq. 5.5) of backfill with the same grain size distribution at the same constant mean effective stress of 15 MPa. When only humidity creep is considered, the timescales required to reach a porosity of 1% is reached after 301 days (if saturated with brine). For the relative humidities (60-75% RH) expected in backfill (e.g. containing 0.5-1 wt% of water) under geological disposal conditions, a porosity of 1% is reached after $2.94 \cdot 10^3 - 2.94 \cdot 10^4$ days (8.1 – 81 years).

These calculations indicate that at these stresses it is expected that pressure solution or humidity-assisted creep is the dominant mechanism, although the effect of power law creep becomes more important when lower humidities are considered. The reason for this is that the porosity function of the BGR power law (Eq. 5.4) is less sensitive to lower porosities. Hence, power law creep becomes dominant over humidity-assisted creep at 1-5% porosity (depending on humidity). Experiments at low porosities are required to determine whether such a switch to power law creep is reasonable or that it is an artifact of the way the porosity function (Eq. 5.4) has been obtained, i.e. at higher porosities (Hein 1991) and extrapolation to lower porosities has resulted in strain rates that are too high for these conditions. Hence, it might be better to assume that humidity-assisted creep becomes dominant at low porosities and the BGR-power law term has to be switched of below 5% porosity. We emphasise that these timescales represent extreme lower bound estimates because under true conditions of coupled convergence-compaction the effective mean stress in the backfill only approached lithostatic values in the very last stages of Stage II convergence.

Case 2: Backfill compaction under linearly increasing mean effective stress:

When a coupled convergence model is considered, the gallery must converge and the porosity of the backfill first needs to decrease in order for the effective mean stress in the backfill to build up (Figure 2-1). In the absence of a numerical calculation based on the creep equations recommended here (Eq 5.1 – 5.6), we use previous calculations based on empirical salt flow and backfill compaction laws (Kröhn et al. 2015) to provide a first, order-of-magnitude indication of the rate of build-up of mean effective stress to be expected in a backfilled opening under in-situ repository conditions. Specifically, we use the stress evolution computed by Krohn et al. 2017 shown in Figure 2-1. Assuming a linear increase of mean stress at a rate of 6 MPa/100 year at the centre of the backfilled opening (based on the results of the coupled convergence model shown in this figure for “dry” conditions) application of our recommended compaction law (Equations 5.3 and 5.5), accounting for the distributed grain size of the KOMPASS mixture, predicts:

- a) it takes approximately $8.24 \cdot 10^3$ days (23 years) after the start of Stage II for the backfill to reach a porosity of 1% under brine-saturated conditions for BGR power law creep and pressure solution creep (Figure 4-1b);
- b) for relative humidities of 60-75% corresponding to brine contents in the backfill of 0.5-1.0 wt%, it will require $3.26 \cdot 10^4 - 6.95 \cdot 10^4$ days (89– 190 years) to reach the same porosity, assuming a combination of BGR power law creep and humidity-assisted creep (Figure 4-1b);
- c) it takes approximately $8.31 \cdot 10^3$ days (23 years) after the start of Stage II for the backfill to reach a porosity of 1% under brine-saturated conditions for pressure solution creep only (Figure 4-1d); and
- d) for relative humidities of 60-75% corresponding to brine contents in the backfill of 0.5-1.0 wt%, it will require $3.39 \cdot 10^4 - 7.05 \cdot 10^5$ days (93 – 287 years) to reach the same porosity for humidity-assisted creep only (Figure 4-1d).

Assuming that it takes initial convergence for the backfill resistance to increase and the mean effective stress to build up, this results in an increase of timescales required to reach 1% porosity from 280 days to 23 years under saturated conditions and from 3-81 to 89-287 years under humid conditions. Note again that this is just an example of the order of magnitude of timescales expected when a coupled model is used. In a rigorous numerical calculation of the coupled problem, the repository geometry, conditions (e.g. T, depth, dimensions) and decision on constitutive laws for the backfill and surrounding wall rock will determine the evolution of effective stress in the backfill, the timescale to reach 1% porosity and the end of Stage II (end of significant convergence and compaction creep).

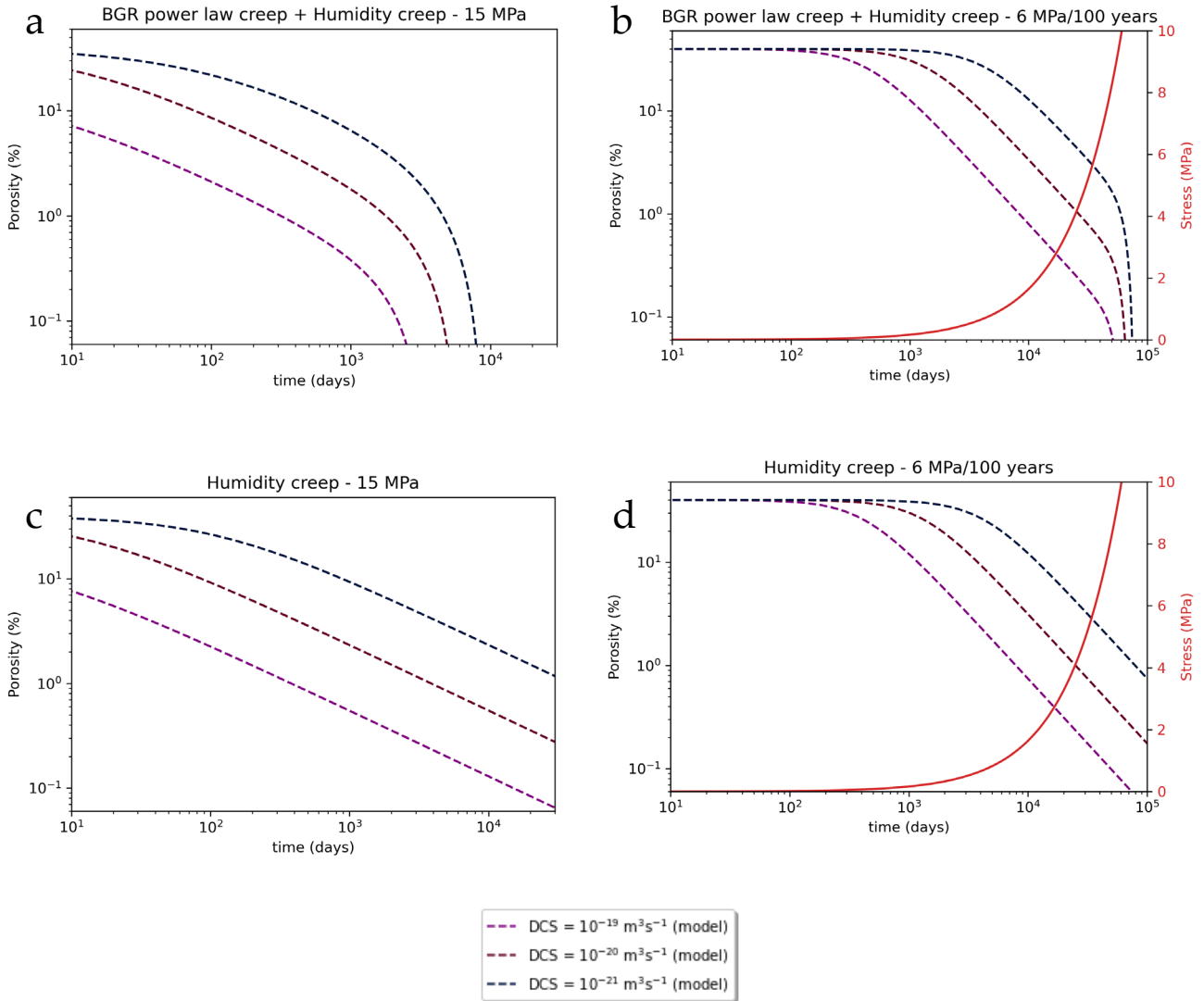


Figure 4-1: (a) Porosity reduction for BGR power law creep (Eq. 5.3) and humidity-assisted or pressure solution creep (Eq. 5.5) in KOMPASS-type backfill at a constant mean effective stress equal to a lithostatic pressure of 15 MPa expected at $\sim 700\text{m}$ depth (Case 1). (b) Porosity reduction for compaction creep of KOMPASS backfill by the same mechanisms at a mean effective stress that increases linearly at a rate of 6 MPa/100 years (Case 2). Initial porosity in both cases is 40%. (c) and (d) same conditions and properties as in a and b, but now showing only humidity creep (Eq 5.5). $DCS = 10^{-19} \text{ m}^3 \text{ s}^{-1}$ corresponds to brine-saturated conditions, while $DCS = 10^{-21} - 10^{-20} \text{ m}^3 \text{ s}^{-1}$ corresponds to in-situ humidity conditions (RH of 60-75%) relevant for geological disposal.

In Cases 1 and 2 above, it has been assumed that backfill compaction to 1% occurs without any build-up of pore pressure and hence without any reduction of effective mean stress driving backfill compaction. In practice, such effects may decrease compaction rate and modestly increase the time needed to reach 1% porosity beyond those times estimated here. More importantly, preliminary calculations for Cases 1 and 2 indicate that for a log normal grain size distribution with a mean grain size of 1.9 mm (e.g. only the larger

fraction of the KOMPASS mixture), compaction creep rates are 2-3 orders of magnitude slower. Hence, timescales for porosity reduction to 1% will also increase by 2-3 orders of magnitude in Cases 1 (constant mean effective stress of 15 MPa) and 2 (linearly increasing mean effective stress), i.e. reaching the range of 3000-50.000 years. This is because of the inverse cubic dependence of the pressure solution or humidity-assisted creep mechanism on grain size (see equation 5.5). On this basis, we recommend sieving and/or crushing of the backfill used in repository construction to the smallest needed to allow full Stage II convergence within feasible waste canister lifetime. We also recommend a water content of 0.5 wt% to maximise humidity-assisted compaction rates without leading to a residual porosity above 1.0 vol %.

4.2.2 Recommendations for porosity-permeability evolution in Stage II

The permeability relation given by Zhang et al. 2007 for three different porosity regimes in granular salt with grain size 0.1-0.5 mm are recommended for the porosity-permeability relation in Stage II. These relations are shown in Figure 3-3 and can be described using Equation 10 ($\kappa = 1.13 \cdot 10^{-11} \phi^{2.80}$), when $\phi \geq 10\%$, Equation 11 ($\kappa = 6.54 \cdot 10^{-8} \phi^{6.99}$), when $4\% > \phi \geq 10\%$ and Equation 12 ($\kappa = 3.90 \cdot 10^{-16} \phi^{1.40}$) when $\phi \leq 4\%$. Bechthold et al. 1999 measured permeabilities around one order of magnitude higher in their coarser-grained salt backfill samples (< 8 mm) but noticed the same trends and regimes. The recommended porosity-permeability relations are given in Table 4-2.

Table 4-2: Recommended porosity-permeability relations for crushed salt backfill determined from compaction tests on fine granular salt (0.1-0.5 mm, Zhang et al 2007). Values of permeability can be around 1 order higher in coarse backfill (grain size <8mm, Bechtholt et al 1999).

| Stages | Porosity | Permeability | |
|-----------|----------------------|-----------------------------------|--|
| Stage I | 40% | $\kappa \gg 10^{-11} \text{ m}^2$ | |
| | | $\phi \geq 10\%$ | $\kappa = 1.13 \cdot 10^{-11} \phi^{2.8}$ |
| Stage II | 40-1% ^(a) | $4\% > \phi \geq 10\%$ | $\kappa = 6.54 \cdot 10^{-8} \phi^{6.99}$ |
| | | $\phi \leq 4\%$ | $\kappa = 3.90 \cdot 10^{-16} \phi^{1.40}$ |
| Stage III | 1%-0.1% | n/a | |

^(a) the exact porosity at which healing will dominate has to be determined

4.2.3 Recommendations for static backfill evolution (Stage III)

As indicated in preceding sections, these data suggest that the permeability reached in the backfill upon reaching 1% porosity at/near the end of Stage II convergence will be of the order $10^{-19} - 10^{-17} m^2$. Depending on the different assumptions made on stress evolution, it has been shown above that the porosity of a KOMPASS-like backfill material is likely to decrease to ~1% within 300 years of Stage II convergence, provided similar percentages of moisture are present and that the backfill contains significant amount of small (0.1mm) grains (as the KOMPASS reference mixture does) (see Figure 4-1).

Considering, the porosity function of the BGR power law (Eq. 5. 4) is too optimistic (see Figure 4-1a and b), it will take at least another 300-1000 years for the porosity to reduce from 1% to 0.1% (for a backfill with KOMPASS mixture grain size distribution - see Figure 4-1c and d), and potentially even much longer considering the uncertainties in extrapolation of the recommended compaction law to low porosities and the fact that the effective mean stress in the backfill may approach zero at porosities around 1%). Once a porosity around 1% is reached, the permeability will have been reduced by compaction creep down to $10^{-17} m^2$ to $10^{-19} m^2$ (see data by Bechthold et al. 1999; Zhang et al. 2007 - Figure 3-4). However, this permeability is still 3-4 orders of magnitude higher than the porosity of natural rock salt. From this point, i.e. into Stage III of backfill evolution, further reduction in permeability is likely to be dominated by pore shrinkage and disconnection, caused by diffusive mass transfer (dissolution-precipitation) mechanisms driven by interfacial area/energy reduction (see Section 2.4).

Houben et al. 2013 shows that crack healing, i.e. contraction and disconnection, in salt by these mechanisms can be estimated to occur on timescales of a few years at laboratory humidity levels. Extrapolating these results to intermediate backfill humidity conditions, such as the ones considered here (using the moisture film diffusivity versus RH data of Koelemeijer et al. 2012), points to timescales of the order of decades for cracks to heal sufficiently to reduce permeability significantly. If crack healing can occur in periods of decades, it seems likely that the porosity-permeability reduction during healing of backfill by pore contraction and disconnection, in the approach to textural equilibrium (equilibrium dihedral angles), will occur at a more rapid rate than reduction by compaction at the low strain rates expected in Stage III (i.e. at porosities < 1%).

First estimates of the timescale for pore contraction and disconnection in compacted, brine-saturated salt backfill have been made in an unpublished preliminary study by Zhang, Grupa and co-workers (Zhang et al. 2008). In this study, the individual healing of cracks is combined with the percolation model described by Peach & Spiers 1996, to investigate the reduction in pore connectivity and hence permeability in an aggregate as

opposed to healing of single cracks. Their results point to longer timescales of 456-1084 years for a model with tapered cracks to seal and 7990-26300 years for parallel-sided cracks to seal under brine saturated conditions with a starting porosity of 3%. However, when the starting porosity is assumed to be 0.3%, the healing times reduce to 5-230 years, also assuming brine-filled conditions. For humid conditions, the minimum sealing times which they predict are 9000 years. It must be noted that these calculations are done for dilated rock salt with an initial permeability of 10^{-12} and 10^{-14} m^2 at respectively 3 and 0.3% porosity, whereas the initial permeability of mechanically compacted backfill at those porosities is expected to be in the range of $10^{-15} - 10^{-19} \text{ m}^2$ (e.g. Bechthold et al. 1999; Zhang et al. 2007). In their model the sealing has an inverse cubic dependence on grain size, which for their calculations was set as 10 mm. However, the grain sizes in the backfill (assuming KOMPASS mixture) are expected to be about 1 order of magnitude smaller, which reduces the sealing times for humid conditions to 9 years.

The central aim of the present UU-COVRA project is to quantify this crucial timescale for Stage III permeability reduction towards natural salt rock levels, in a rigorous manner, using both theoretical and experimental approaches. Besides theoretical work, long-term permeability measurements on pre-compacted samples with porosities around 1% and lower are going to be necessary to evaluate the decrease in permeability due to static healing during Stage III and to test the theoretical models developed. Although 1% has been chosen here as the porosity at which compaction creep in Stage II slows down and Stage III evolution begins, this does not rule out the possibility that permeability reduction by healing mechanisms may already dominate permeability reduction, and bring about the Stage II to III transition, at higher porosities.

4.3 An analytical approach to coupled convergence: Towards a fast model for estimating Stage II convergence times?

It will be evident from the foregoing Sections (Section 4.1-4.2) that the present estimates for the duration of Stage II convergence of a backfilled opening (i.e. to the point where convergence is expected to cease at around 1% backfill porosity and where Stage III begins) are crude and subject to multiple uncertainties. It will also be clear that accurate estimates of the type needed for the COVRA safety study can only be obtained by properly solving the problem of coupled convergence and backfill compaction, e.g. by finite element modelling (FEM) incorporating constitutive laws for both the salt host rock and the backfill material within a gallery, shaft or borehole.

This has been done in numerous previous studies (e.g. Krohn et al. 2017; Prij 1991) but with the use of empirical constitutive equations for backfill that differ drastically from the preliminary, microphysically based ones recommended here - and from those expected to emerge from our ongoing work in the UU-COVRA project. Setting up an FEM model to solve the coupled convergence problem using UU compaction laws is a major undertaking that is not feasible in the UU-COVRA project (though it may be feasible for KOMPASS partners to insert UU constitutive laws into their FEM models in future). An alternative possibility is to employ an analytical solution for the coupled convergence-compaction problem focusing on an idealized backfilled opening, such as a circular-sectioned gallery or borehole surrounded by a large cylindrical region of host salt rock. Such solutions were explored extensively in the 1980's and 1990's by Prij and others (see Prij 1991, for example) but have since been superseded by advances in FEM techniques. In the following section, the foundations of the analytical approach are laid out as a basis for constructing a fast computational model for estimating the duration (timescale) of Stage II convergence, i.e. convergence to the point at which compaction-related porosity-permeability reduction becomes negligibly slow and static Stage III healing sets in. As already discussed in detail, this is expected to occur at around 1% or perhaps 0.1% porosity in the backfill, corresponding to a permeability of $10^{-19} - 10^{-17} \text{ m}^2$.

4.3.1 Elements of an analytical solution for Stage II convergence

Analytical solutions for steady state, plane strain convergence of a cylindrical opening, surrounded by a much larger cylindrical region of elastic solid that exhibits steady state creep described by a flow law of the form $\dot{\epsilon} = A\sigma^n$, have long been available in the literature on the mechanics of thick-walled cylinders (e.g. Besseling 1968; Timoshenko 1956). The problem can be considered as equivalent to the creep of an internally pressurized pressure vessel where the applied pressure acting on the walls of the bore is negative (tensile) – as opposed to convergence of an unpressurized bore due to the action of an equal but positive hydrostatic pressure applied to the outer boundary of the thick cylinder.

Prij (1991) applied this analysis to obtain an analytical approximation for convergence creep of an open vertical borehole or shaft in a salt formation (Figure 4-2), taking the far field stress (i.e at a conceptual thick cylindrical wall) to be equal to the isotropic lithostatic pressure (P) in the salt at the depth of interest. The expression obtained for the steady state convergence rate of a length of borehole having volume V can be written in terms of a volumetric strain rate for the cavity given by:

$$\dot{\epsilon}_{conv} = \frac{-\dot{V}}{V} = \frac{\sqrt{3}^{\frac{n+1}{n}}}{n} AP^n = \alpha AP^n \quad (\text{Eq. 5.10})$$

Where P is the lithostatic pressure (MPa), $\alpha = \sqrt{3}^{n+1}/n^n$. This applies independently of opening radius. The same expression can be assumed to hold roughly for a horizontal cylindrical cavity, such as a gallery (see Figure 4-2), provided that the cavity radius a is small compared to the depth of the cavity (such that the difference in lithostatic pressure P between the top and bottom of the cavity is minimal). If a borehole or gallery contains backfill that supports an isotropic mean stress $\bar{\sigma}$ (MPa) and assuming no pore pressure builds up during stage II convergence, then the driving stress for convergence becomes $P - \bar{\sigma}$. The coupled steady-state convergence rate can subsequently be written as:

$$\dot{\epsilon}_{conv} = \alpha A (P - \bar{\sigma})^n \quad (\text{Eq. 5.11})$$

Steady state convergence of an open cavity at the rate described by Eq. 5.10 or Eq. 5.11, when $\bar{\sigma} = 0$, will not be established immediately upon creating the opening, because of a phase of transient evolution in the stress-strain field around the opening from an initial purely elastic field towards the ultimate steady condition (Besseling 1968). The rates during this phase are much faster than the steady state rates. However, in-situ measurements in salt mines and analytical calculations (Prij 1991) indicate that this stage takes in the order of a few months to a year for an open cavity under repository conditions.

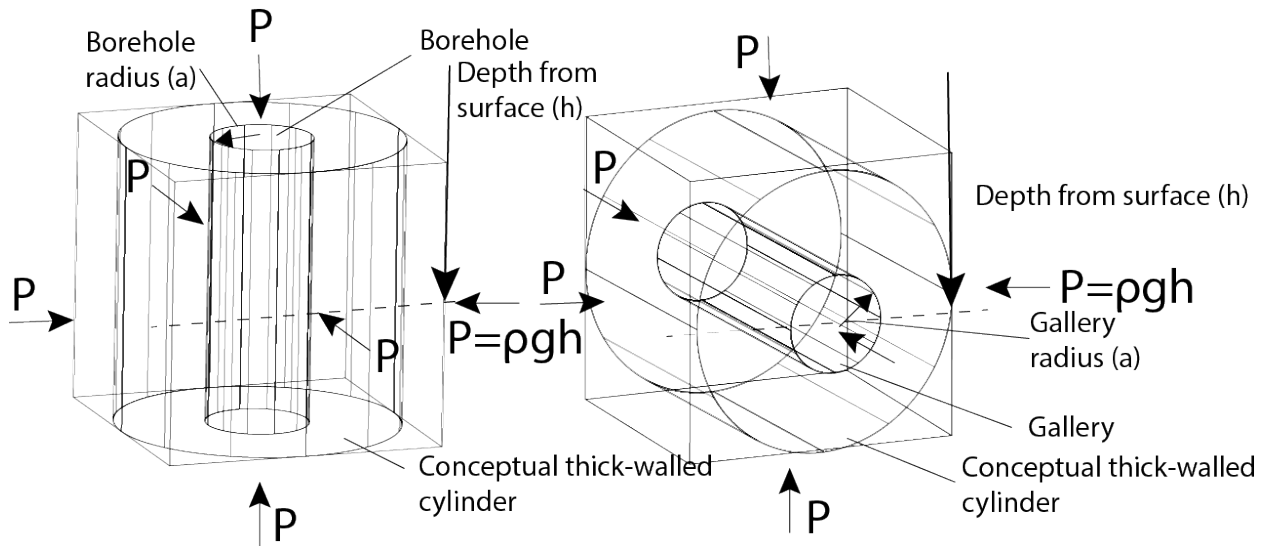


Figure 4-2: Schematic illustration of (left) a borehole and (right) a gallery located at a given depth in a salt formation, along with the extent of a surrounding conceptual thick-walled cylinder of host salt rock.

On this basis, and as a first approximation, we assume that the initial transient phase of convergence of a repository cavity will mostly occur after its construction and before emplacement of the backfill. After backfill emplacement, and from the moment at which it starts to resist convergence (that is from the onset of stage II, when $\bar{\sigma} > 0$), we assume that steady state convergence is achieved – i.e. in an evolving series of steady state rates

(depending on porosity). Convergence rates and closure times obtained in this way will accordingly represent lower and upper bounds.

Once stage II convergence begins, the convergence rates must equal the compaction strain rate in the backfill, such that $\dot{\epsilon}_{conv} = \dot{\epsilon}_{comp}$. For a single creep mechanism in the salt host rock, described by $\dot{\epsilon} = A\sigma^n$, and a single compaction creep mechanism in the backfill, described by $\dot{\epsilon} = B\bar{\sigma}^m f(\phi)$ (see Table 4-1, for example), combined with Eq. 5.11 will yield:

$$\alpha A(P - \bar{\sigma})^n = B\bar{\sigma}^m f(\phi) \quad \text{Eq. 5.12}$$

where $f(\phi)$ represents the effect of decreasing backfill porosity on backfill compaction rate or resistance. For a gallery or borehole segment at a known depth, the lithostatic pressure is fixed. Moreover, given well-defined constitutive laws for the salt rock and backfill, the parameters A, n, B and m are known and fixed (at constant temperature and grain size). Equation 5.12 can then be written as:

$$\alpha A(P - \bar{\sigma})^n - B\bar{\sigma}^m f(\phi) = 0 \quad \text{Eq. 5.13}$$

Which can be solved numerically to obtain $\bar{\sigma}$ as a function of ϕ , varying ϕ from its initial value ϕ_0 at the start of stage II to $\phi_f = 1\%$ at the end of stage II (and start of stage III). Equation 5.12 then yields the compaction strain rate at any porosity, neglecting small elastic changes in solid phase density with changing $\bar{\sigma}$ in the backfill, the relation $\dot{\phi} = -\dot{\epsilon}_{comp} \cdot (1 - \phi)$ applies, so that $\dot{\phi}$ at any porosity is given by:

$$\dot{\phi} = -(1 - \phi)B\bar{\sigma}^m f(\phi) \quad \text{Eq. 5.14}$$

Numerical integration of $d\phi = \dot{\phi}dt$ over the interval ϕ_0 to ϕ_f , using appropriate time steps then yields ϕ vs time and hence the duration of steady state stage II convergence to 1% porosity.

For the case of two creep mechanisms in both the host salt rock and the backfill the above approach can be modified. Assuming that the steady state strain rate fields in the salt rock around an opening are additive for the two mechanisms considered than Eq. 5.11 can be written as:

$$\dot{\epsilon}_{conv} = \alpha A_1(P - \bar{\sigma})^{n_1} + \alpha A_2(P - \bar{\sigma})^{n_2} \quad \text{Eq. 5.15}$$

Where A_i and n_i ($i = 1,2$) are the material parameters and stress exponents of the two creep equations for the host rock (Eq. 5.1 and Eq. 5.2). Similarly, the compaction creep rate in the backfill will be given as:

$$\dot{\epsilon}_{comp} = B_1\bar{\sigma}^{m_1}f_1(\phi) + B_2\bar{\sigma}^{m_2}f_2(\phi) \quad \text{Eq. 5.16}$$

where B_i and m_i ($i = 1,2$) are the material parameters and stress exponents of the two compaction creep equations for the backfill (Eq. 5.3 and Eq. 5.5). Given that $\dot{\epsilon}_{conv} = \dot{\epsilon}_{comp}$ it can be shown that for two creep mechanisms in both the surrounding host rock and backfill, this leads to:

$$\alpha A_1(P - \bar{\sigma})^{n_1} + \alpha A_2(P - \bar{\sigma})^{n_2} - B_1\bar{\sigma}^{m_1}f_1(\phi) + B_2\bar{\sigma}^{m_2}f_2(\phi) = 0 \quad \text{Eq. 5.17}$$

Provided the parameters in the creep equations are known, this can be solved numerically to obtain $\bar{\sigma}$ as a function of ϕ for any value of lithostatic pressure P , ϕ in the range of $\phi_f \leq \phi \leq \phi_0$. Equation 5.16 then gives the backfill compaction rate $\dot{\epsilon}_{comp}$ at any porosity, and using $\dot{\phi} = -\dot{\epsilon}_{comp} \cdot (1 - \phi)$, the rate of change of porosity at any instant in stage II is given as:

$$\dot{\phi} = -(1 - \phi)B_1\bar{\sigma}^{m_1}f_1(\phi) + B_2\bar{\sigma}^{m_2}f_2(\phi) \quad \text{Eq. 5.18}$$

As in the single mechanism case, numerical integration of $d\phi = \dot{\phi}dt$ over the interval ϕ_0 to ϕ_f , then gives ϕ vs time and the duration of convergence in stage II, assuming a series of steady states. Using the recommended two-mechanism creep equations for salt rock and salt backfill given in Table 4-1 in Equation 5.18, provides a means of estimating the duration of stage II coupled convergence down to 1% porosity. This also allows for the effects of P, T and backfill grain size (-distribution) on convergence rates and timescales.

4.3.2 Next steps to obtain improved Stage II convergence times

Taken together, Equations 5.17 and 5.18 above form an analytical model that can be solved numerically to yield the evolution of porosity during steady-state, Stage II convergence of a backfilled opening. This offers a way to provide better estimates of the timescale to reach porosities of the order of 1% (at which Stage III is anticipated to begin) than presented in this report (Section 4.2.1). In the coming months, the UU team will implement the numerical solution to the model making use of the recommended constitutive equations given in Table 4-1, or of updates that emerge as new experimental data are obtained. The resulting “fast model” (as opposed to an FEM calculation) will be used to investigate, in particular, how backfill grain size (distribution) and water content or humidity influence Stage II convergence times and the evolution of backfill permeability and transport potential throughout Stage II (i.e. until convergence reaches negligible rates and Stage III static healing starts to dominate permeability change). Results will be compared with FEM results on convergence obtained by others (e.g. KOMPASS partners), ideally using UU-recommended constitutive laws, to assess whether the steady state analytical solution is adequate or whether transient convergence needs to be accounted for (e.g. following the analytical approach by Besseling 1968).

5 Conclusion/Summary

In this report we have reviewed current understanding of the creep deformation mechanisms and processes that operate in salt rock and granular salt backfill materials under conditions relevant to the convergence of openings in radioactive waste repositories in salt formations. We have also reviewed available empirical and microphysically based constitutive models and the experimental data on which these models are based or against which they tuned.

On this basis, preliminary recommendations are made regarding choice of constitutive models for creep of salt, and in particular compaction creep of salt backfill, for the purpose of estimating porosity evolution in and closure times of backfilled openings down to porosities of the order of 1%. Recommendations are also made for the relationship between porosity and perm down to porosities of 0.1 to 1 %. Attempts are then made to estimate closure times crudely and to consider subsequent static healing behaviour. Finally, an analytical model is outlined to allow better estimates of porosity-permeability evolution and the timescale for convergence of a backfilled opening towards a residual porosity of 1% and a corresponding permeability of $10^{-19} - 10^{-17} m^2$. The key findings and conclusions can be summarized as follows:

- 1) Three stages of convergence of a repository opening (borehole, shaft or gallery) can be distinguished:
 - a. Stage I: unsupported convergent creep and microcracking in the EDZ surrounding the disposal galleries, prior to contact with the backfill;
 - b. Stage II: backfill-supported convergent creep coupled with backfill compaction and porosity permeability reduction in the backfill and EDZ; and
 - c. Stage III: near-static pore disconnection and healing/sealing as hydrostatic stress is approached and as creep closure and backfill compaction rates become negligible.
- 2) Porosity and permeability reduction in Stage II is controlled by coupled convergence-compaction. Computation of this and hence of the duration of Stage II (time until the onset of static healing in Stage III) requires an FEM or analytical solution employing constitutive equations for salt creep and backfill compaction creep.
- 3) Key constitutive equations for coupled compaction are given in Table 4-1, based on experimental results. These describe creep in the intact dense salt around the repository and compaction creep in the backfilled repository. For the intact salt around the repository, the mechanical behaviour is best described using a two-mechanism flow law of dislocation creep and pressure solution creep. Compaction creep in the backfill is best described using a power law with a stress-exponent of $n = 5$ and a modified version of the pressure solution model, taking the diffusive properties of adsorbed films in a humid environment into account. Both creep mechanisms in the backfill have an empirical based porosity function, describing the decrease in strain rates with decreasing porosity. We recommend to use these

equations in combination with the porosity-permeability relations (Table 4-2) as input for modelling the coupled convergence problem in Stage II.

- 4) Crude estimates of the Stage II convergence behaviour of a backfilled opening in a repository, based on the equations given in Table 4-1, for a constant lithostatic stress of 15 *MPa* and a linearly increasing stress of 6 *MPa/100 years* point to timescales of 3 to 287 *years* for porosities to reach values around 1% and permeability of $\sim 10^{-17} \text{ m}^2$ for a mixture containing fine grained material (e.g. KOMPASS mixture).
- 5) To enable better estimates of Stage II convergence times and porosity-permeability evolution in future, an analytical model has been outlined, following previous work by Prij 1991 and others, for coupled convergence. This will be implemented and evaluated/improved in future and used as a fast model to explore the effects of grain size and humidity on convergence times in Stage II.
- 6) Beyond this, permeability is expected to decrease primarily by pore reconfiguration and disconnection caused by static healing in Stage III. Previous work suggests this may take 5 to 9000 *years* (counting from the end of stage II, i.e. after a porosity of 1% is reached), but these estimates are highly uncertain. The present project aims to elucidate this, by further exploring the reduction in permeability by healing, by means of permeametry, CT-imaging and microphysical modelling.

References

- Barber, D.J. & Meredith, P.G. (1990): *Deformation Processes in Minerals, Ceramics and Rocks*, Deformation Processes in Minerals, Ceramics and Rocks.
- Bauer, S.J., Broome, S.T., Hansen, F.D., Lampe, B., Mills, M. & Stormont, J. (2015): Gas flow measurements of consolidating crushed salt. *49th US Rock Mech. / Geomech. Symp. 2015 3*, pp. 1800–1805.
- Bechthold, W., Rothfuchs, T., Poley, A., Ghoreychi, M., Heusermann, S., Gens, A. & Olivella, S. (1999): Backfilling and Sealing of Underground Repositories for Radioactive Waste in Salt (BAMBUS Project). *Eur 19124 En* pp. 248.
- Besseling, J.F. (1968): *A Thermodynamic Approach to Rheology*. TU Delft.
- Callahan, G.D. & Hansen, F.D. (1999): Crushed-salt constitutive model. *Basic Appl. Salt Mech. 1999 (February)*, pp. 239–252.
- Carter, N.L., Hansen, F.D. & Senseny, P.E. (1982): Stress magnitudes in natural rock salt.. *J. Geophys. Res. 87 (B11)*, pp. 9289–9300.
- Carter, N.L. & Heard, H.C. (1970): Temperature and rate dependent deformation of halite. *Am. J. Sci.*
- Carter, N.L., Horseman, S.T., Russell, J.E. & Handin, J. (1993): Rheology of rocksalt. *J. Struct. Geol. 15 (9–10)*, pp. 1257–1271.
- Chan, K.S., Bodner, S.R. & Munson, D.E. (2001): of Damage Mechanics Permeability of WIPP Salt during 10.
- Chen, J., Ren, S., Yang, C., Jiang, D. & Li, L. (2013): Self-healing characteristics of damaged rock salt under different healing conditions. *Materials (Basel). 6 (8)*, pp. 3438–3450.
- Czaikowski, O., Friedenber, L. & Wiczorek, K. (2020): *Kompass. compaction of crushed salt for the safe containment (No. GRS-608)*.
- De Bresser, J.H.P. (2002): On the mechanism of dislocation creep of calcite at high temperature: Inferences from experimentally measured pressure sensitivity and strain rate sensitivity of flow stress. *J. Geophys. Res. Solid Earth 107*.
- De Mulder, E.F., Geluk, M.C., Ristema, I., Westerhoff, W.E. & Wong, T.E. (2003): *De ondergrond van Nederland*.
- Friedenberg, L., Bartol, J., Bean, J., Czaikowski, O., Düsterloh, U., Gartzke, A.-K., Hangx, S., Laurich, B., Lerch, C., Lerche, S., Lippmann-Pipke, J., Liu, W., Lüdeling, C., Mills, M., Popp, T., Rabbel, O., Rahmig, M., Reedlunn, B., Rölke, C., Spiers, C.J., Svensson, K., Thiedau, J., van Oosterhout, B., Zemke, K. & Zhao, J. (2022): Compaction of

- Crushed Salt for the Safe Containment – Overview of the Phase 2 of the KOMPASS project. In: *SaltMech X*.
- Guillope, M. & Poirier, J.P. (1979): Dynamic recrystallization during creep of single-crystalline halite: an experimental study.. *J. Geophys. Res.* 84 (B10), pp. 5557–5567.
- Hart, J., Prij, J., Vis, G.-J., Becker, D.-A., Wolf, J., Noseck, U. & Buhmann, D. (2015): Collection and analysis of current knowledge on salt- based repositories.
- Hart, J., Wildenborg, T., Davis, P., Becker, D.-A. & Verhoef, E. (2013): Definition of the OPERA safety case for radioactive waste disposal in the Netherlands pp. 299–310.
- Haupt, M. (1991): A constitutive law for rock salt based on creep and relaxation tests. *Rock Mech. Rock Eng.* 24 (4), pp. 179–206.
- Hein, H.J. (1991): *Ein Stoffgesetz zur Beschreibung des thermomechanischen Verhaltens von Salzgranulat*. RWTH Aachen.
- Holcomb, D.J. & Hannum, D.W. (1982): *Holcomb, David Joseph, and D. W. Hannum. Consolidation of crushed-salt backfill under conditions appropriate to the WIPP facility*.
- Holcomb, D.J. & Zeuch, D.H. (1990): Modeling the consolidation of a porous aggregate of dry salt as isostatic hot pressing. *J. Geophys. Res.* 95 (B10).
- Holness, M.B. & Lewis, S. (1997): The structure of the halite-brine interface inferred from pressure and temperature variations of equilibrium dihedral angles in the halite-H₂O-CO₂ system. *Geochim. Cosmochim. Acta* 61 (4), pp. 795–804.
- Hou, Z., Wundram, L., Meyer, R., Schmidt, M., Schmitz, S. & Were, P. (2012): Development of a long-term wellbore sealing concept based on numerical simulations and in situ-testing in the Altmark natural gas field. *Environ. Earth Sci.* 67 (2), pp. 395–409.
- Houben, M.E., Desbois, G. & Urai, J.L. (2013a): Pore morphology and distribution in the Shaly facies of Opalinus Clay (Mont Terri, Switzerland): Insights from representative 2D BIB-SEM investigations on mm to nm scale. *Appl. Clay Sci.* 71, pp. 82–97.
- Houben, M.E., ten Hove, A., Peach, C.J. & Spiers, C.J. (2013b): Crack healing in rocksalt via diffusion in adsorbed aqueous films: Microphysical modelling versus experiments. *Phys. Chem. Earth* 64, pp. 95–104.
- Hunsche, U. & Hampel, A. (1999): Rock salt - The mechanical properties of the host rock material for a radioactive waste repository. *Eng. Geol.* 59 (3–4), pp. 271–291.
- Khaledi, K., Mahmoudi, E., Datcheva, M., König, D. & Schanz, T. (2016): Sensitivity analysis and parameter identification of a time dependent constitutive model for rock salt. *J. Comput. Appl. Math.* 293, pp. 128–138.

- Koelemeijer, P.J., Peach, C.J. & Spiers, C.J. (2012a): Surface diffusivity of cleaved NaCl crystals as a function of humidity: Impedance spectroscopy measurements and implications for crack healing in rock salt. *J. Geophys. Res. Solid Earth* 117 (1), pp. 1–15.
- Koelemeijer, P.J., Peach, C.J. & Spiers, C.J. (2012b): Surface diffusivity of cleaved NaCl crystals as a function of humidity: Impedance spectroscopy measurements and implications for crack healing in rock salt. *J. Geophys. Res. Solid Earth* 117 (1), pp. 1–15.
- Korthaus, E. (1996): Measurement of crushed salt consolidation under hydrostatic and deviatoric stress conditions. *Ser. rock soil Mech.* pp. 311–322.
- Kröhn, K.-P., Stührenberg, D., Herklotz, M., Heemann, U., Lerch, C. & Xie, M. (2009): *Restporosität und-permeabilität von kompaktierendem Salzgrus-Versatz REPOPERM-Phase 1.*
- Krohn, K.-P., Stührenberg, D., Jobmann, M., Heeman, U., Czaikowski, O., Wieczorek, K., Muller, C., Zhang, C.-L., Moog, H., Schirmer, S. & Friedenbergl, L. (2017): *Mechanical and hydraulic behaviour of compacting crushed salt backfill at low porosities.*
- Kröhn, K.P., Zhang, C.L., Czaikowski, O., Stührenberg, D. & Heemann, U. (2015): The compaction behaviour of salt backfill as a THM-process. *Mech. Behav. Salt VIII - Proc. Conf. Mech. Behav. Salt, SALTMECH VIII (May 2015)*, pp. 49–60.
- Langer, M. (1999): Principles of geomechanical safety assessment for radioactive waste disposal in salt structures. *Eng. Geol.* 59 (3–4), pp. 257–269.
- Mills, M.M., Stormont, J.C. & Bauer, S.J. (2018): Micromechanical processes in consolidated granular salt. *Eng. Geol.* 239 (October 2017), pp. 206–213.
- Muhammad, N. (2015): *Deformation and transport processes in salt rocks: An experimental study exploring effects of pressure and stress relaxation.*
- Munson, D.E. & Dawson, P.R. (1979): Constitutive model for the low temperature creep of salt (with application to WIPP). SAND79-1853. Sandia National Laboratories, Albuquerque, NM. *Sandia Natl. Lab* pp. 31.
- Olivella, S., Gens, A. & Carrera, J. (1997): *CODE_BRIGHT User's Guide.*
- Peach, C.J. & Spiers, C.J. (1996): Influence of crystal plastic deformation on dilatancy and permeability development in synthetic salt rock. *Tectonophysics* 256 (1-4 SPEC. ISS.), pp. 101–128.
- Peach, C.J., Spiers, C.J. & Trimby, P.W. (2001): Effect of confining pressure on dilatation, recrystallization, and flow of rock salt at 150°C. *J. Geophys. Res. Solid Earth* 106 (B7), pp. 13315–13328.

- Pluymakers, A.M.H. & Spiers, C.J. (2015): Compaction creep of simulated anhydrite fault gouge by pressure solution: Theory v. experiments and implications for fault sealing. *Geol. Soc. Spec. Publ.* 409 (1), pp. 107–124.
- Poirier, J.-P. (1985): *Creep of crystals: high-temperature deformation processes in metals, ceramics and minerals..* Cambridge University Press.
- Poirier, J.P. (1976): On the symmetrical role of cross-slip of screw dislocations and climb of edge dislocations as recovery processes controlling high-temperature creep. *Rev. Phys. Appliquée* 11 (6), pp. 731–738.
- Popp, T. & Kern, H. (2000): Monitoring the state of microfracturing in rock salt during deformation by combined measurements of permeability and P- and S-wave velocities. *Phys. Chem. Earth, Part A Solid Earth Geod.* 25 (2), pp. 149–154.
- Prij, J. (1991): AN IMPROVED MODEL FOR THE CONVERGENCE OF AN EXCAVATION ON ROCK SALT.
- Pusch, R. (2009): *Geological storage of highly radioactive waste: current concepts and plans for radioactive waste disposal.*
- Rutqvist, J., Bäckström, A., Chijimatsu, M., Feng, X.T., Pan, P.Z., Hudson, J., Jing, L., Kobayashi, A., Koyama, T., Lee, H.S., Huang, X.H., Rinne, M. & Shen, B. (2009): A multiple-code simulation study of the long-term EDZ evolution of geological nuclear waste repositories. *Environ. Geol.* 57 (6), pp. 1313–1324.
- Schléder, Z. & Urai, J.L. (2005): Microstructural evolution of deformation-modified primary halite from the Middle Triassic Röt Formation at Hengelo, The Netherlands. *Int. J. Earth Sci.* 94 (5–6), pp. 941–955.
- Schmatz, J. & Urai, J.L. (2011): The interaction of migrating grain boundaries and fluid inclusions in naturally deformed quartz: A case study of a folded and partly recrystallized quartz vein from the Hunsrück Slate, Germany. *J. Struct. Geol.* 33 (4), pp. 468–480.
- Schutjens, P.M.T.M. & Spiers, C.J. (1999): Intergranular pressure solution in NaCl: Grain-to-grain contact experiments under the optical microscope. *Rev. l'Institut Fr. du Pet.* 54 (6), pp. 729–750.
- Senseny, P.E., Hansen, F.D., Russell, J.E., Carter, N.L. & Handin, J.W. (1992): Mechanical behaviour of rock salt: Phenomenology and micromechanisms. *Int. J. Rock Mech. Min. Sci.* 29 (4), pp. 363–378.
- Sinn, C.J.A., Giacomel, P., Peach, C.J. & Hangx, S.J.T. (2018): Effects of Plastic Deformation on the Transport Properties of Rocksalt. In: *SaltMech IX*.
- Sjaardema, G. & Kreig, R.D. (1987): A constitutive model for the consolidation of WIPP (Waste Isolation Pilot Plant) crushed salt and its use in analyses of backfilled shaft

and drift configurations 29000 (October).

- Spiers, C.J. & Carter, N.L. (1998): Microphysics of rocksalt flow in nature. *Ser. rock soil Mech.* pp. 115–128.
- Spiers, C.J., Schutjens, P.M.T.M.T.M., Brzesowsky, R.H., Peach, C.J., Liezenberg, J.L. & Zwart, H.J. (1990): Experimental determination of constitutive parameters governing creep of rocksalt by pressure solution. *Geol. Soc. Spec. Publ.* 54 (54), pp. 215–227.
- Stührenberg, D. (2013): R + D Radioactive Waste Repository Compaction Test TK-031 (August).
- Stührenberg, D. (2017): Long-term laboratory investigation on backfill. *Mech. Behav. Salt–Understanding THMC Process. Salt.*
- Stührenberg, D. & Zhang, C.L. (1995): Stührenberg, D., and C. L. Zhang. Results of experiments on the compaction and permeability behavior of crushed salt. *Am. Soc. Mech. Eng.*
- Ter Heege, J.H., De Bresser, J.H.P. & Spiers, C.J. (2004): Composite flow laws for crystalline materials with log-normally distributed grain size: Theory and application to olivine. *J. Struct. Geol.* 26 (9), pp. 1693–1705.
- Ter Heege, J.H., De Bresser, J.H.P. & Spiers, C.J. (2005a): Dynamic recrystallization of wet synthetic polycrystalline halite: Dependence of grain size distribution on flow stress, temperature and strain. *Tectonophysics* 396 (1–2), pp. 35–57.
- Ter Heege, J.H., De Bresser, J.H.P. & Spiers, C.J. (2005b): Rheological behaviour of synthetic rocksalt: The interplay between water, dynamic recrystallization and deformation mechanisms. *J. Struct. Geol.* 27 (6), pp. 948–963.
- Timoshenko, S. (1956): *Elements of strength of materials.*
- Tsang, C.F., Bernier, F. & Davies, C. (2005): Geohydromechanical processes in the Excavation Damaged Zone in crystalline rock, rock salt, and indurated and plastic clays - In the context of radioactive waste disposal. *Int. J. Rock Mech. Min. Sci.* 42 (1), pp. 109–125.
- Umwelt, T. & Korthaus, E. (1998): Forschungszentrum Karlsruhe Experiments on Crushed Salt Consolidation with True Triaxial Testing Device as a Contribution to an EC Benchmark Exercise.
- URAI, J., SPIERS, C., PEACH, C., FRANSSEN, R. & LIEZENBERG, J. (1987): Deformation mechanisms operating in naturally deformed halite rocks as deduced from microstructural investigations. *Geol. en Mijnb.* 66 (2), pp. 165–176.
- Urai, J.L., Schlöder, Z., Spiers, C.J., Kukla, P. a, Lange, J.-M. & Röhling, H.-G. (2008): Flow and Transport Properties of Salt Rocks. *Geo 2008; Int. Conf. 106th Annu. Meet. Dtsch.*

- Gesellschaft für Geowissenschaften e. V. 98th Annu. Meet. Geol. Vereinigung e.V. 60*, pp. 61.
- Urai, J.L., Spiers, C.J., Zwart, H.J. & Lister, G.S. (1986): Weakening of rock salt by water during long-term creep. *Nature* 324 (6097), pp. 554–557.
- Vons, L.H. & Prij, J. (1988): Final disposal of radwaste in salt formations in the Netherlands (OPLA research program). *Nucl. Eur.*
- Wawersik, W.R. & Zeuch, D.H. (1986): Modeling and mechanistic interpretation of creep of rock salt below 200°C. *Tectonophysics* 121 (2–4), pp. 125–152.
- Weertman, J. (1955): Theory of steady-state creep based on dislocation climb. *J. Appl. Phys.* 26 (10), pp. 1213–1217.
- Zhang, X., Grupa, J.B., Spiers, C.J., Peach, C.J., Blomen, E.C., Houben, M.E., Ten Hove, A., Fokkens, J.H. & Haverkate, B.R.W. (2008): *THERESA WP 3.2 Deliverable 6*.
- Zhang, X., Peach, C.J., Grupa, J. & Spiers, C.J. (2007): Stress relaxation experiments on compacted granular salt: Effects of water. *Proc. 6th Conf. Mech. Behav. Salt "SALTMECH6" - Mech. Behav. Salt - Underst. THMC Process. Salt* pp. 159–166.
- Zhu, C. & Arson, C. (2015): A Model of Damage and Healing Coupling Halite Thermo-mechanical Behavior to Microstructure Evolution. *Geotech. Geol. Eng.* 33 (2), pp. 389–410.

A Appendices

A.1 BGR-CS3 model

The BGR-CS3 model considers elastic and creep deformation of crushed salt as well as deformation due to grain rearrangement (Krohn et al. 2017). The elastic component is described by implementing Hooke's law for a Young's modulus which is dependent on the density (hence porosity) of the backfill, using a fit to measurements of the Young's modulus at a range of porosities (e.g. Sjaardema & Kreig 1987). The other models discussed here use similar approaches for the elastic strain (and strain rate). For creep and grain rearrangement, the BGR-CS3 model assumes an idealized model, with the unit crystal shown in Figure A-1. Two creep mechanism laws are considered: a power law creep and a humidity creep law. The term for power-law creep is given by:

$$\dot{\varepsilon}_{v,N} = 2A_{BGR} \exp\left(\frac{-Q_{BGR}}{RT}\right) \left(\frac{\sigma^{local} - \sigma^{rv}}{1-z}\right)^{n-1} \cot(\alpha) \sqrt{U} \frac{P}{U'} e^{\frac{1}{1+e}} \quad \text{Eq. 4.1}$$

In which A_{BGR} is a material parameter for power-law (Norton) creep, Q_{BGR} the apparent activation energy of the power law mechanism, n is the stress exponent for the Norton law which is typically taken as 5. σ^{local} is the local stress (MPa) at the contact zone and σ^{rv} is the frictional hardening stress (MPa), which increases with decreasing porosity. P is the hydrostatic stress (MPa). U is the relative contact area (mm), U' the extension of relative contact area (mm), α is the contact angle ($^\circ$), e is the void ratio (-) and k is the ratio of solid mass over the total mass (see Figure A-1). The local stress is given as a function of hydrostatic stress, deviatoric (Von Mises equivalent) stress and contact area, given by:

$$\sigma^{local} = \sqrt{\left(\frac{P}{U'}\right)^2 + b \left(\frac{q}{U'^B}\right)^2} \quad \text{Eq. 4.2}$$

In which q is the deviatoric stress and b, β are fit parameters with a value close to 1. Basically, it can be envisaged as a power law taking into account the strength-, porosity- and contact shape evolution with ongoing backfill compaction. The Norton creep law (or other creep laws with $n \approx 5$, also for dense salt) is widely used, because it is in good agreement with experimental data on backfill compaction above 10 MPa (Korthaus 1996; Kröhn et al. 2015; Zhang et al. 2007). However, it underestimates creep rates at low stresses when moisture or brine is present. Hence Krohn et al. 2017 incorporated a second term for humidity creep, implicitly assuming ionic diffusion through an adsorbed film, using a linear creep law given by:

$$\dot{\varepsilon}_{v_h} = \frac{D^{diff}}{R^{contact} D_i [1 + \cot(\alpha)]^{\frac{1}{3}}} \frac{(1+ke)^{\frac{2}{3}}}{k(1+e)} \cdot \exp\left(\frac{-Q_{diff}}{RT}\right) \cdot \sinh\left(\frac{3k\sigma^{local}}{TR^{contact}}\right) \quad \text{Eq. 4.3}$$

in which D^{diff} is a parameter taking into account the diffusion ($m^2 s^{-1}$), Q_{diff} is the activation energy for diffusion, k' is a material parameter ($K m MPa^{-1}$). $R^{contact}$ describes the contact area and is a function of grain size, contact width (rectangle in Figure A-1) and void ratio. The grain rearrangement takes into account that fracturing occurs when the local stress exceeds a given stress limit, which is dependent on grain size. A fit parameter is then used to relate this to the volumetric strain resulting from fracturing. The volumetric creep rates of these three mechanisms are then added to calculate the total volumetric creep rate.

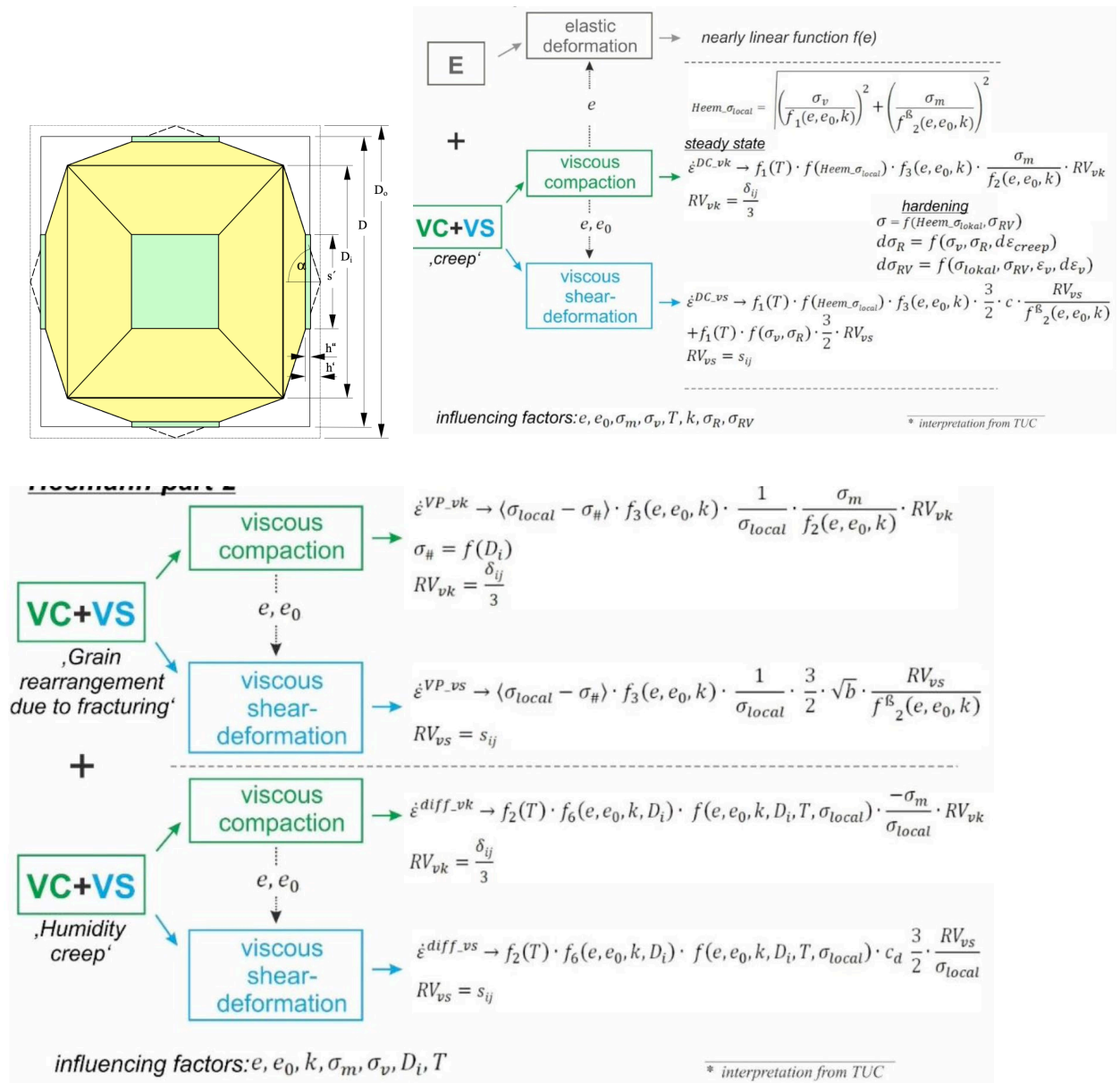


Figure A-1: (top left) idealized model of a unit crystal used to derive the BGR-CS3 model, (top right/bottom) constitutive laws for the BGR-CS3 models (Czaikowski et al. 2020).

A.2 Callahan model

The Callahan model (Callahan & Hansen 1999) considers elastic strains and inelastic (creep) strains. For the inelastic strains two creep mechanisms are considered: dislocation creep and pressure solution creep. The dislocation creep model is based on the Multi-mechanism deformation model (MD model) originally developed by Munson & Dawson 1979. The dislocation creep model contains a transient part (see Callahan & Hansen 1999 for details) and three dislocation creep mechanisms: dislocation climb ($\dot{\epsilon}_{s1}$), an unidentified but experimentally observed mechanism ($\dot{\epsilon}_{s2}$) and dislocation slip ($\dot{\epsilon}_{s3}$). The stress exponent of dislocation climb, and the unidentified mechanism are respectively 5.5 and 5.0, with activation energies of 1045 and 418 kJ/mol^{-1} . The stress dependence of dislocation slip assumed in this law is not known as it is given as a hyperbolic sine. These mechanisms are assumed to occur in parallel and the total dislocation creep rate is the sum of the four creep laws. The kinetic equation used for pressure solution is a modified version of Spiers et al. 1990, given by:

$$\dot{\epsilon}_{v-ps} = \frac{r_1 w^a}{d^p} \exp\left(\frac{\exp(r_3 e_v)}{(\exp(e_v)-1)^{r_4}}\right) \frac{\exp\left(\frac{-Q_{ps}}{RT}\right)}{T} \Gamma \sigma_{eq} \quad \text{Eq. 4.4}$$

in which r_1, r_3, r_4, a and p are material parameters, d is the grain size (m), e_v is the volumetric strain relative to the original configuration (-), w is the moisture content (wt%) Γ is a geometry function. Note that the term $r_1 w^a$ to account for diffusion would be similar as considering a change in effective surface diffusivity in the original pressure solution model (see Section 2.2.2). When the moisture content is 0, the pressure solution strain rate reduces to 0.

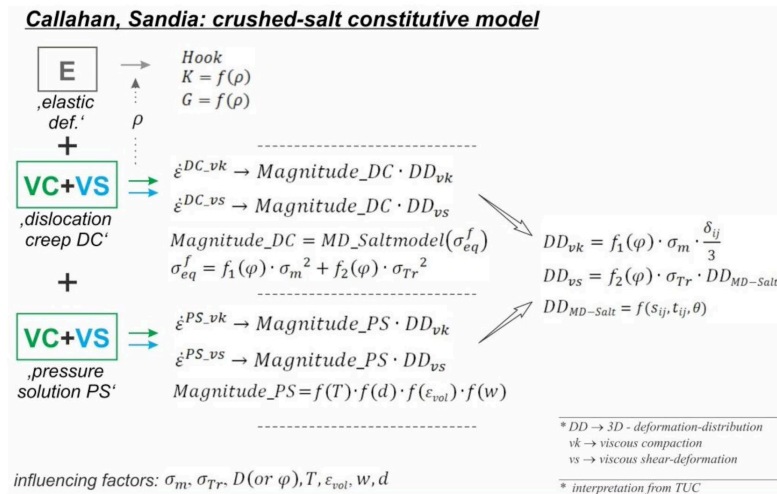


Figure A-2: constitutive laws for the Callahan model (after Czaikowski et al. 2020).

A.3 C-WIPP models

The original C-WIPP model was developed by Sjaardema & Kreig 1987 to describe backfill compaction of the WIPP facility. The crushed salt deformation is modelled as a sum of elastic deformation, volume-preserving creep and compaction creep. The volume preserving creep contains a transient and a stationary creep part. The stationary creep part is modelled as power law creep with a stress exponent of $n \approx 5$ (see Section A. 1), by which effective stress is divided by $1 - \phi$ to account for the effect of porosity on grain contact stresses. The C-WIPP model was modified by BGE-TEC to include a more extensive stress and porosity function, to account for (1) the observed change in stress dependence of dry granular salt vs. moist granular salt (Kröhn et al. 2009); and (2) a larger dependance of strain rates on porosity at lower porosities. IfG also modified the C-WIPP model, such that the compaction rate goes to zero for small porosities. In addition, they extended the original C-WIPP model to account for deviatoric creep by replacing the effective stress term with an isotropic and deviatoric term to accommodate triaxial stress states (Czaikowski et al. 2020). The model of C-WIPP was further modified by TUC to account for a functional relationship between compaction rates and porosity and to allow for different stress geometries (Czaikowski et al. 2020). A difference between the C-WIPP models and the BGR-CS3/Callahan models is that the influence of moisture content on compaction creep is not considered here, or at least not explicitly.

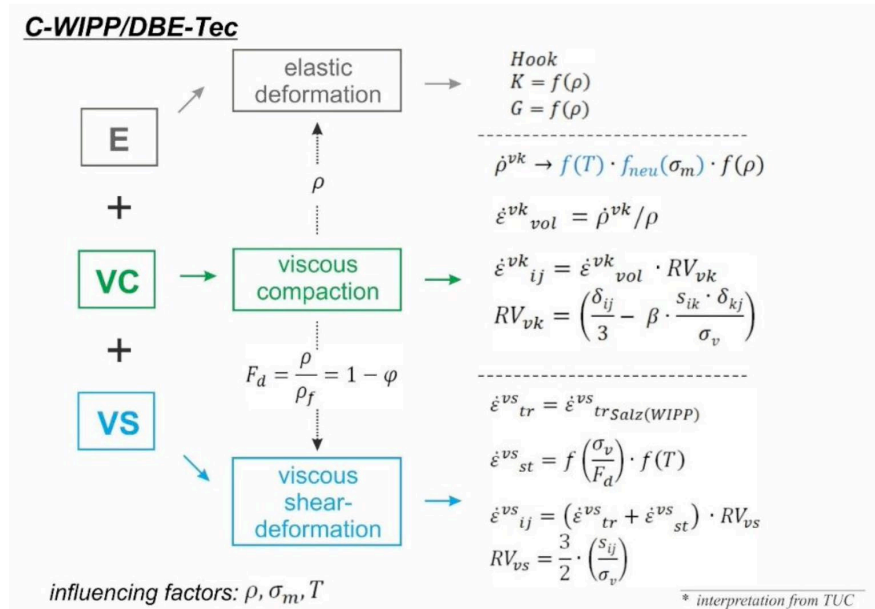


Figure A-3: C-WIPP model showing in blue the modifications made by BGE-TEC to allow for a variation in strain rate dependency on stress at different stresses (after Czaikowski et al. 2020).

A.4 Triaxial isotropic compaction tests TK-031 and TK-033

Experimental method

Both TK-031 and TK-033 were on raw crushed material retrieved from the Asse mine (“Speisesalz”) (Czaikowski et al. 2020; Krohn et al. 2017; Stührenberg 2013). For the experiment all grains larger than 8mm were removed from the mixture. The material was pre-compacted for 16 days at a constant strain rate of 0.136 mm/hr, with a maximum load during pre-compaction of 30 MPa to a final length of 200mm and a diameter of 100mm. The initial porosity after pre-compaction was equal to 21%. The tests were performed in a triaxial test apparatus with multi-step loading up to a final mean stress of 20.4 MPa at a constant temperature of 50 °C.

Experimental results

Compaction test TK-031 included five loading stages with a mean stress of 10.3; 12.3; 15.3; 18.4 and 20.4 MPa, with creep phase durations of 7, 19, 26, 27 and 202 days respectively. The loading rate during each phase set between 1 and 3 MPa/day. The moisture content of the sample was equal to 0.05wt%. The strain rate during all loading stages varies from $10^{-8} - 10^{-9} s^{-1}$ from the beginning to the end of each loading stage. The relative similar strain rates in each phase are caused by a combination of decreasing porosity and increasing stress. The decrease in strain rate during each creep rate is a result of ongoing porosity reduction and transient creep. The final porosity after 300 days of compaction is equal to 7.5%.

The second triaxial test (TK-033) was performed under the same set of conditions, but with only two loading stages of 15.3 MPa for 34 days and of 20.4 MPa for 366 days. The initial porosity after pre-compaction was equal to 21%. Because of a first loading stage of 15.3 MPa, with respect to a loading stage of 10 MPa, the strain rates during the first loading stage are 1 order of magnitude faster than the strain rates observed in TK-031. After the first loading stage porosity is reduced to 8.5%. During the second stage a gradual decrease in strain rates from $10^{-8} - 10^{-10} s^{-1}$ is observed as porosity is reduced from 8.4% to 5.5%.

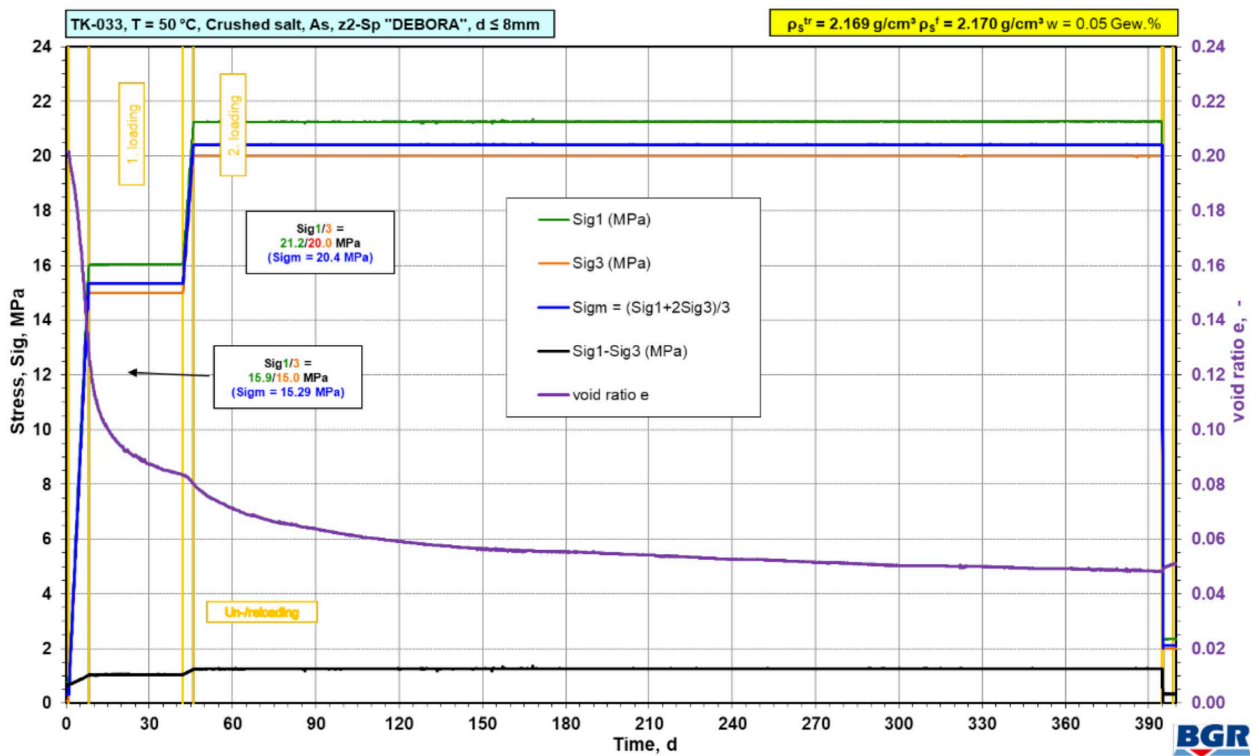
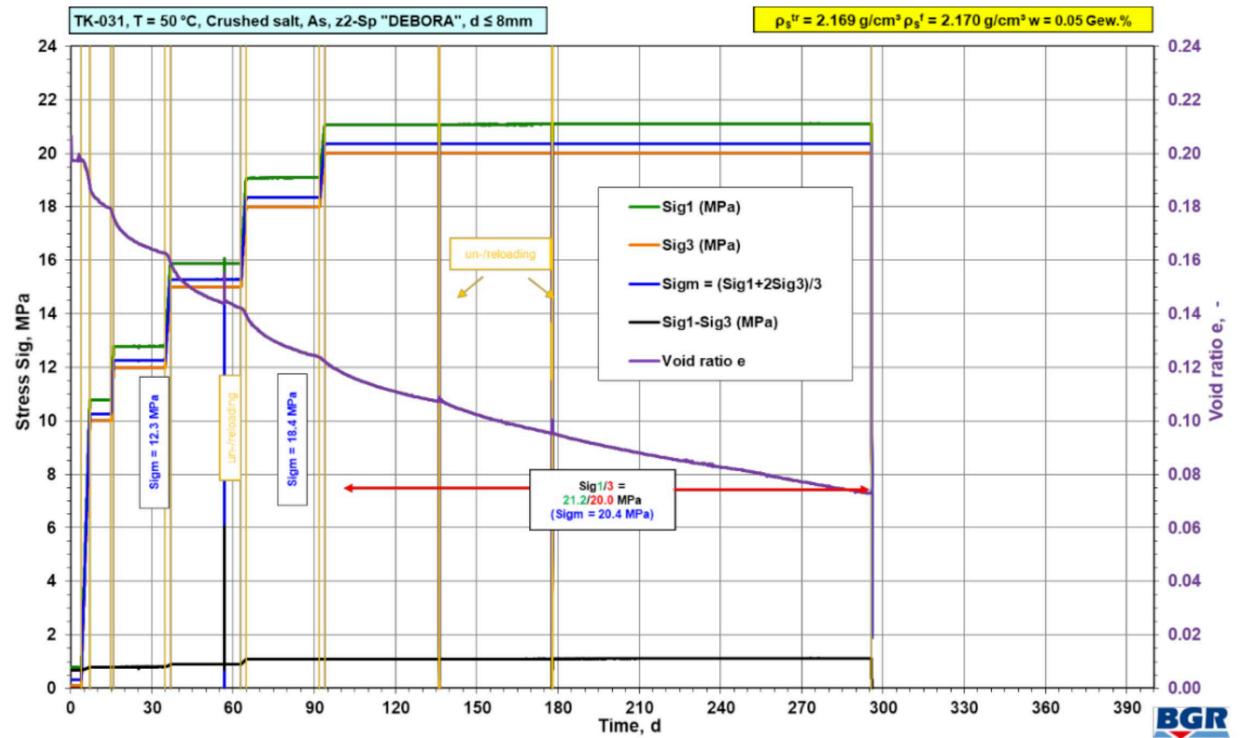


Figure A-4: Development of stress and void ratio (porosity) as a function of time in days for (top) TK-031 and (bottom) TK-033 (Krohn et al. 2017).

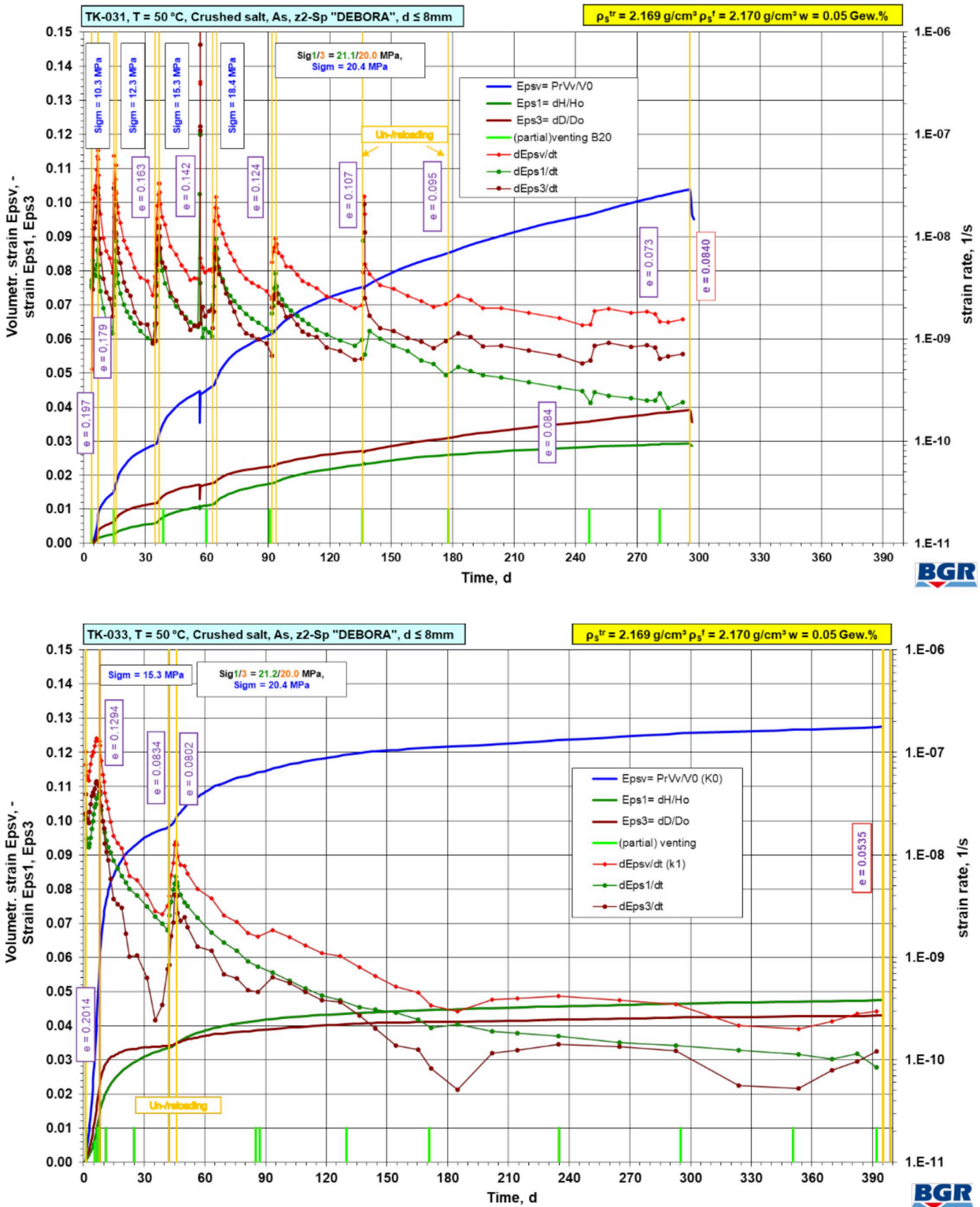


Figure A-5: Development of strain and strain rate versus time in days for (top) TK-031 and (bottom) TK-033 (Krohn et al. 2017). Note that strain rate in TK-031 is in the same range for all loading stages as the decrease in strain rates with decreasing porosity are compensated by an increase in stress. For TK-033, initial strain rates are 1 order of magnitude faster as the first loading stage is at 15.3 MPa compared to 10 MPa for TK-031. During the very long (1 year) second loading stage strain rates decrease by 2 orders of magnitude as porosity is reduced from 8.1% to 5.5%.

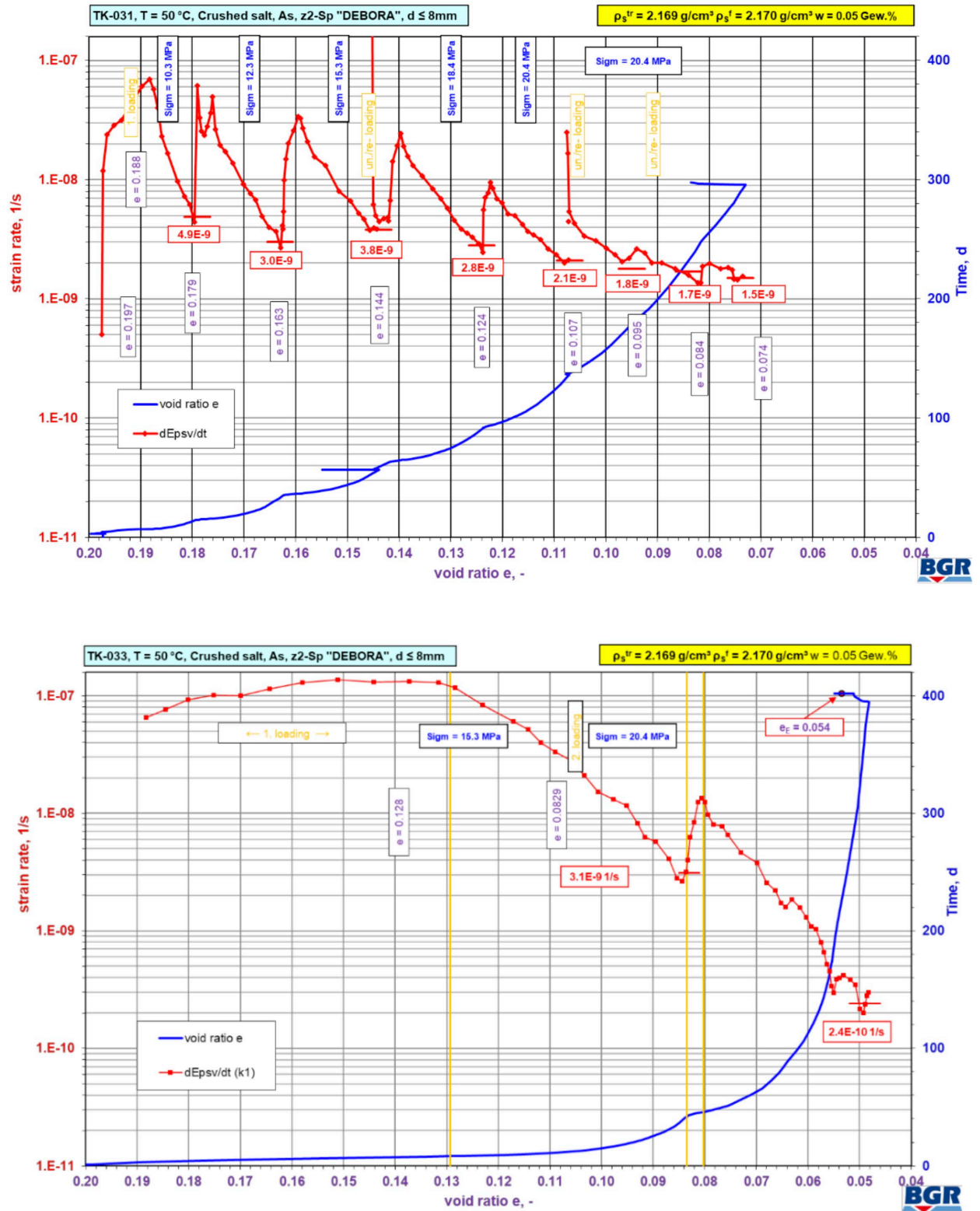


Figure A-6: Development of strain rate versus void ratio (porosity) for (top) TK-031 and (bottom) TK-033 (Krohn et al. 2017).

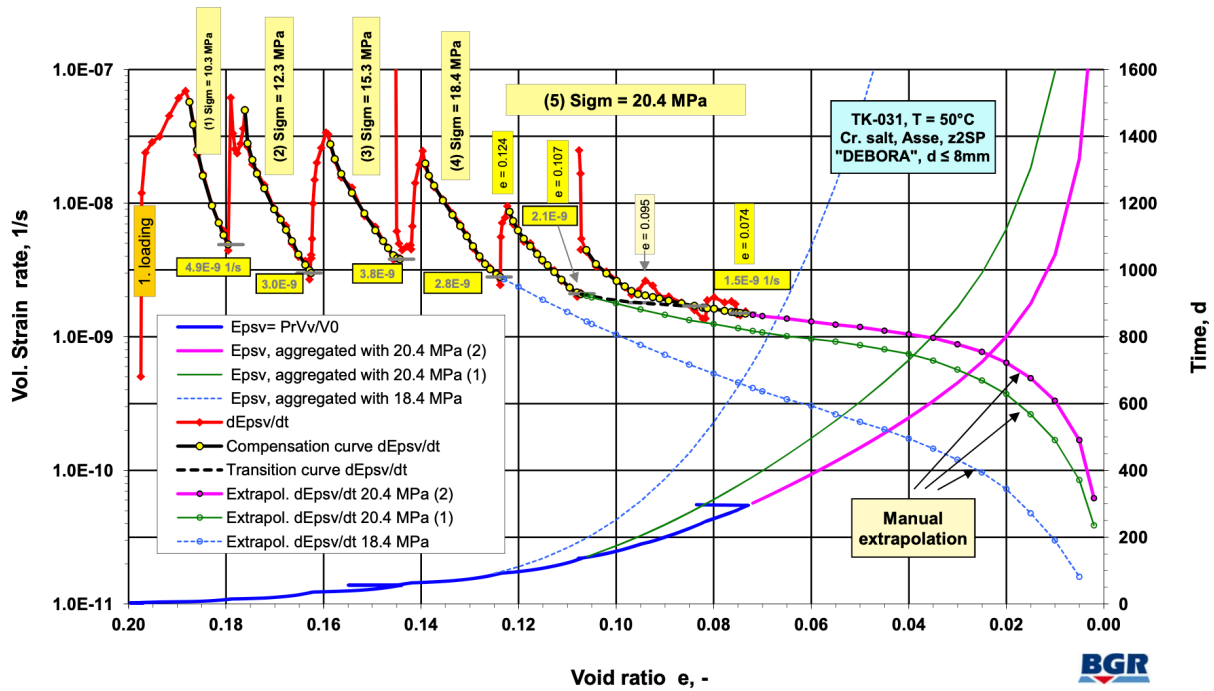


Figure A-7: Extrapolation of strain rates of test TK-031 (Krohn et al. 2017).

Using the general trends of each loading cycle, a qualitative basis has been created for the original objective of quantifying the results of the less complicated oedometer tests with the results of the triaxial compaction tests.

To estimate the material behaviour beyond the change in compaction occurring during the course of the experiment, the compaction rate trend derived from the loading phase at a stress of 20.4 MPa for a period of 200 days, was extrapolated as a function of the void ratio (see Figure A-7). The entered equalisation curve was extended in line with the trend until the progressive asymptotic decline in the compaction rate expected with increasing compaction reaches a void ratio of 0. The compaction increments calculated and added together for small time intervals produce a plausible compaction curve trend which reaches a void ratio of $e = 0.02$ after 2.2 years (see Figure A-7, approximately 800 days). This takes 3 years for a slightly less favourable version under the same load. The curve for the extrapolation oriented to a constant stress of 18.4 MPa takes 11 years to reach a void ratio of $e = 0.02$.

A.5 Isostatic long-term compaction test by IfG

Experimental method

The long-term experiments by IfG (TCC1-TCC6, Czaikowski et al. 2020) were performed on the KOMPASS reference material, which consist of three grain size fractions with mean grain sizes of 0.14 mm, 0.49 mm and 1.90 mm with volume ratios of 65.6%, 20.2% and 14.2% respectively. The material was pre-compacted using the small IfG compaction cell at room temperature with load steps of 5, 10, 15 and 20 MPa with each load step taking 24 hours. After pre-compaction samples had a length of 100 mm and a diameter of 60 mm.

The isostatic compaction experiments at IfG were performed under axisymmetric conditions with an applied confining pressure ($\sigma_2 = \sigma_3$) and the axial stress controlled independently, although all experiments were performed under isostatic conditions. Experiments TCC1-TCC3 were performed without adding moisture to the sample, whereas TCC5 and TCC6 were performed with 1% of saturated brine added to the sample by spraying the crushed salt. All samples were compacted in different stages of increasing isostatic stress, all up to a total duration of 197 days. Dry experiments were performed at 60 °C, wet experiments at 25 °C. For the exact loads and durations see Table A-1.

| IfG – Lab.-test-no. (isostatic creep tests) | Humidity | σ_{iso} | Stage duration | Creep phase - Porosity change - | |
|--|------------|----------------|-------------------|------------------------------------|----------------|
| | | | | $\Phi_{initial}$ | Φ_{final} |
| | | [MPa] | [d] | [%] | [%] |
| 684/OEDO1/TCC1 | dry | 5 | 31.9 | 14.39 | 14.32 |
| (25 °C) | dry | 10 | 35.1 | 13.94 | 13.82 |
| | dry | 20 | 92.0 | 13.07 | 11.09 |
| Total test time: 197 d | +T (60 °C) | 20 | 38.0 | - | - |
| 684/OEDO1/TCC2 | dry | 10 | 31.9 | 15.60 | 15.49 |
| (25 °C) | dry | 20 | 35.1 | 14.43 | 12.83 |
| | dry | 30 | 92.0 | 12.03 | 7.77 |
| Total test time: 197 d | +T (60 °C) | 30 | 38.0 | - | - |
| 684/OEDO1/TCC3 | dry | 1 | 31.9 | 12.90 | 12.84 |
| (25 °C) | dry | 5 | 35.1 | 12.24 | 12.33 |
| | dry | 10 | 92.0 | 11.90 | 11.70 |
| Total test time: 197 d | +T (60 °C) | 10 | 38.0 | - | - |
| 684/OEDO1/TCC5 | wet (1%) | 5 | 31.9 | 16.00 | 7.82 |
| (25 °C) | wet (1%) | 10 | 35.1 | 7.66 | 3.98 |
| Total test time: 197 d | wet (1%) | 20 | 92.0 | 4.18 | 1.36 |
| 684/OEDO1/TCC6 | wet (1%) | 1 | 31.9 | 16.21 | 10.80 |
| (25 °C) | wet (1%) | 5 | 35.1 | 10.43 | 5.01 |
| Total test time: 197 d | wet (1%) | 10 | 92.0 | 4.71 | 0.88 |

Table A-1: Experimental conditions of the long-term compaction experiments at IfG

Experimental results (mathematical fits)

The outcome of the multi-stage compaction creep test TCC1-TCC5 are obtained and presented in Figure A-9a and 3-6b. The axial strain is measured and using the assumption that the volumetric strain can be estimated by multiplying the axial strain by 3, the volumetric strain is calculated. Subsequently the volumetric strain is fitted using power law functions for each loading cycle of each experiment, which directly can be used to estimate the porosity reduction and the derivative of the power law is used to calculate volumetric strain rates. These graphs are displayed in Figure A-8 and Figure A-9.

At dry conditions (TCC1-3), the increase of isostatic stress from 1 MPa to 20 MPa results in an increase of compaction rates of 2 orders of magnitude (see Figure A-9a), whereas between 20 and 30 MPa, the increase in compaction rate is just 1 order of magnitude. The addition of 1wt% water (TCC5-6) significantly increases the compaction creep rates by 1.5 orders of magnitude at 10 MPa and 3 orders of magnitude at 1 MPa. For a wet sample, a porosity of near 1% is reached (1.36% in TCC5 and 0.88% in TCC6) within the timescale of the experiment, after three steps of increasing stress of 1, 5 to 10 MPa.

Other experiments (e.g. Zhang et al. 2007) show a clear indication of diminishing creep rates at very low porosities (around 1%). Therefore, extrapolation using a power law fit may give unrealistic results. In addition, these extrapolated power law fits result in negative porosities in all the wet experiments after a few years. Extrapolating these curves result in a porosity of zero after a few years, hence compaction creep cannot continue for 1000 years. Unfortunately the experimental data is not yet published anywhere outside of the GRS-608 KOMPASS report (Czaikowski et al. 2020).

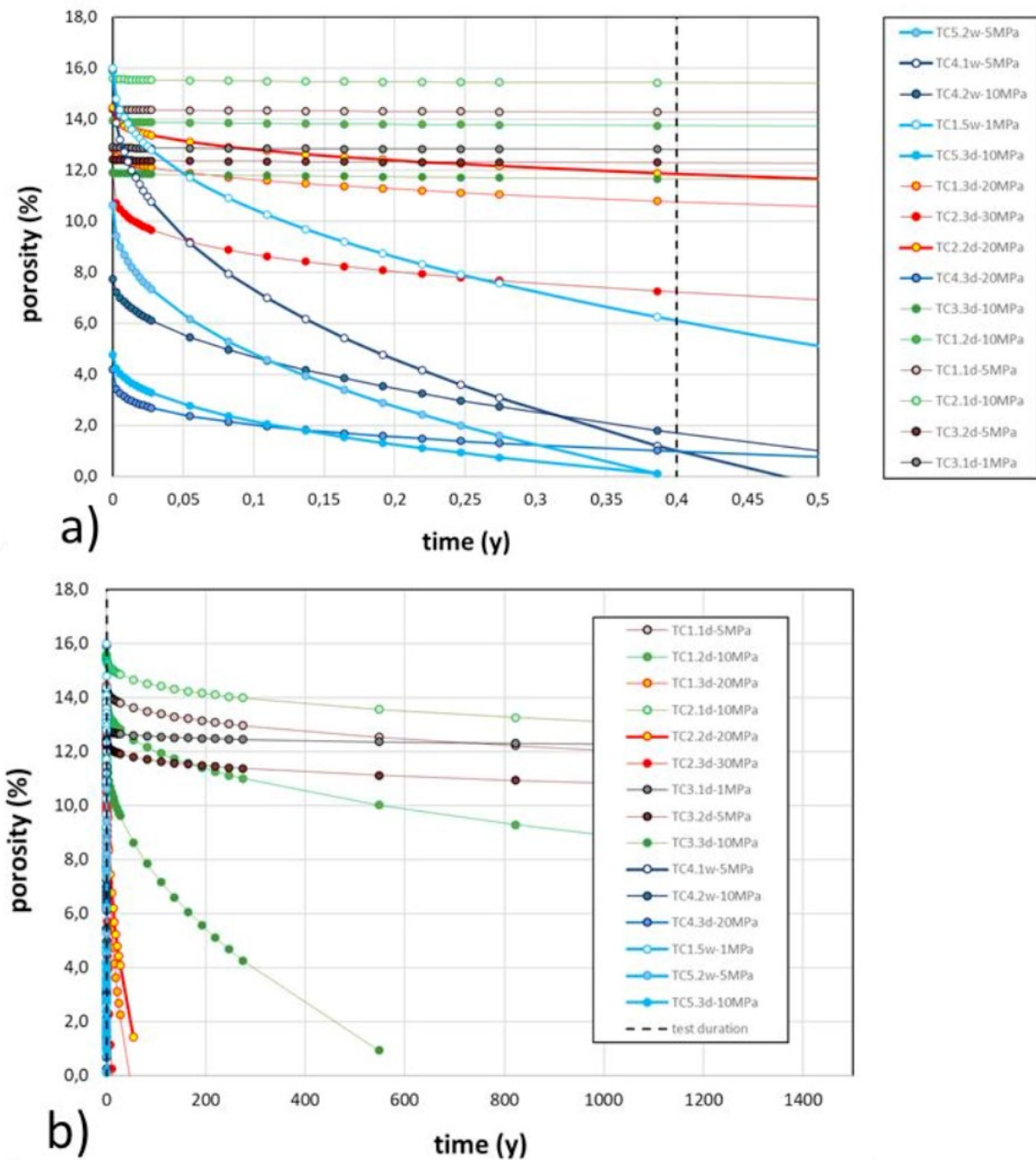


Figure A-8: calculated porosity reduction curve for (top) the length of the experiment (0.4 years) and (bottom) extrapolated to longer timescales (1400 years). Note that actually the experiments consist of individual loading steps, of which the longest one takes 92 days, so in reality anything after 0.25 years is mathematical extrapolation (and not after 0.4 years) (Czaikowski et al. 2020).

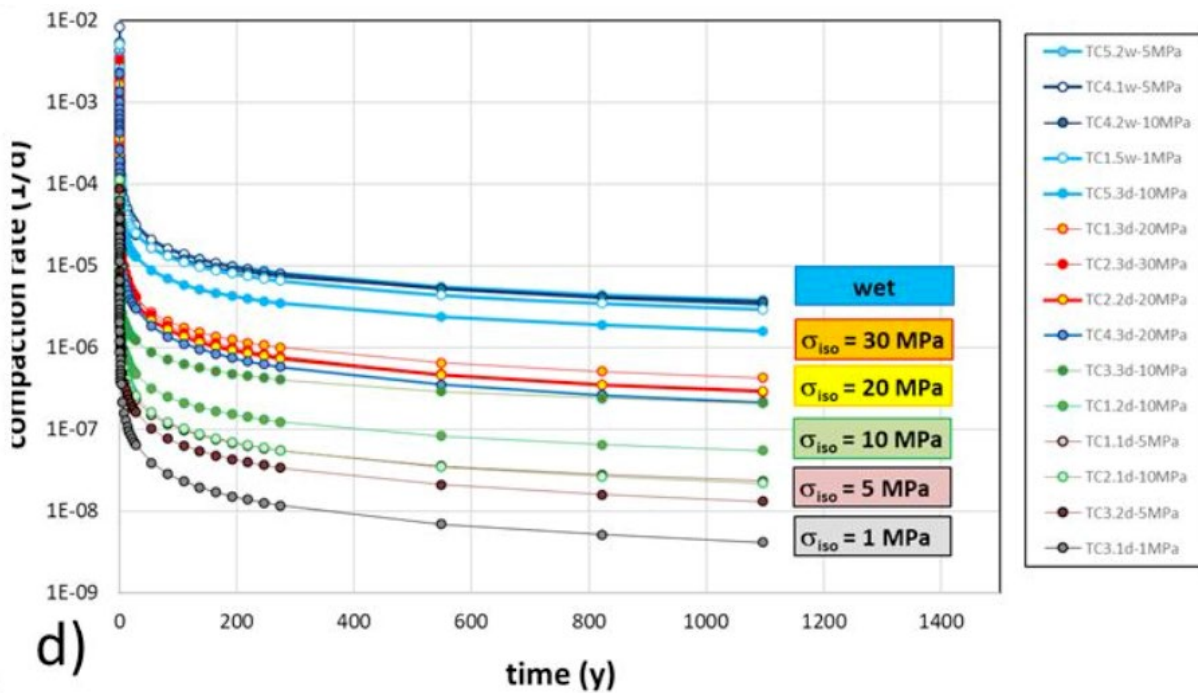
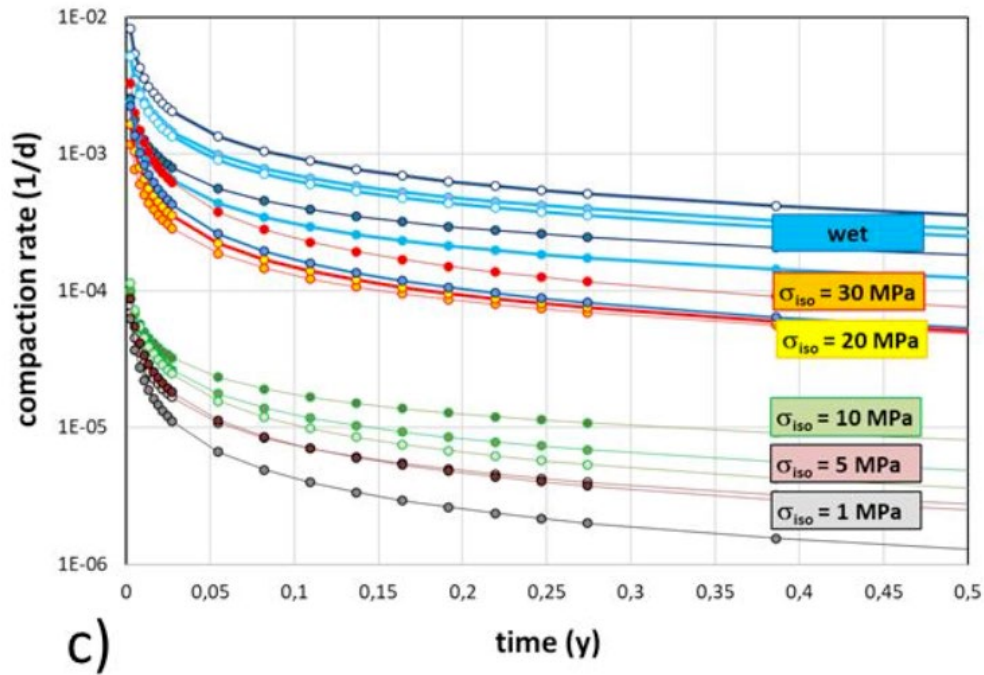


Figure A-9: calculated compaction creep rates (/day) for (top) the duration of the experiment (0.4 years) and (bottom) extrapolated to longer timescales (1400 years). Note that the extrapolation of these power-law curves results in near constant compaction creep after 250 years (Czaikowski et al. 2020).

A.6 TUC multi-stage test with isotropic and deviatoric stages

Experimental method

The TUC-V2 experiment was performed on the same KOMPASS mixture material from the Sondershausen mine as the experiments on the TCC samples (Czaikowski et al. 2020). The material was pre-compaction in an autoclave by applying a high radial stress combined with a lower axial stress to allow for the sample to elongate in the axial direction. The radial load was applied stepwise by applying 5, 10 and 15 MPa stress, with a uniformly specified compaction time of 3 days. The pre-compacted sample had a length of 180 mm and a diameter of 90 mm. The initial porosity (e.g. after pre-compaction) was equal to 16.7% and a moisture content of 0.5wt% water was added to the sample. The temperature during the experiment was kept constant at 30 °C. The load was increased in 5 stages during the experiment, from 4.2-8.2-12.2-16.2-20.2 MPa with a duration of 30 days each (see Figure A-10). Each load stage is then characterized by a 10-day approximately isotropic load, followed by a 10-day deviatoric load with a deviatoric stress of 8 MPa, again followed by a 10-day isotropic load. The total duration of the experiment was equal to 150 days. Note that the deviatoric load was applied by lowering the radial stress ($\sigma_2 = \sigma_3$), while increasing the axial stress, thereby keeping the mean stress constant.

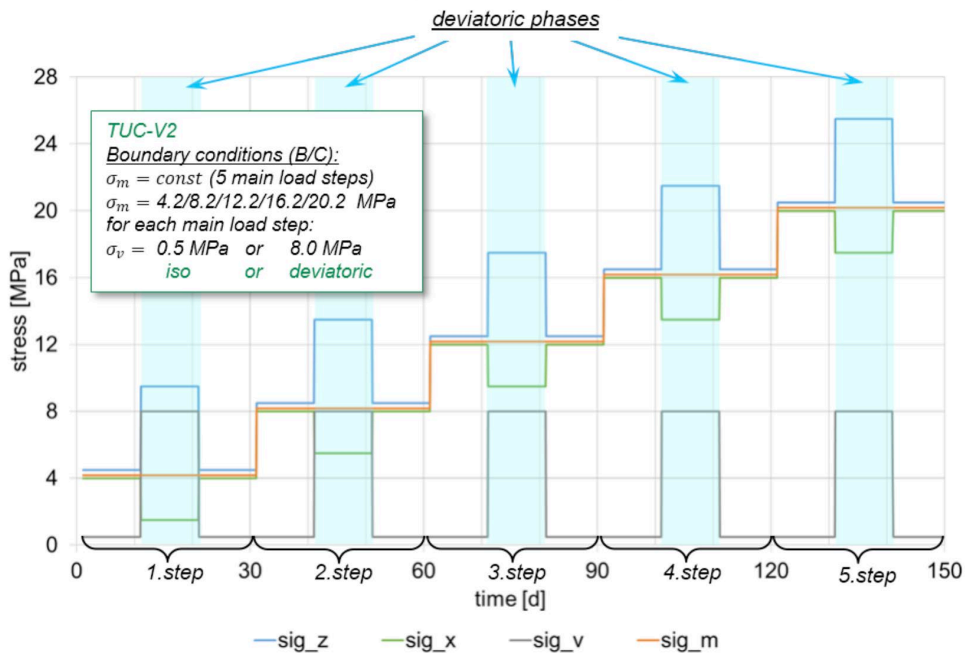


Figure A-10: Loading history for the multi-stage long-term test TUC-V2 (Czaikowski et al. 2020)

Experimental results

The evolution of strain and strain rate during experiment TUC-V2 are shown in Figure A-11. The smoothed volumetric strain in Figure A-11a is used to calculate the strain rate in Figure A-11b. The final porosity after 150 days was equal to 9.51%. The strain rate varies from $10^{-7} s^{-1}$ after increasing the loads to $10^{-9} s^{-1}$ in the first stage at low stress (4.0 MPa) and high porosity (16-15%) and again $10^{-9} s^{-1}$ in the final stage at a high stress (20.4 MPa) and a low porosity (10-9%). Strain rates are comparable to the TK-031 experiment, although there is a difference in water content of 0.5wt% (for this experiment) and 0.05wt% for TK-031. Note that both increasing the mean effective stress and applying a deviatoric stress, while keeping the mean effective stress constant, results in a rapid increase in strain rates. However, after loading strain-rates converge to similar values for both the isotropic and the deviatoric parts.

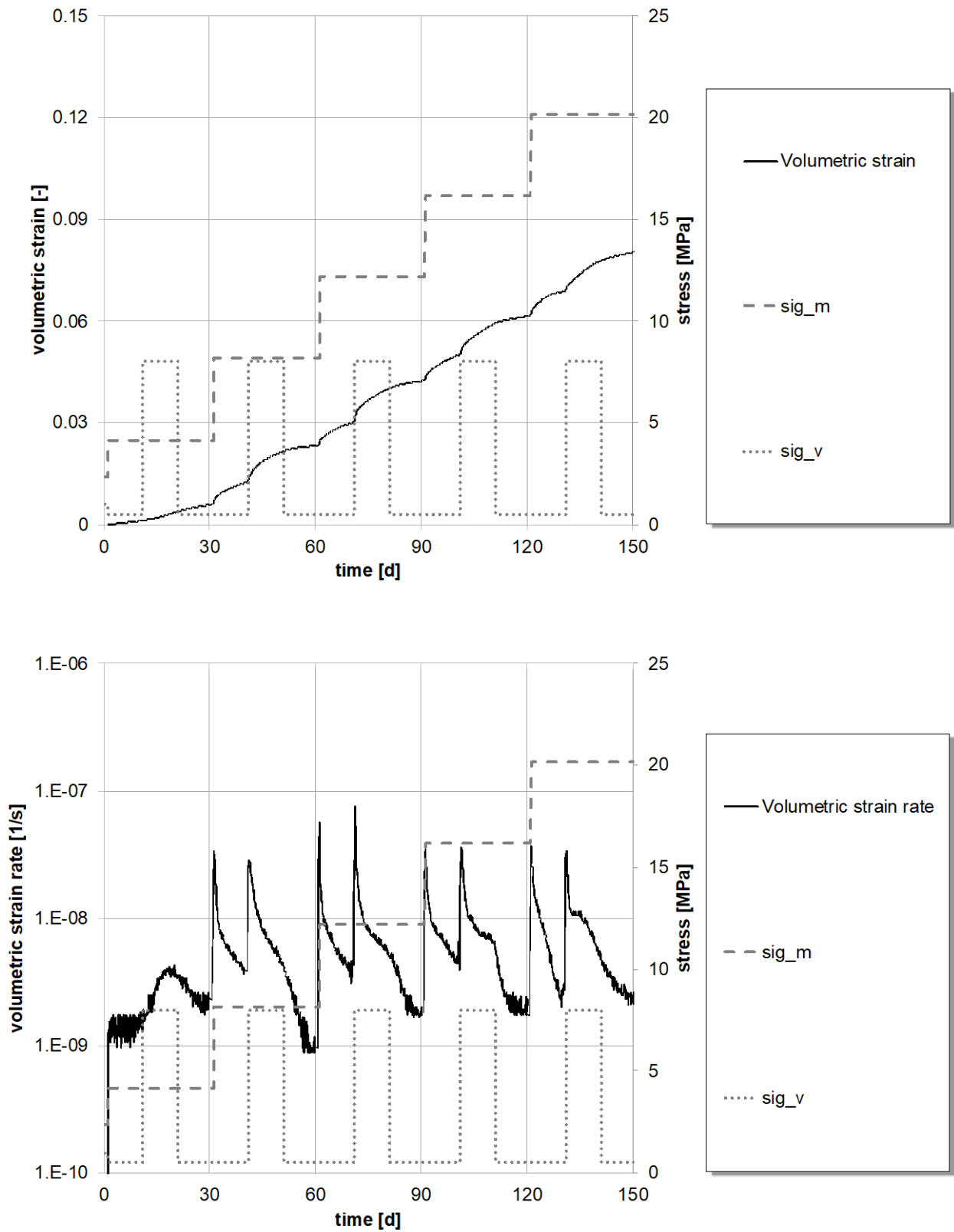


Figure A-11: Experimental results for the multi-stage long-term test TUC-V2. Showing in (top) the evolution of applied stress and volumetric strain and in (bottom) the evolution of volumetric strain rate (Czaikowski et al. 2020).

A.7 Hydrostatic compaction creep tests by Sandia

Experimental method

Backfill from mining operations at the WIPP facility (bedded salt formation) and the Avery island mine (domal salt formation) were compacted in laboratory hydrostatic creep tests in a pressure vessel with isostatic stresses up to 38 MPa at constant temperatures up to 250 °C (Bauer et al. 2015; Mills et al. 2018) (see Table A-2). The grains were selected to exclude particle with a size larger than 9.5 mm. Further sieving was performed to create a well distributed fraction with about 60% finer than 2.8mm and dried at 110 °C. Four samples were exposed to 100% relative humidity until 1 wt. % moisture content was achieved. The created samples had an initial length of 122 mm and a diameter of 105 mm. Four of the samples were pre-compacted to a porosity of about 20% at hydrostatic pressures of 19 to 38 MPa (see Table A-2). Axial strains were measured using an LVDT (linear variable differential transformer) and lateral strains were measured with Schuler gauges. The tests had a duration between a few days up to a few months and final porosities were below 10%.

After compaction samples were cut and impregnated with blue stained raisin and thin sectioned, while others were vacuum impregnated with low viscosity kit for microstructural observations. Observations include optical and scanning electron microscope (SEM). The thin sections for optical observations were etched to highlight grain substructure and boundaries.

Table A-2: compacted samples and associated conditions. Samples that were not pre-compacted had a starting porosity of 30-40%. W=Waste Isolation Pilot Plant (WIPP), A=Avery Island (Mills et al. 2018).

| Sample name | Temperature (°C) | Hydrostatic stress (MPa) | Moisture added | Elapsed consolidation time (days) | Pre-conditioned | Core porosity (%) | Point counting porosity (%) |
|-------------|------------------|--------------------------|----------------|-----------------------------------|-----------------|-------------------|-----------------------------|
| W90-1 | 90 | 20 | None | 111 | No | 8.0 | 8.33 |
| W90-2 | 90 | 20 | 1% | 16 | No | 2.0 | 1.89 |
| W90-4 | 90 | 20 | 1% | 5 | Yes | 3.5 | 4.45 |
| W90-7 | 90 | 20 | 1% | 21 | Yes | 2.0 | 2.67 |
| W90-8 | 90 | 38 | None | 3 | Yes | 3.6 | 3.44 |
| W175-1 | 175 | 20 | None | 1 | Yes | 5.5 | 4.55 |
| W250-1 | 250 | 20 | None | 14 | No | 1.0 | 1.55 |
| W250-2 | 250 | 20 | None, Unvented | 12 | No | 1.0 | 1.67 |
| A250-1 | 250 | 20 | None | 7 | No | 1.0 | 1.78 |
| A250-2 | 250 | 20 | 1% | 7 | No | 1.0 | 0.78 |

Mechanical results

A graph of porosity response during testing of the first five days for the pre-compacted samples under different moisture, stress and temperature conditions are shown in Figure A-12. The data logging for W90-7 was interrupted. The volumetric strain evolution of sample W250-1 is given in Figure A-13. The sample had an initial porosity of more than 40%. During the first loading stage at a hydrostatic stress of 1.5 MPa and 50 °C, the porosity reduced about 10% over the course of 120 hours. When the temperature was increased to 250 °C, an additional 18% porosity reduction was achieved over the course of just 10 hours. The increase in load to a hydrostatic stress of 20 MPa added another 12% volumetric strain within an hour, while during the final 290 hours the sample only compacted another 0.5 to 1%. Note that increasing the temperature significantly weakens the backfill.

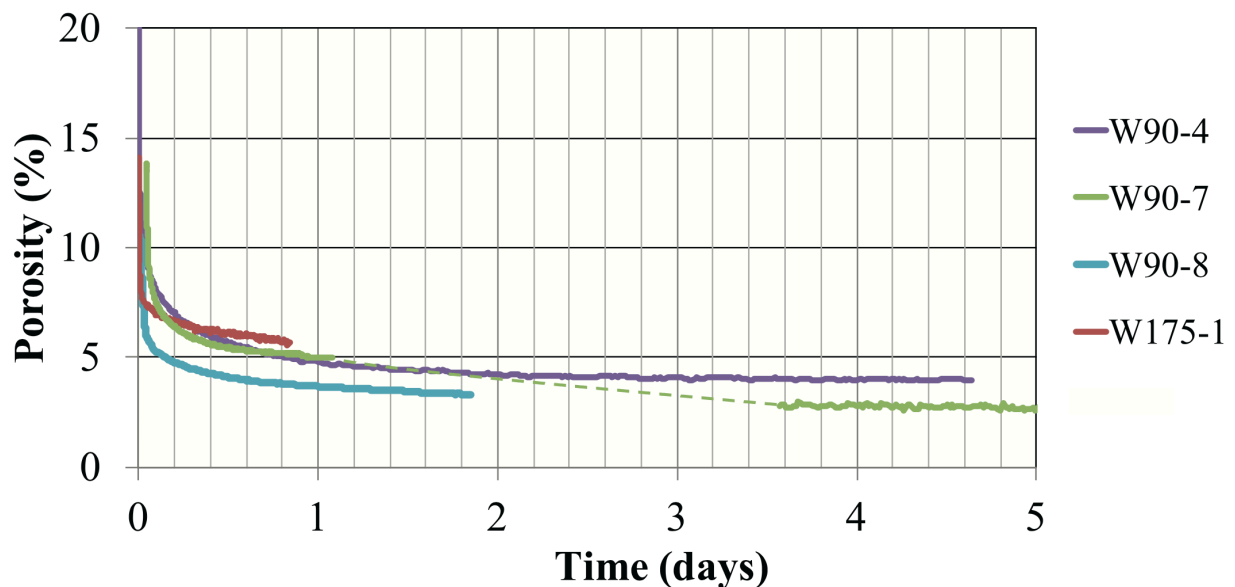


Figure A-12: porosity vs time for pre-conditioned samples at different moisture, stress and temperature conditions. Test conditions are given in Table A-2 (Mills et al. 2018).

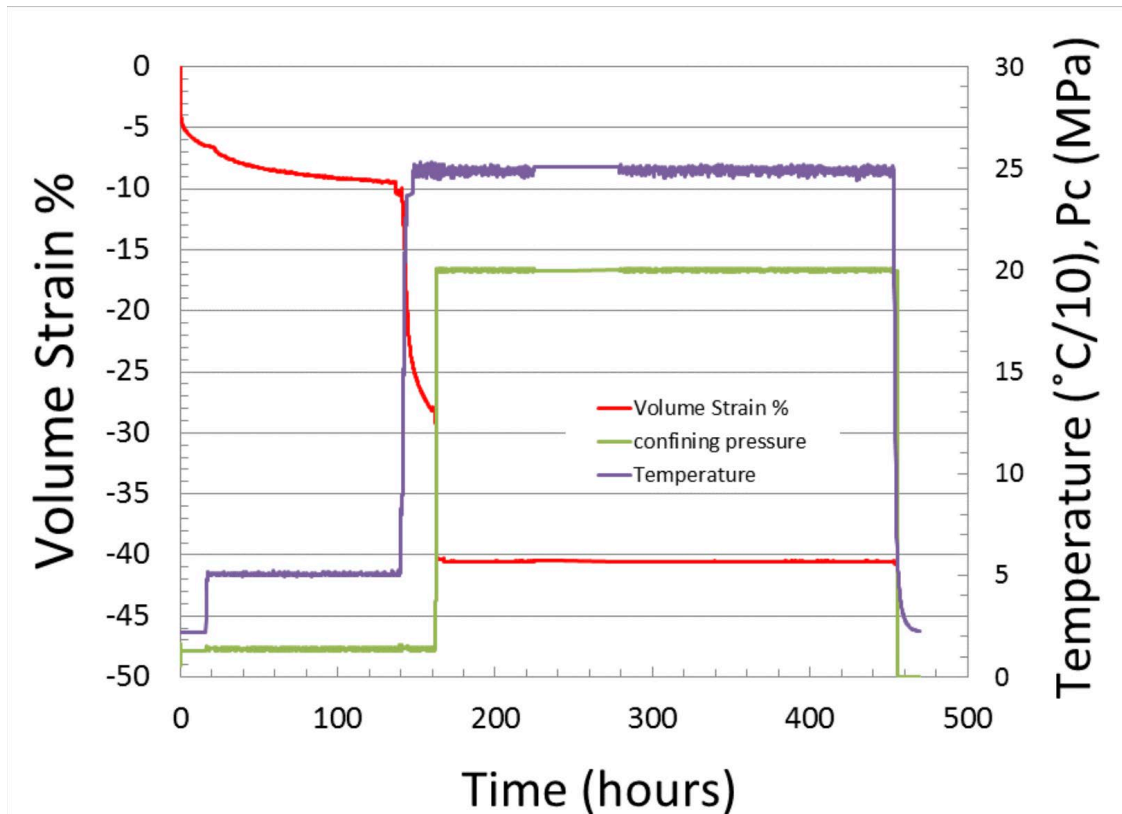


Figure A-13: volume strain, temperature and pressure vs time for W250-1. Note that temperature is in $^{\circ}\text{C}/10$ (Mills et al. 2018).

Microstructures and interpretation of deformation mechanisms

Mills et al. 2018 note that without addition of moisture samples compacted at 90°C and 175°C were compacted by processes of mechanical abrasion, grain breakage and minor plastic deformation (see Figure A-14a-c). These samples contain visible pore space, unhealed grain boundaries and rearrangement of grains. The abraded surfaces in Figure A-14b, show clear signs of grain sliding. The distorted planes are interpreted as features of dislocation glide operating in the backfill. No differences in microstructure could be observed between compaction at 38 MPa (W90-8) and 20 MPa (W90-1), indicating similar mechanism were active. In addition, no difference is observed between the sample compacted down to 8.3% porosity (W90-1) and 3.4% (W90-8). Samples with added moisture were observed to have coherent or healed grain boundaries, which according to Mills et al. 2018 has been facilitated by pressure solution processes and occlusion of fluid pore space along grain boundaries. These features can be seen throughout Figure A-15. Cleaved surfaces are created by breaking through the grains, instead of along grain boundaries indicating a large increase in the cohesion of the grain boundaries due to healing processes. Isolated and occluded fluid pore spaces are widespread along grain boundaries in all of the micrographs and it shows a clear snapshot of the breakdown of brine films during deformation into isolated inclusions.

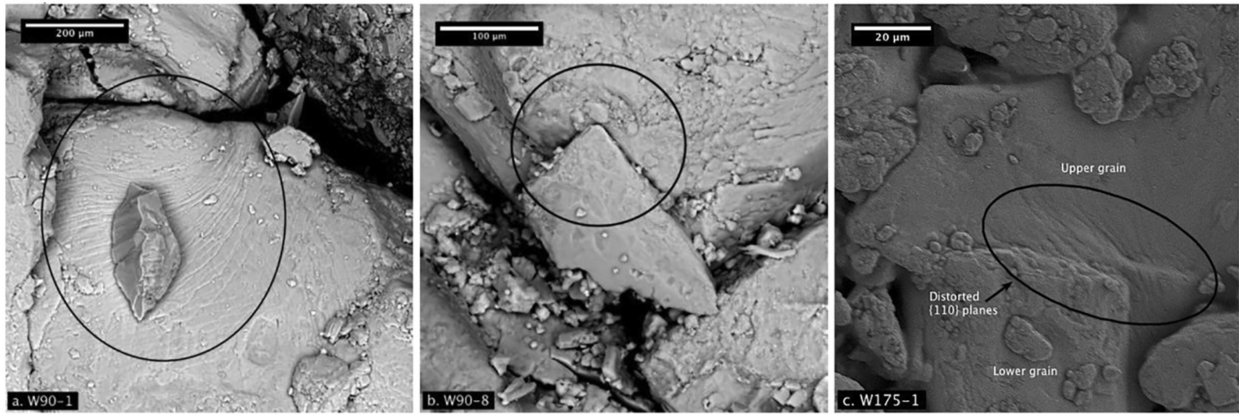


Figure A-14: SEM micrographs of compacted backfill without added moisture. (a) W90-1: curved $\{110\}$ planes showing glide along to portion of central grain, whereas linear $\{110\}$ planes can be observed in lower grain (Magnification $\times 250$). (b) W90-8: distinct grain boundaries showing no cohesion and rough abraded surfaces ($\times 500$) and (c) W175-1: plastic deformation at grain contact and open pore space ($\times 1300$).

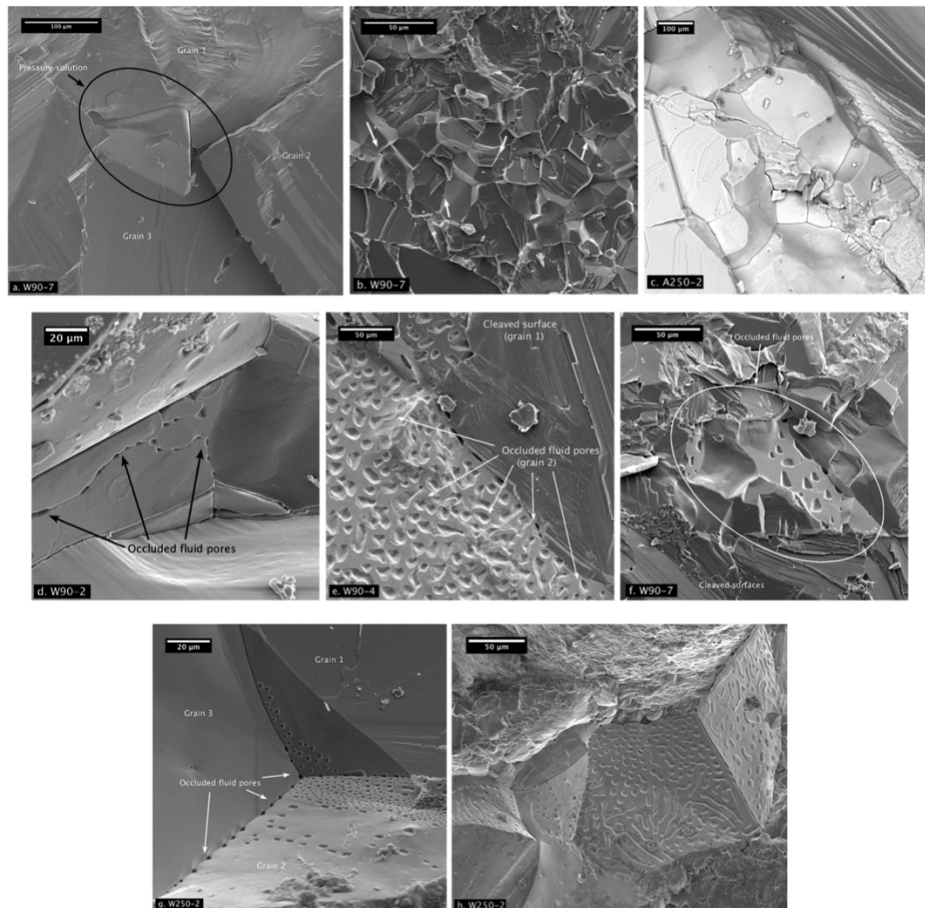


Figure A-15: SEM micrographs of samples with 1 wt % added moisture. (a) W90-7: highly deformed grain at center showing indentation features, surrounded by grains showing glide features ($\times 650$). (b) W90-7: micrograph showing grain boundaries are in full contact and pore space has been eliminated, most likely by pressure solution processes ($\times 1000$). (c) A250-2: rounded cubic grains with bulging grain boundaries ($\times 250$). (d) W90-2: occlusion of pore space and formation of inclusions ($\times 1000$). (e) W90-4: array of fluid canals and pore space imprinted on grain boundary surface ($\times 750$). (f) W90-7: area of occluded fluid pore space at center surrounded by cleaved faces ($\times 950$). (g) W250-2: triple junction with canals of residual moisture and occluded pores ($\times 1500$). (h) W250-2: occluded fluid droplets and canals on a planar grain boundary ($\times 500$) (Mills et al. 2018).

A.8 Utrecht University stress relaxation tests

A key issue with interpreting all previous experiments in terms of stress-strain rate behavior is that there is ongoing porosity reduction during the experiments. Hence the changes in strain rate between each loading stage are not only caused by stress changes but also caused by a continuous decrease in porosity. Therefore, the individual effect of stress or porosity on creep rate cannot easily be determined. Interpretation of the controlling mechanisms are further complicated by the use of a large grain size distribution, which activates multiple mechanisms and is expected to vary with sorting. Zhang et al. 2007 investigated the effect of water on the dominant deformation mechanism in crushed salt backfill at room temperature down to 1% porosity using stress relaxation experiments on narrow grain size fractions, the results are described in this section.

Experimental method

Analytical grade sodium chloride powder was sieved into grain size fractions of <50, 70±20, 137±12, 280±20, 412±12 and 560±20 µm (as opposed to natural rock salt grains in the other experiments). The samples had a weight of 6.24g each, corresponding to a length of 10 mm and diameter of 20 mm when fully compacted. Most samples were oven-dried at 50°C for several days before use and the samples that were used to determine mechanical behavior in 100% dry conditions were dried at temperatures of 100-150°C. Pre-compaction and stress relaxation tests were carried out in an Instron 8562 materials testing machine using an oedometer for 1D compaction with an inner diameter of 20 mm. Applied stress and relative position was measured by the Instron machine and an additional LVDT was mounted between the top piston and the vessel. The plastic strain rate of the sample was determined from the stress relaxation tests after correcting for machine and sample stiffness. The material was pre-compacted at constant strain rate ($10^{-5} - 10^{-4} s^{-1}$) to a porosity of 25%, with the pores filled with lab-air. Pore fluid was then introduced, and the sample was then compacted to the desired porosity (25-1%). Experiments were conducted using lab-air/decane, 100% saturated brine and dry argon gas as pore fluid to represent dry, wet and humid (uncontrolled) conditions. Permeability measurements were performed using decane and brine and samples were prepared for thin sectioning.

Experimental results and mechanistic interpretation

The experimental results can be divided into three groups, based on the different pore fluids used. An overview of the measured stress relaxation of these three different groups is given in Figure A-16a. The samples flushed with argon is the strongest, while the sample flooded with saturated solution is the weakest. The samples exposed to lab air and decane have an intermediate relaxation rate. No difference is observed after introducing decane (samples were filled with lab air before injecting decane). The presence of moisture (lab humidity) and water significantly weakened the samples. The stress relaxation data can be converted into strain rate data and displayed in log-log space to obtain the creep rate dependence on stress for samples tested under various conditions and to interpret data in terms of deformation mechanisms (see Figure A-16b,14).

In the argon dry samples, the strain rates are very sensitive to stress (see Figure A-16b). The strain rate sensitivity to stress can be represented using the n -value or so-called stress exponent. The average apparent n -value for the dry argon samples is about 20. The effect of porosity and grain size on the slope is negligible. Note that for completely dry conditions and low porosities (<10%) stresses of 60-110 MPa are required to obtain significant strain rates ($10^{-8} s^{-1} - 10^{-6} s^{-1}$). Extrapolating these rates to low stresses < 10 MPa, would result in negligible ($10^{-23} s^{-1}$) strain rates. These high n values are comparable to experiments on single crystals at room temperature, for which n values of 18.5-20 are reported (Holcomb & Zeuch 1990). These high n value experiments show clear features of dislocation glide (see section 2.2).

Moisture in the lab air clearly weakens lab dry samples compared to the argon dry ones (see Figure A-17a). The average n value of the lab air and decane filled samples is 5.1. In the saturated samples, the n values are exactly 1 at stresses less than 15-20 MPa (see Figure A-17b), while at higher stresses the n value gradually transitions from 1-6. The deformation mechanism for the samples flooded with a saturated solution is most likely pressure solution, given the n value and microstructural observations. Many studies on crushed rock salt and dense rock salt conclude that the steady state flow laws have a stress exponent of about 5. For example, the Norton creep laws (see Section A.1) which incorporates an n value of 5 based on compaction experiments of Kortheus 1996.

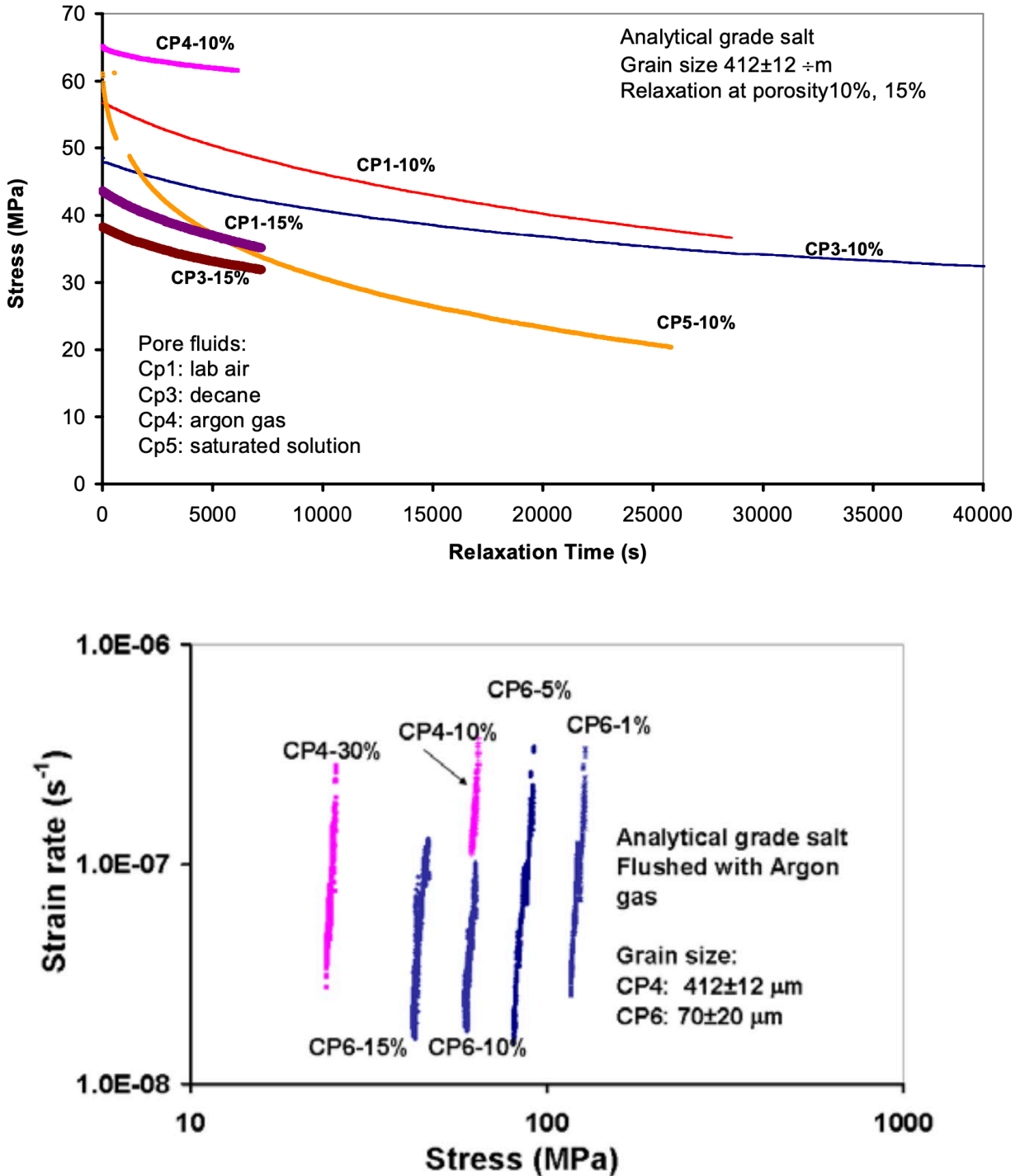


Figure A-16: (top) an overview of stress relaxation data showing the different rates of relaxation for samples exposed to a saturated solution, lab-air, decane and dry argon gas, for analytical grade salt with all samples having a grain size of $412 \mu\text{m}$. The samples flushed with dry argon gas have a slow relaxation rate, the samples exposed to saturated solution have a rapid relaxation rate and samples with lab-air/decane have an intermediate relaxation rate. The porosity at the start of relaxation has been indicated in %. Depending on relaxation rate and time 0.1 – 1.5% porosity reduction has occurred during relaxation. (bottom) Strain rate vs. stress obtained from relaxation experiments on samples flushed with dry argon gas. Slopes are independent of grain size and porosity. (Zhang et al. 2007).

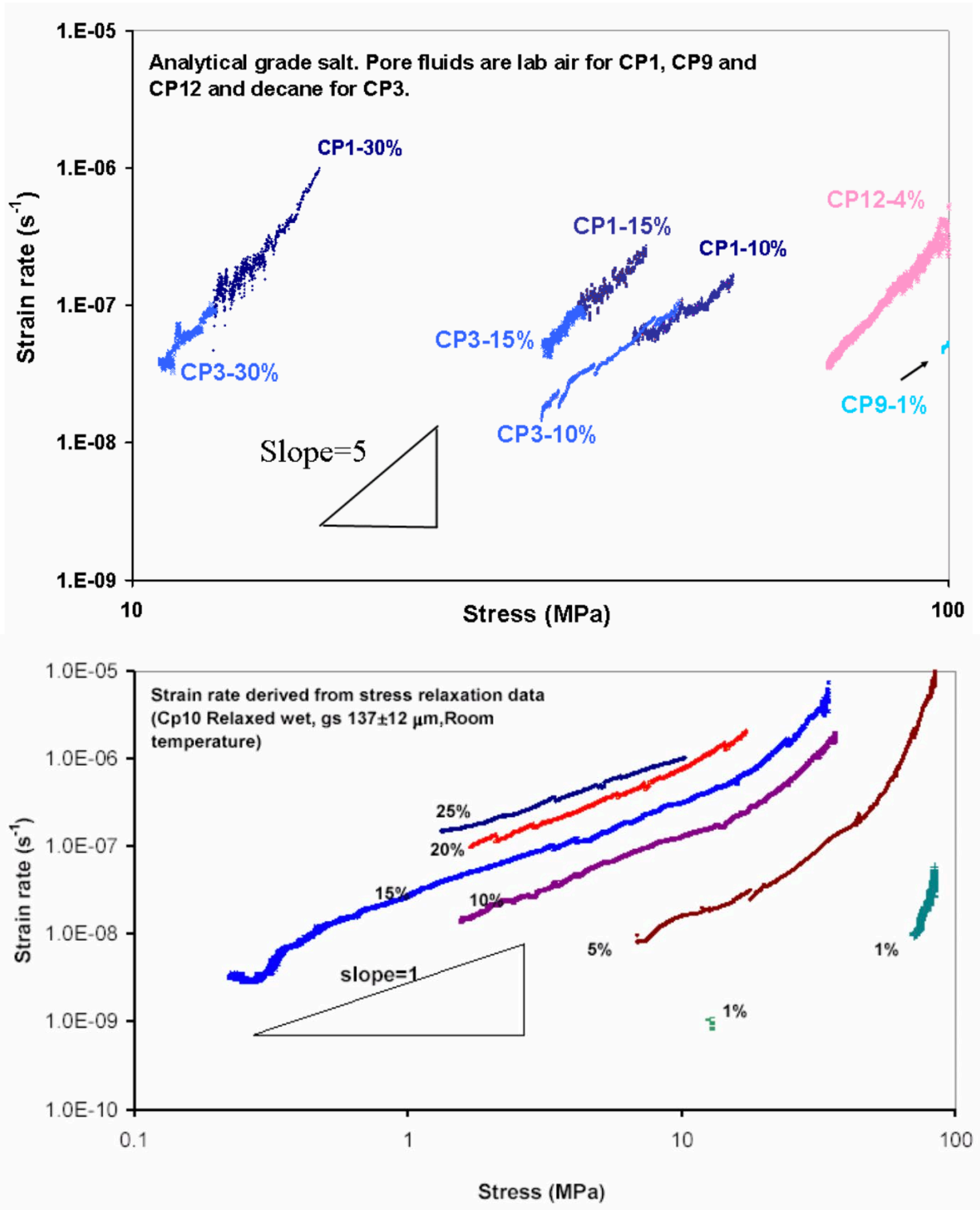


Figure A-17: Strain rate vs. stress obtained from relaxation experiments on samples exposed to (top) lab air and (bottom) saturated solution. Sample CP1, CP3 and CP9 have a grain size of $412 \pm 12 \mu m$, CP10 & CP12 have a grain size of $137 \pm 12 \mu m$ (Zhang et al. 2007).

Microstructures

Two thin sections have been made from the compacted samples: Cp12 and An14 (see Figure A-18). Sample Cp12 was compacted with lab air as pore fluid to 5.4% porosity, while An14 was compacted to 5% with saturated solution present in the pores. No micrograph is present from the argon dry compacted sample. The grains can be classified into two groups: the highly deformed (or the highly etched) grains and less-deformed grains. The highly deformed grains have abundant internal microstructures. The less-deformed grains show flat etching surfaces and have no or minor internal microstructures. The two group grains usually have very straight contact with less-deformed grains grow into the highly deformed grains.

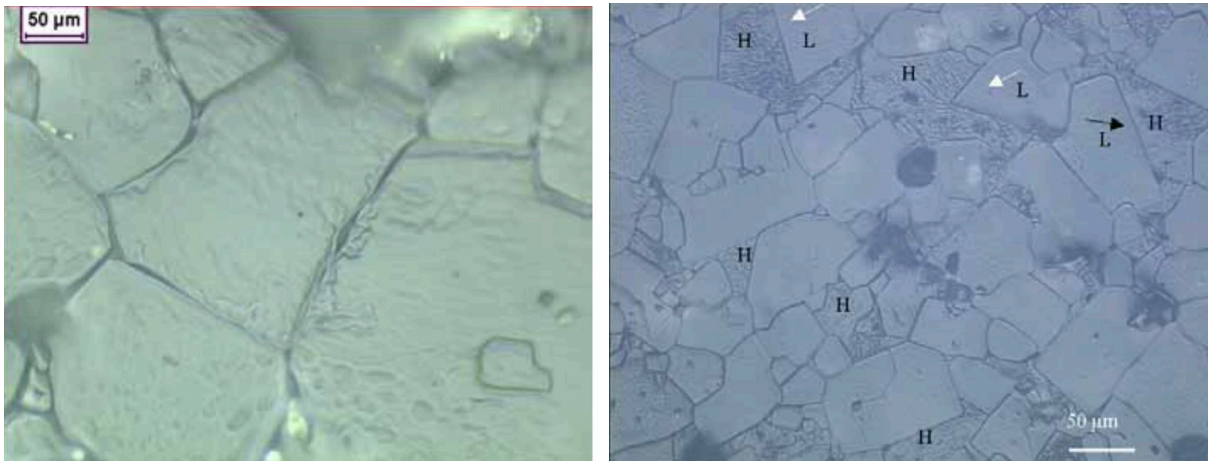


Figure A-18: (a) reflected light micrograph of sample An14 (compactd with saturated solution). Note the indentation features between two less deformed grains. Precipitation close the grain boundaries may be caused by evaporation of brine during preparation of the thin section. (b) reflected light micrograph of sample Cp12 (compactd with lab air). Grains can be classified into highly deformed (H) and less deformed grains (L). Less deformed grains consume the highly deformed grains, indicating recrystallization has occurred. (Zhang et al. 2007).